Advances in Colloid and Interface Science 323 (2024) 103071

Contents lists available at ScienceDirect

Advances in Colloid and Interface Science

journal homepage: www.elsevier.com/locate/cis

Polymorphic phase transitions in triglycerides and their mixtures studied by SAXS/WAXS techniques: In bulk and in emulsions

Diana Cholakova *, Nikolai Denkov

Department of Chemical and Pharmaceutical Engineering, Faculty of Chemistry and Pharmacy, Sofia University, 1 James Bourchier Avenue, 1164 Sofia, Bulgaria

ARTICLE INFO

Keywords:
Triacylglycerol
Polymorphism
Solid lipid nanoparticle
α-form, β'-form, β-form
Crystallization
Melting

ABSTRACT

Triacylglycerols (TAGs) exhibit a monotropic polymorphism, forming three main polymorphic forms upon crystallization: α, β' and β. The distinct physicochemical properties of these polymorphs, such as melting temperature, subcell lattice structure, mass density, *etc.*, significantly impact the appearance, texture, and long-term stability of a wide range products in the food and cosmetics industries. Additionally, TAGs are also of special interest in the field of controlled drug delivery and sustained release in pharmaceuticals, being a key material in the preparation of solid lipid nanoparticles. The present article outlines our current understanding of TAG phase behavior in both bulk and emulsified systems. While our primary focus are investigations involving monoacid TAGs and their mixtures, we also include illustrative examples with natural TAG oils, highlighting the knowledge transfer from simple to intricate systems. Special attention is given to recent discoveries *via* X-ray scattering techniques. The main factors influencing TAG polymorphism are discussed, revealing that a higher occurrence of structural defects in the TAG structure always accelerates the rate of the α → β polymorphic transformation. Diverse approaches can be employed based on the specific system: incorporating foreign molecules or solid particles into bulk TAGs, reducing drop size in dispersed systems, or using surfactants that remain fluid during TAG particle crystallization, ensuring the necessary molecular mobility for the polymorphic transformation. Furthermore, we showcase the role of TAG polymorphism on a recently discovered phenomenon: the creation of nanoparticles as small as 20 nm from initial coarse emulsions without any mechanical energy input. This analysis underscores how the broader understanding of the TAG polymorphism can be effectively applied to comprehend and control previously unexplored processes of notable practical importance.

Abbreviations: 2D, two dimensional; API, active pharmaceutical ingredient; CNO, coconut oil; DAG, diacylglycerol; FA, fatty acid; FHCO, fully hydrogenated canola oil; FHSFO, fully hydrogenated sunflower oil; FWHM, full width at half maximum peak height; HOSO, high oleic sunflower oil; MAG, monoacylglycerol; MC, molecular compound; MCT, medium chain triglyceride oil; MDG, mono- and di-glyceride mixture; NLC, nano lipid carrier; SLN, solid lipid nanoparticle; TAG, triacylglycerol; TCP, triglyceride property calculator; UV, ultraviolet; w/o/w, water-in-oil-in-water double emulsion; w/o, water-in-oil emulsion; *TAGs abbreviations*: $C_XC_YC_Z$, triacylglycerol with fatty acid residues containing *X*, *Y* and *Z* number of C-atoms; CaCaCa ≡ C_8TAG, tricaprylin (1,2,3-trioctanoyl glycerol); CCC ≡ C_{10}TAG, tricaprin (1,2,3-tridecanoyl glycerol); LLL ≡ C_{12}TAG, trilaurin (1,2,3-tridodecanoyl glycerol); MMM ≡ C_{14}TAG, trimyristin (1,2,3-tritetradecanoyl glycerol); PPP ≡ C_{16}TAG, tripalmitin (1,2,3-trihexadecanoyl glycerol); SSS ≡ C_{18}TAG, tristearin (1,2,3-trioctadecanoyl glycerol); OOO ≡ $C_{18:1}$TAG, triolein (1,2,3-tri(*cis*-9-octadecanoyl) glycerol); AAA ≡ C_{20}TAG, triarachidin (1,2,3-trieicosanoyl glycerol); *Experimental techniques*: AFM, atomic force microscopy; DSC, differential scanning calorimetry; MD, molecular dynamic (simulations); NMR, nuclear magnetic resonance; SANS, small angle neutron scattering; SAXD, small angle X-ray diffraction; SAXS, small angle X-ray scattering; TEM, transmission electron microscopy; USAXS, ultra small angle X-ray scattering; WAXS, wide angle X-ray scattering; WAXD, wide angle X-ray diffraction; *Chemical compounds*: Brij 30, polyoxyethylene (4) lauryl ether; Brij O10, polyoxyethylene (10) oleyl ether; Brij S20, polyoxyethylene (20) stearyl ether; C_{16}MAG ≡ monopalmitin, 1-monohexadecanoyl-*rac*-glycerol; C_{18}MAG ≡ monostearin, 1-monooctadecanoyl-*rac*-glycerol; $C_{18:1}$MAG ≡ monoolein, 1-(cis-9-octadecenoyl)-*rac*-glycerol; $C_{18:1}EO_2$, polyoxyethylene (2) oleoyl ether; C_{22}MAG ≡ monobehenate, 1-monodocosanoyl-*rac*-glycerol; LAS, sodium linear alkylbenzene sulfonate; PGPR, polyglycerol polyricinoleate; PVA, polyvinyl alcohol; P-170, palmitic acid oligoester; S100, purified soybean lecithin, ≥ 94% phosphatidylcholine, rich in doubly unsaturated 18:2 FA; SDS, sodium dodecyl sulfate; Tween 20, polyoxyethylene (20) sorbitan monolaurate; Tween 80, polyoxyethylene (20) sorbitan monooleate; WPI, whey protein isolate; DLPC, 1,2-dilauroyl-*sn*-glycero-3-phosphocholine; DOPC, 1,2-dioleoyl-*sn*-glycero-3-phosphocholine.

* Corresponding author.
E-mail address: dc@lcpe.uni-sofia.bg (D. Cholakova).

https://doi.org/10.1016/j.cis.2023.103071
Received 7 September 2023; Received in revised form 4 December 2023; Accepted 11 December 2023
Available online 18 December 2023

Notation

Capital Latin letters

A	pre-exponential factor (Eq. 12)
A	Euclidean dimension of the embedding space (Eqs. 17-18)
B	constant (Eq. 21)
C_n	normal alkane with n carbon atoms in its chain (C_{31} – n-henetriacontane)
C_p	specific heat capacity at constant pressure
C	carbon
D	mass fractal dimension
D_S	surface fractal dimension
E	elastic modulus
G	Gibbs free energy
ΔG^*	nucleation free energy
G	constant (Eq. 21).
H_m	melting enthalpy
$\Delta H_{m,X}$	melting enthalpy of phase X
I	scattering intensity
J	nucleation rate
K	constant (Eq. 13) or shape factor (Eq. 20)
M	mass
M_w	molecular weight
P	Porod exponent
R	universal gas constant
R	size/radius of an object (section 4.6)
R_g	radius of gyration
S	surface area (section 4.6)
T	temperature
T_m	melting temperature
$T_{m,X}$	melting temperature for phase X
$T_{m,r}$	melting temperature for particle with radius r
T_{cr}	onset crystallization temperature
$\Delta T = T_m - T$	supercooling below the melting temperature
V	volume
ΔV-	difference in the molar volume between liquid and crystalline states (eq. 15)
V_S	specific volume of solid (Eq. 23)
Z_{ave}	average diameter (measured by dynamic light scattering)

Small Latin letters

a, b, c	unit cell parameters
a_d	primary particle diameter (Eqs. 17-18)
d	repeat distance of the layers (also denoted as d_{001})
k	number of components in a TAG mixture
l	average repeat length
n	number of C-atoms in a single acyl chain
$\overline{n}$	average number of C-atoms in the acyl chains of triglycerides
p	pressure
q	scattering vector
r	particle size (Eq. 23)

Greek letters

α, β' and β	main polymorphic forms of triacylglycerols
α, β and γ	angles in the unit cell (section 3.2)
γ	surface/interfacial tension
γ_{sl}	interfacial tension between solid substrate and liquid oil
Δ	symbol showing the change of a given quantity
Δn	chain length difference
ε^*	critical strain
θ	scattering angle
λ	wavelength
μ	chemical potential
ξ	crystalline domain size
π	surface pressure
ρ	density
σ^*	yield stress
χ	molar fraction
Φ	volume fraction

1. Introduction: Triglycerides polymorphism

Triacylglycerols (TAGs), commonly known as triglycerides, are esters of glycerol (propane-1,2,3-triol) and three fatty acids. TAGs are type of lipids which present major constituents in various consumers products, *incl.* foods, cosmetics, personal care products and medicines. Within the human diet, TAGs are commonly referred to as either fats or oils, depending on their physical state at room temperature (solid for fats and liquid for oils). They are abundant in foods such as meats, dairy products, nuts, seeds and other dietary sources [1–3]. Moreover, TAGs play a vital role in energy storage and metabolism, contributing to essential biological processes [4–7]. In the cosmetic industry, TAGs serve multiple functions. They are used as emollients, moisturizers, texture enhancers, and cleansing agents, offering excellent skin compatibility and hydration [8–11]. TAGs also facilitate the delivery of lipophilic components, such as colour pigments, ultraviolet (UV) filters, and other bioactive molecules [12,13].

A comprehensive understanding of TAGs phase behavior is vital for controlling the physical properties, stability, and functionality of fats and oils in various applications. For instance, the texture and mouthfeel of lipid-rich products such as margarine, butter, ice cream, whipped cream, and chocolate depend largely on the crystalline structure formed by frozen TAG molecules [14–18]. Likewise, the shelf life and stability of these products are closely related to the crystalline properties of lipid molecules, as undesirable crystalline forms can lead to fat bloom, impacting negatively their quality [18,19]. In the field of pharmaceutics, the physical state of lipid-based carriers has been shown to significantly impact the drug delivery and bioavailability [13,20–22]. Recent studies have revealed that the physical state of lipids may directly affect the rate of initial lipolysis of TAGs during digestion [23–26]. Solid lipid particles were found to cause a delay in digestive lipolysis within the initial two hours. Conversely, liquid lipid carriers exhibited higher concentrations during this period. However, both samples underwent extensive hydrolysis, and after longer periods (24 h), the bioaccessibility did not show significant differences [23]. These findings hold practical implications in the formulation and design of food or drug products, as they can be utilized to prepare healthier foods or products with delayed release properties.

Monoacid saturated TAGs exhibit three main polymorphic forms, namely α, β' and β [27,28]. Polymorphism refers to the capability of a material to exist in multiple crystalline forms arising due to the differences in molecular arrangement [29]. The α, β' and β polymorphs have distinct melting temperatures, defined as the temperatures below which the Gibbs free energy of the crystal becomes lower than that of the liquid phase, see Fig. 3a below.

The first evidence of the existence of more than one melting points in tristearin (SSS, C_{18}TAG) dates back to 1849 when Heintz observed two distinct melting points for SSS [30]. Subsequent investigations by Duffy confirmed this observation [31,32]. However, further insights into the TAG polymorphism were limited until the pioneer work of Clarkson and Malkin, who used X-ray diffraction to study them [27]. Though almost a century has elapsed since this first paper was published, nowadays the X-ray scattering experiments, continue to be the main experimental method giving a direct information about the inner molecular structure

of the crystalline lipids. Interestingly, even for the simplest TAGs, novel findings continue to be reported.

For example, Ghazani and Marangoni recently demonstrated the existence of β polymorphic form for SSS with melting temperature of 75.7 ± 0.5 °C [33]. This temperature is roughly 3 °C higher than the melting temperature commonly reported by other researchers, $T_m \approx$ 73 °C [34–36]. The new β-form has been obtained after a two-year static isothermal crystallization of SSS molecules dissolved in acetone and stored at 4 °C, resulting in formation of SSS monocrystals. This β-form has slightly shorter lattice long-spacing of 44.91 Å compared to the one reported for the other β-form, $d \approx 45.21$ Å [33].

Furthermore, in another study by Takeguchi and co-authors, the existence of multiple β-forms of saturated monoacid TAGs was demonstrated for trilaurin (LLL, C_{12}TAG), trimyristin (MMM, C_{14}TAG), tripalmitin (PPP, C_{16}TAG) and SSS [37]. The multiple β phases were obtained through distinct heat treatments. The β-forms made directly from the α-form, without passing through the β' polymorph, had slightly lower melting temperatures than the β-forms obtained from β'-form: 45.7 °C *vs.* 44.8 °C for LLL. A similar polymorphism, characterized by the same subcell packing, was observed across all β-forms [37].

The development of highly brilliant synchrotron X-ray sources made possible phase behavior investigation not only in bulk systems but also in dispersed TAG systems [38–42] and even direct studies of processes occurring at the oil-water interface [43]. Such studies shed more light about the role of emulsifier in TAG crystallization and subsequent polymorphic phase transitions. Furthermore, the polymorphic phase transitions in emulsified TAG systems have been recently used to demonstrate a novel spontaneous disintegration mechanism able to produce TAG nanoparticles with sizes down to 20 nm [44]. Remarkably, these nanoparticles are obtained from coarse triglyceride-in-water emulsion droplets solely by cooling and heating them in an aqueous surfactant solution, without any mechanical energy input to the system. The mechanism behind this phenomenon, along with additional details, is discussed in Section 6.6.

This review paper aims to provide a concise yet comprehensive overview of our current understanding of the TAG phase behavior in both bulk and emulsified systems. Considering the breadth of this research field, we focus on investigations involving monoacid TAG systems. Nevertheless, we have also included illustrative examples involving natural TAG oils when relevant, to demonstrate that the knowledge gained from the simpler systems can often be readily extended to more complex ones. Particular attention is given to the recent discoveries in the polymorphic phase behavior of TAGs, which have been made through the use of X-ray scattering techniques.

The paper is structured as follows: Section 2 briefly addresses the debate regarding the molecular arrangement of TAGs in their liquid state. Sections 3 and 4 provide an overview of polymorphism in bulk TAG systems. Section 3 examines the phase behavior of pure monoacid TAGs, while Section 4 discusses the behavior of TAG mixtures. Section 5 presents insights about TAG surface layers. Section 6 focusses on investigations involving triglyceride-in-water emulsion systems, highlighting the comparison between findings in bulk and emulsified systems. Lastly, Section 7 summarizes the key observed features in TAG polymorphism and suggests potential directions for future research.

2. Triglycerides organization in liquid state

The main molecular conformations of TAGs are schematically shown in Fig. 1. They differ in the position of the fatty acid (FA) acyl chains with respect to the glycerol backbone structure. In crystallized TAGs, the tuning fork conformation is predominantly observed, followed by the chair conformation, whereas in liquid state all different conformations are possible [36]. The difference between the chair and tuning fork conformations (both resembling "*h*" shapes) is the orientation of FA residues with respect to the glycerol backbone. In the most stable tuning fork conformation, the FA esterified to the two outer C-atoms (*sn*-1 and *sn*-3 positions) align in the same direction, while the middle FA points to the opposite direction. In contrast, in the chair conformation, the fatty acids in *sn*-1 and *sn*-2 positions orient in the same direction, with the FA in *sn*-3 faces the opposite direction. In the trident conformation (also known as *E* shape), all three FA residues are oriented in the same direction. This conformation is typically observed for TAG molecules positioned at the oil-water phase boundary, where the oxygen atoms are oriented towards the water molecules, minimizing the unfavorable contact between water and hydrophobic acyl chains [45–47]. Lastly, the propeller conformation (Y shape) displays relatively similar angles between separate FA moieties, around ≈ 120°.

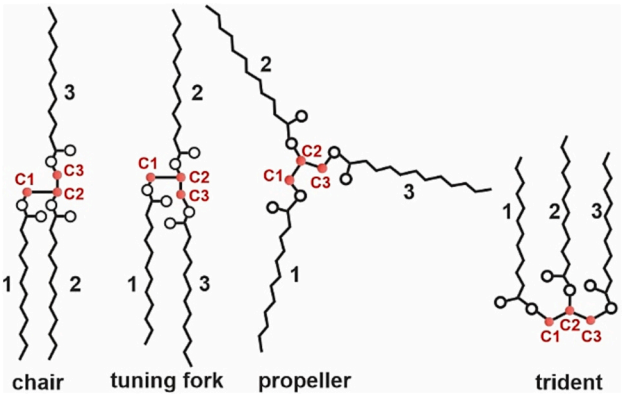

Fig. 1. Molecular conformations of TAGs.

In the liquid state, all different molecular conformations are possible. However, a debate persists regarding whether the TAG molecules exist in a completely random orientation or if some level of molecular organization is present even at temperatures considerably higher than their melting point. This suggestion is based on the observation that in the liquid state, a broad peak with a maximum at scattering vector $q \approx$ 2.2–3 nm^{-1} (depending on the exact TAG studied) is observed in SAXS and SANS. This peak suggests a fluid ordering with a characteristic distance of 2.1–2.8 nm, see Fig. 2a [48,49].

Initially, Larsson was first to propose the existence of a pseudo-lamellar molecular arrangement in liquid TAGs, similarly to the structure found in smectic liquid crystals. This arrangement was suggested to have a correlation length of up to 200 Å, see Fig. 2b [50]. In a later study, Cebula et al. used neutron scattering to investigate the issue and concluded that there are no discrete layers persisting in the liquid state. Instead, they postulated a molecular arrangement similar to that observed in nematic liquid crystals for molten trilaurin, see Fig. 2c [48]. The underlying molecular conformation of the TAGs was still believed to be predominantly *h* shaped. Afterwards an alternative discotic model was proposed by Corkery and co-authors, based on results obtained with Monte-Carlo computer simulations [51]. In this model, they suggested that, in the liquid state, most molecules exist in a propeller conformation (Y) driven by the entropy, see Fig. 2d. The individual molecules were proposed to be loosely bounded within discs which are able to stack into short cylindrical rods, ultimately forming time-averaged hexagonal mesophases [51]. Although this model agreed with the scattering data, subsequent computer simulations indicated that the existence of long-range discotic order was unlikely [52].

More recently, Sadeghpour et al. [49] suggested a combined model between the previously known. In this model, part of the molten TAG molecules are assumed to be arranged in a core cluster with their glycerol backbones assembled in back-to-back fashion, whereas their fatty acid residues point outwards, see Fig. 2e. Additionally, a second layer with approximately 10% occupancy of loosely attached TAG molecules was needed to fully explain X-ray scattering data. The authors suggested that the occupancy of this second layer increases as the temperature decreases, eventually leading to the formation of a completely

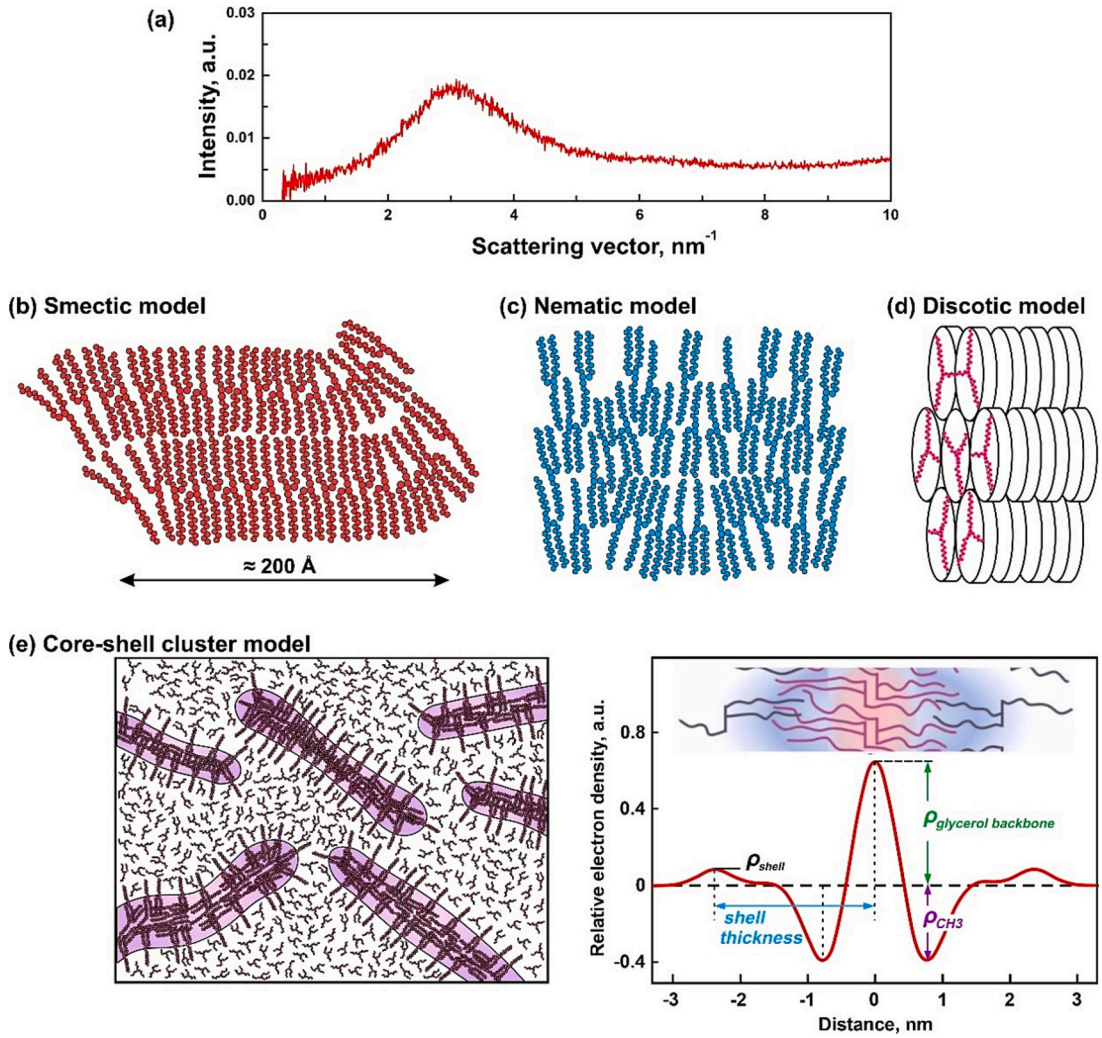

Fig. 2. Models proposed for the organization of liquid TAG molecules. (a) SAXS spectra of liquid LLL obtained at 52 °C. (b) Smectic TAG organization [50]. (c) Nematic TAG organization [48]. (d) Discotic model [51]. (e) Core-shell cluster model. Adapted and partially reprinted with permission from Ref. [49]. Copyright © 2018, American Chemical Society.

occupied second layer that facilitates the crystallization process [49]. Notably, these small smectic lamellar domains existed in an uncorrelated manner, maintaining an overall isotropic structure within the molten TAG.

Using all-atom molecular dynamics (MD) simulation for tristearin and triolein (OOO), Golodnizky et al. found that the most abundant TAG conformation in the liquid state was the trident conformation (*ca.* 50–56% of all molecules), followed by the chair (28–34%), propeller (11–14%) and tunning fork conformations (1–6%) [53]. The authors concluded that a degree of organization was present, given the existence of characteristic lengths, but the molecules were distributed arbitrarily with respect to their conformation within the formed clusters. Moreover, the highest percentage of trident molecules was explained with a preferable molecular pairing between trident molecules and molecules adopting other conformations. In contrast, no such preferential pairing was observed for molecules in tuning fork conformation, suggesting that the molecules would need to reorganize to allow the crystallization process [53].

As seen from this short overview, further dedicated experiments and MD simulations will be needed to comprehensively resolve the actual organization of TAG molecules in the liquid state.

3. Polymorphism in bulk single triglycerides

This section reviews the properties of main polymorphic forms inherent in TAG systems (α, β' and β). The structural characteristics and leaflet arrangements are explained in Section 3.1. Section 3.2 discuss the physicochemical properties exhibited by various polymorphic forms. The impact of external factors on the organization of TAGs is addressed in Section 3.3. Only single bulk TAG systems are considered in this section. The phase behavior of TAG mixtures and dispersions is discussed later in Sections 4 and 6.

3.1. *Triglyceride polymorphs: Main structural characteristics*

The triglyceride polymorphism is of monotropic type [54]. This signifies that the β phase is the most stable form, with the lowest Gibbs energy at all temperatures below its melting temperature, see Fig. 3a. The α polymorph is the least stable form, characterized by the lowest melting temperature and the highest Gibbs energy. In the α polymorph, the acyl chains of molecules, particularly the carbon atoms close to the chain-end groups possesses significant molecular freedom [55–57]. It has been proposed and verified by Raman spectroscopy measurements [58] and high-resolution NMR (nuclear magnetic resonance) experiments [59] that these atoms are able to perform torsional oscillation. Furthermore, the absence of alternative melting features for both odd-

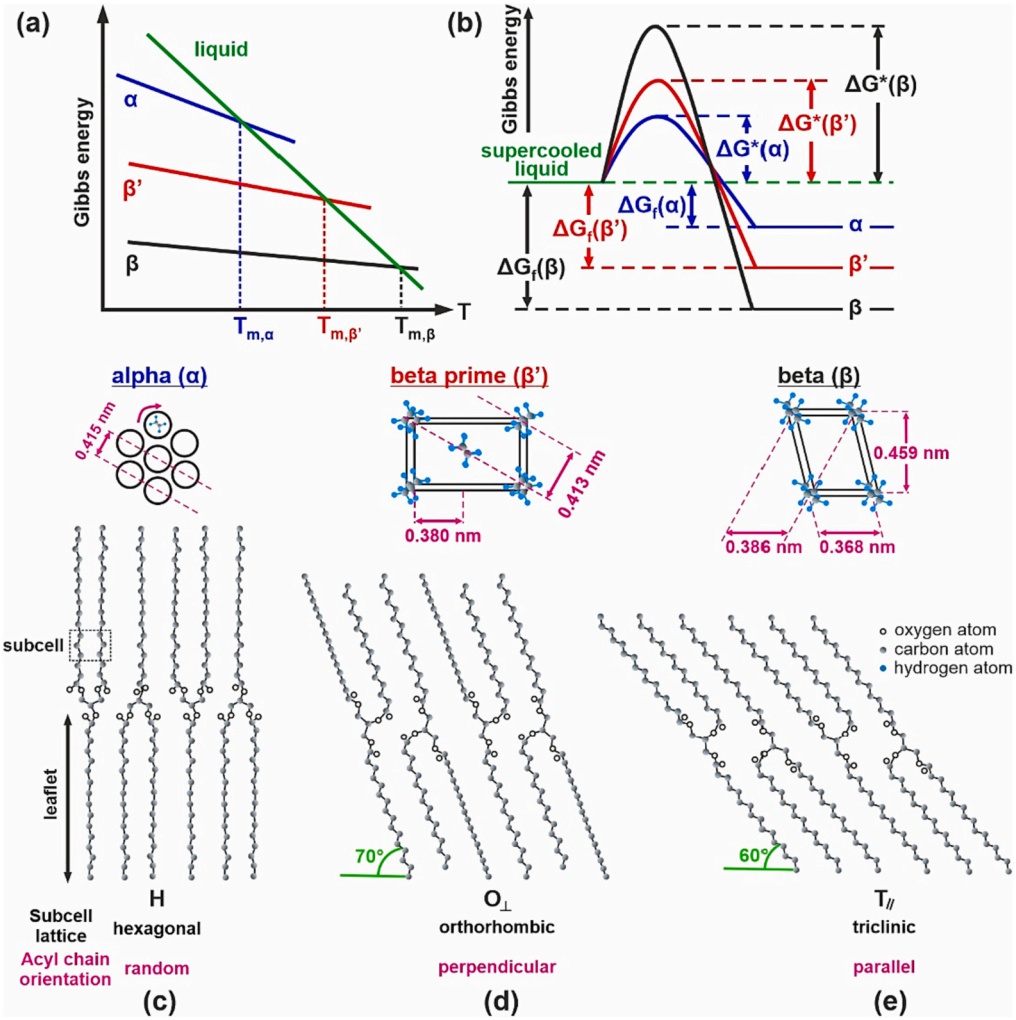

Fig. 3. Triglyceride polymorphs. (a) Gibbs energy as a function of temperature for α, β' and β polymorphs and liquid phase. Melting temperatures for the different polymorphs are shown with dashed lines. (b) Activation free energy for nucleation (ΔG*) of polymorphic forms α, β' and β and respective energy gain upon formation of each polymorph. (c-e) Subcell and unit cell structures for: (c) α, (d) β' and (e) β phases. See text for more detailed explanations. Adapted from Refs. [54, 63–65].

and even-numbered chain length TAGs in α-form indirectly supports this hypothesis [60]. The partial freedom of acyl chains in α phase makes it somewhat similar to the rotator phases observed in *n*-alkanes and other saturated long-chain molecules [39,61,62]. Nonetheless, the molecular motion of TAG molecules is more restricted compared to alkanes due to the typical double-chain-length structure adopted by these molecules, see Fig. 4.

The β' phase falls in between the α and β polymorphs, displaying intermediate properties. However, as the nucleation barrier to the β phase is the highest, the less stable α and β' polymorphs tend to crystallize prior to the emergence of the β phase, see Fig. 3b. The polymorphic transitions α → β', α → β and β' → β are irreversible [63–65].

Monotropic polymorphism allows for two distinct modes of polymorphic transformation processes: solid state transitions and melt-mediated transformations. Solid state transitions take place beneath the melting temperature of the involved polymorphs and occur upon prolonged storage of the sample. These transitions are spontaneous and solely driven by kinetics [54]. Conversely, melt-mediated transitions occur when the sample is heated above the melting temperature of less stable polymorphs (α or β'). In this process, these less stable forms initially melt (*via* an endothermic process) and then re-crystallize (exothermic process) into one of the more stable forms. It has been proposed that the rotation of a single acyl chain within the TAG molecule is sufficient to trigger the rearrangement of the whole crystalline

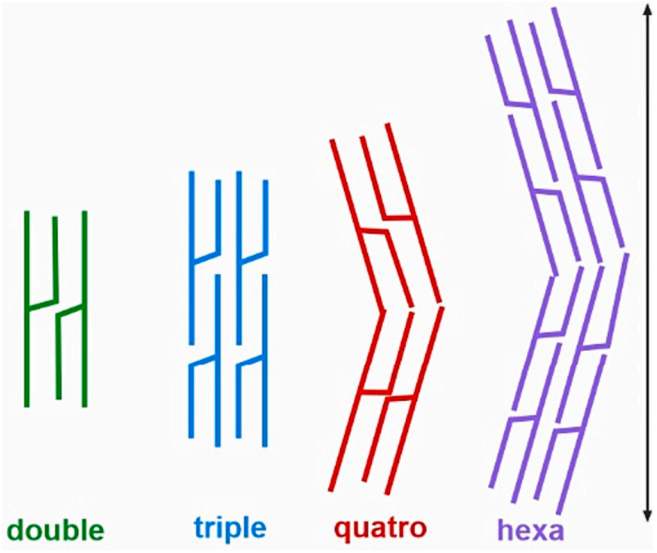

Fig. 4. Different TAG chain-length structures.

lattice from β' to β polymorph [14].

Different polymorphs adopt various subcell structures, defined as the cross-sectional arrangement of zigzag hydrocarbon chains, see Fig. 3c-e for illustration. In the α phase, molecules assemble into a hexagonal subcell (Fig. 3c), where acyl chains are disordered, allowing rotation of carbon atoms by several degrees around the long axis of the alkyl moiety [55–57,66]. This arrangement is observed in WAXS (wide angle X-ray scattering) spectrum with a single broad peak at 0.415 nm (equivalent to scattering vector $q \approx 15.3\ nm^{-1}$). The β' polymorph, with intermediate stability, possesses an orthorhombic subcell lattice where acyl chains are orthogonally oriented; it is denoted as $O_{\perp}$, see Fig. 3d. Its subcell parameters are typically shown by two WAXS peaks corresponding to 0.380 and 0.413 nm distances in real space ($q \approx 16.5\ nm^{-1}$ and $15.2\ nm^{-1}$). The most stable β polymorph has triclinic parallel subcell structure ($T_{\parallel}$), characterized by three primary patterns at distances of 0.368, 0.386 and 0.459 nm ($q \approx 17.1\ nm^{-1}$, $16.3\ nm^{-1}$ and $13.7\ nm^{-1}$), Fig. 3e. All mentioned distances specifically apply to saturated monoacid TAGs [54].

The chain-length structure of TAGs is defined as the number of repetitive hydrocarbon chains (leaflets) forming a unit lamella along the *c*-axis, see Fig. 4 [54]. This arrangement varies depending on the fatty acid composition. TAGs with identical or similar fatty acids typically adopt a double-chain-length structure. However, a triple-chain-length structure can arise when one of the fatty acids significantly differs from the others, as seen in $C_{16}C_{18:1}C_{16}$. In more complex systems with asymmetrical mixed-acid TAGs, quatro- and hexachain-length structures have been observed. The quatro-chain-length structure entails two double-chain-length structures aligned in alternative directions, while the hexachain-length structure consists of two triple-chain-length structures oriented oppositely [66–68]. Additionally, mixed-chain-length structures have been also identified [69].

3.2. Properties of triglyceride polymorphs

3.2.1. Melting temperatures

Table 1 presents selected thermal data for monoacid TAGs. Simple monoacid saturated TAGs of the $C_nC_nC_n$ type can be considered as homologous, as their melting temperatures lie on a smooth curve, see Fig. 5a [34,36]. Nonetheless, a pronounced even-odd effect arises due to the lower degree of symmetry possessed by odd-numbered chains in comparison to even-numbered chains [70,71]. This disparity is particularly pronounced within the most stable β-form of TAGs. This effect is ascribed to distinct intermolecular interactions occurring between the fully extended molecules. This principle is well known for alkanes [62,72,73] and other molecular classes featuring long saturated hydrocarbon chains, such as fatty acids and long chain fatty esters (methyl, ethyl, propyl and butyl esters) [74].

Accounting that the theoretical maximal melting temperature for polyethylene is 140 °C, it becomes possible to represent the melting temperatures of distinct TAG polymorphs using the relation [34]: $T_m = 140 - exp(a + bn + cn^2)$ or $ln(140 - T_m) = a + bn + cn^2$, where *a*, *b* and *c* are empirical constants which depend on the polymorphic phase, and T_m is the melting temperature of the given polymorph expressed in degrees Celsius. In this equation, as well as in all equations presented within the text, *n* denotes the number of C-atoms in a single fatty acid acyl chain within the TAG molecule. Applying this approach and using averaged data from literature regarding melting points, we derived the following equations describing the melting points of monoacid saturated TAGs with *n* varying from 10 to 24C-atoms, see Fig. 5b:

$$\begin{aligned} &\text{alpha}: ln(140 - T_{m,\alpha}) \approx 6.05076 - 0.12456n + 0.00195n^2 \\ &\text{beta prime}: ln(140 - T_{m,\beta'}) \approx 5.59355 - 0.09311n + 0.00130n^2 \\ &\text{beta odd}: ln(140 - T_{m,\beta,odd}) \approx 5.67541 - 0.10771n + 0.00167n^2 \\ &\text{beta even}: ln(140 - T_{m,\beta,even}) \approx 5.55694 - 0.10338n + 0.00158n^2 \end{aligned} \quad (1\text{-}4)$$

3.2.2. Enthalpies

Similar analysis can be performed for the enthalpies of fusion of TAGs. To the best of our knowledge, however, only one dataset is available for the enthalpies of odd-numbered molecules, reported about 40 years ago by Hagemann and Rothfus [70]. A comparison between the more widely available data for even-numbered monoacid TAGs and the solitary dataset for odd-numbered TAGs shows that this data is relatively scattered. Hence, we have opted not to include the odd-numbered TAG data in this context. Instead, we present only the enthalpies of fusion for even-numbered TAGs, see Table 1. These enthalpies display a linear increase in correspondence with the elongation of the fatty acid chains for molecules with 10 to 20C-atoms:

$$\begin{aligned} \Delta H_{m,\alpha} &= 2.31n + 82.5\ J/g \\ \Delta H_{m,\beta'} &= 4.15n + 88.1\ J/g \\ \Delta H_{m,\beta} &= 5.42n + 120.1\ J/g \end{aligned} \quad (5\text{-}7)$$

The β-to-liquid transition requires approximately 1 kcal per methylene group (-CH_2-), while the α-to-liquid transition requires around 0.8 kcal per methylene group. The 0.2 kcal disparity between these values approximates the enthalpy of the α → β transition [36]. The heat capacities at constant pressure, C_p, at 25 °C for monoacid saturated TAGs vary between 1.95 J/(g.K) for tricaprylin (CaCaCa, C_8TAG) and 2.23 J/g.K for tristearin [75]. The thermal conductivities of these monoacid saturated TAGs measured at 25 °C are ≈ 0.17 ± 0.03 W/(m.K) [77,78].

A semi-empirical model, able to estimate the melting points and enthalpies of fusion of mono- and mixed-acid TAGs, was developed by Wesdorp in Ref. [79]. Later on, this model was improved [69,80] and recently a software tool "Triglyceride property calculator" (TCP) was developed and implemented in a web application available at https://lipidlibrary.shinyapps.io/Triglyceride_Property_Calculator/ [81]. Currently, this calculator is able to predict the melting points and enthalpies of fusion for even-

Table 1
Molecular weights (M_w), melting enthalpies (ΔH_m) and temperatures T_m for different TAG polymorphs.

TAG	M_w, g/mol	*α phase*			*β' phase*			*β phase*			
		$\Delta H_{m,\alpha}$, J/g	$T_{m,\alpha}$, °C	*d*, nm	$\Delta H_{m\beta'}$, J/g	$T_{m,\beta'}$, °C	*d*, nm	$\Delta H_{fm\beta}$, J/g	$T_{m,\beta}$, °C	*d*, nm	ρ, g/ml
C_8TAG	470.7	37.8	-52.5	2.5	-	-19.3	2.3	146.0	9.7	2.2	-
C_{10}TAG	554.8	102.6	-11.4	3.0	-	16.3	2.8	168.4	31.6	2.4	-
C_{12}TAG	639.0	110.9	15.0	3.5	134.6	34.6	3.2	188.8	46.3	3.1	1.057
C_{14}TAG	723.2	116.5	32.3	4.1	146.6	45.8	3.7	199.0	57.5	3.6	1.050
C_{16}TAG	807.3	123.1	45.1	4.6	156.7	56.8	4.2	210.0	66.0	4.0	1.047
C_{18}TAG	891.5	123.8	54.8	5.05	169.9	64.0	4.6	217.8	72.8	4.5	1.043
C_{20}TAG	975.6	125.9	62.9	5.57	164.4	69.2	5.1	224.7	78.0	4.9	-

Melting temperatures are averaged from Table 1 in Ref. [75] and Ref. [36]. Enthalpies are averaged from Refs. [36,69,75]. Additional large set of data for other saturated and unsaturated, monoacid and mixed acid TAGs is available in Appendix 9.A of Ref. [69]. The long-space distances are from Ref. [34,36] and mass densities are from Ref. [36]. The missing information is indicated with "-" signs.

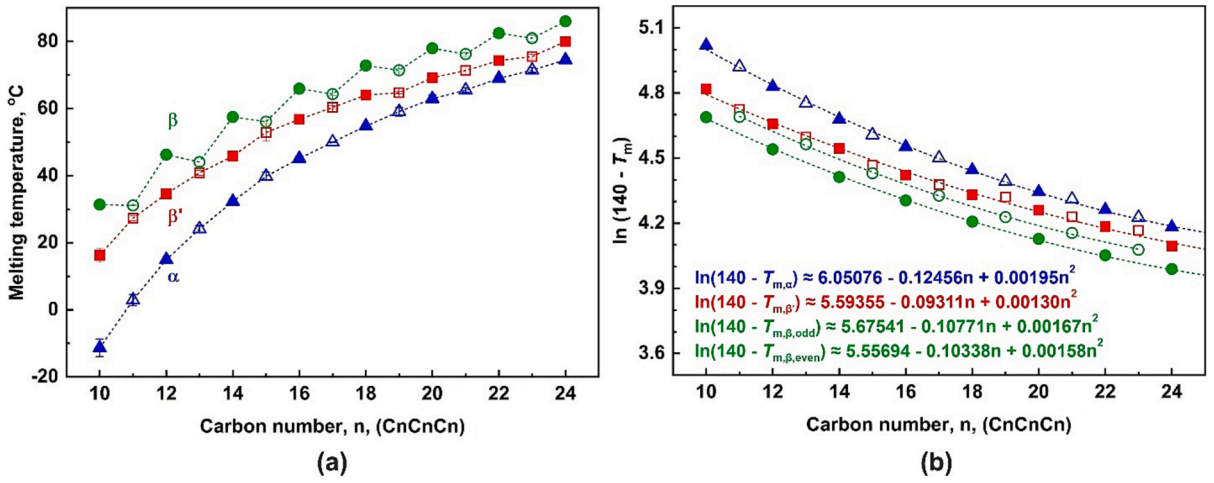

Fig. 5. Melting temperatures for monoacid bulk TAGs. (a) Melting temperature as a function of the fatty acid residue chain length in the TAG molecule. (b) Scaled melting temperature, ln(140-T_m) as a function of the fatty acid residue chain length. Data for α polymorphs are shown with blue triangles; β' – red squares and β – green circles. The data for odd-numbered TAGs are shown with empty symbols, whereas for even-numbered TAGs – with filled symbols. Data from Refs. [34, 36, 60, 75, 76] have been used to construct the plot. (For interpretation of the references to colour in this figure legend, the reader is referred to the web version of this article.)

numbered TAG molecules in α, β' or β polymorph containing chains with 4 to 22C-atoms using both Wesdorp model [69,79–81] and the method developed in Ref. [82]. Some of the widespread unsaturated chains are also included in the calculator. The underlying mathematical model requires description of the TAG molecule of interest – primarily, the chain lengths of FA residues and the number of double bonds in each FA residue. The position of each saturated/unsaturated FA residue, the C-atoms differences between the FA residues connected at *sn*-1 and *sn*-2/*sn*-3 positions are included as secondary and tertiary attributes in Wesdorp model. Further details about the mathematical models are available in the original papers [69,79–82]. However, we note that the authors who developed and tested the TCP calculator concluded that the calculated enthalpies of fusion are usually with higher precision compared to the predicted melting points which were often "physically unlikely" [81]. The efforts to develop a model for precise estimates of the thermodynamic properties continue, see *e.g.* Refs [83, 84]. The final aim is to advance a tool applicable not only to single-component mixed-acid TAGs, but also to mixtures of liquid and solid TAGs, and ultimately - to the natural fats and oils.

3.2.3. *Unit cell parameters and repeat distance of the layers*

The lattice long-spacing, denoted as *d*, for TAGs has been determined as well, see Table 1. The linear regressions representing the repeat distances are:

$$\begin{aligned} d_{\alpha} &= 0.259n + 0.410 \text{ nm} \\ d_{\beta'} &= 0.232n + 0.443 \text{ nm} \\ d_{\beta,even} &= 0.227n + 0.411 \text{ nm} \\ d_{\beta,odd} &= 0.233n + 0.391 \text{ nm} \end{aligned} \quad (8\text{-}11)$$

These equations are valid for monoacid TAGs with *n* ranging from 2 to 22 [34,36].

The cell parameters of the most stable β polymorphs have also been reported for certain monoacid saturated TAGs, see Table 2 [85–87]. The space group determined for β-TAGs is the centrosymmetric triclinic $P\bar{1}$. The average lengths of the cell parameters are: $a \approx 5.47$ Å, $b \approx 12.07$ Å, $\alpha \approx 73.6°$, $\beta \approx 100.5°$, and $\gamma \approx 118.7°$. The length of the long cell parameter, *c*, depends on the acyl chain length, displaying an increment of approximately 5.1 Å between successive members of the even series. This length is in good agreement with the average C—C bond length of 1.524 Å and the C-C-C (sp^3 hybridization) angle of 109.3° [87].

The temperature-dependent behavior of the lattice parameters for monoacid TAGs (C_{12}TAG to C_{18}TAG) has been studied as well [88]. The most pronounced temperature expansion was observed in the $(3\bar{1}0)$ WAXS peak ($d \approx 0.368$ nm), with an approximate rate of ≈ 0.13 Å/°C (calculated for the real-space distance). In contrast, the $(20\bar{1})$ peak ($d \approx$ 0.386 nm) exhibited a comparatively smaller shift in response to a temperature change, showing a temperature expansion of ≈ 0.06 Å/°C. The positions of the other peaks observed for the β phases in WAXS, including the characteristic (101) peak situated at $q \approx 13.7$ nm^{-1}), remained relatively unchanged within the temperature range of −20 °C to 40–60 °C (varied according to the melting temperature of the specific TAG under study) [88]. The *d*-spacings, respectively the positions of the peaks, were found to be reversible with changes in temperature [88]. The provided Miller indices are referenced according to Ref. [87].

3.2.4. *Mass density and voids formation*

In contrast to alkanes, where density increases with the chain length, the density of TAGs decreases in both liquid and crystalline phases as chain length increases [89]. This phenomenon is attributed to the reduced packing efficiency of longer chain length homologs compared to shorter ones [90]. Additionally, various studies have reported significant expansions (up to 20%) in many saturated TAGs during the transition from less stable to more stable polymorphs [91–93]. This behavior

Table 2
Unit cell parameters for β-TAGs. *a*, *b* and *c* are the unit cell lengths; α, β and γ are the unit cell angles and *V* is the unit cell volume. Data from Refs [85–87].

	β-C_{10}TAG (tricaprin)	β-C_{12}TAG (trilaurin)	β-C_{14}TAG (trimyristin)	β-C_{16}TAG (tripalmitin)	β-C_{18}TAG (tristearin)
a, Å	5.49	5.47	5.47	5.45	5.47
b, Å	12.18	12.08	12.07	11.95	12.07
c, Å	31.56	36.61	41.72	46.84	51.95
α, °	73.4	73.4	73.6	73.8	73.6
β, °	100.7	100.5	100.5	100.2	100.5
γ, °	119.2	118.7	118.7	118.1	118.7
V, Å^3	1761.3	2029.2	2314.2	2581.1	2881.7

is somewhat unexpected, considering that the macroscopic density of the crystalline phase is higher than that of the liquid TAG. For example, tristearin exhibits densities of 0.863 g/ml in its liquid phase, 1.014 g/ml for α, 1.017 g/ml for β', and 1.043 g/ml for β polymorph [36].

The anomalous expansion on cooling has been explained by the presence of molecular-sized voids within the crystalline structure of TAGs [93]. These voids are linked to the "negative pressure effect" which has been also observed during the crystallization of certain synthetic polymers [94]. Small angle neutron scattering (SANS) experiments have revealed voids with correlation lengths ranging from 9.3 to 63 nm in β_{LLL} [93]. In another study, the polycrystalline structure formed upon freezing of bulk tripalmitin and tristearin was successfully modeled as consisting of TAG grains with nanovoids between them. Ultra-small angle X-ray scattering (USAXS) data indicated that the average volume of these nanovoids is characterized by a radius of gyration of approximately 440 and 370 nm for PPP and SSS, respectively [95]. The presence of such nanovoids and the associated negative pressure effect have been found to play a significant role in the spontaneous cold-bursting process observed in emulsified TAGs, as detailed in Section 6.6 below.

3.2.5. Triglyceride properties studied by molecular dynamics simulations

In addition to experimental data, the advancement of powerful computational resources has enabled the execution of computational experiments. However, the high number of atoms present within a single TAG molecule (155 in the case of tripalmitin, for example) presents a challenge for conducting all-atom molecular dynamics simulations.

Among the available force fields, the NERD force field is the most commonly used one in computational studies of TAGs. Nevertheless, other force field like CHARMM-36 have also found use in certain investigations [96]. Using a modified NERD force field and 100 mono unsaturated TAG molecules ($C_{16}C_{18:1}C_{18}$, 1-palmitoyl-2-oleoyl-3-stearoyl-*sn*-glycerol), Cordina et al. demonstrated that the MD simulations can be successfully applied to predict the crystalline and liquid densities, as well as the dimensions of the crystalline state for this specific TAG [97].

In other studies, less computationally expensive, united atom models have been utilized to predict the macroscopic properties of TAGs. For example, Hsu and Violi successfully calculated the temperature dependence of the densities for LLL, SSS and OOO [90]. Similarly, other researchers have applied this method to predict the properties of various monoacid TAGs [98–100]. More recently, the Tuttle group has contributed several papers introducing a modified TAG optimized force field, referred to as COGITO (coarse-grained interchangeable triacylglyceride optimized). The authors demonstrated a good agreement between theoretically obtained results and experimentally measured data across various TAG properties, including density, lattice parameters, melting temperatures, and crystallinity [101–103].

These studies provide invaluable insights into the molecular arrangement of TAGs, which cannot be fully accessed through direct experimental methods at the moment. For instance, see the discussion in Section 4.2 below regarding the mixture of tripalmitin and tristearin molecules [104]. We anticipate that the research in this field will progress even more rapidly in the coming years, further enriching our understanding of these intriguing systems.

3.3. Effect of additives and other external factors for bulk triglycerides crystallization

3.3.1. External factors - temperature profile

One of the most critical factors which should be considered when studying liquid-to-solid phase transitions is the thermal profile used to induce the crystallization process. While isothermal crystallization from a solvent can yield monocrystals, this method is notably time-consuming (taking months to years) [33]. As a result, molten TAGs are typically subjected to isothermal crystallization at a specific temperature below their melting point or cooled with a constant cooling rate. In such cases, a polycrystalline structure is formed, comprised of multiple crystalline domains. According to classical crystallization theory, when the driving force for crystallization is decreased temperature, less stable polymorphs crystallize more rapidly compared to the more stable forms [105,106]. Furthermore, it is expected that the crystallization rate will increase when the temperature decreases, *i.e.* upon larger supercooling. The nucleation rate, J, dependence on the temperature can be expressed as an Arrhenius equation:

$$J = Aexp\left(-\frac{\Delta G^*}{RT}\right), \tag{12}$$

where A is the pre-exponential factor accounting for the nucleation kinetics and the rates of attachment and detachment of lipid molecules between crystalline clusters and molten environment, ΔG^* is the activation free energy for nucleation, T represents the temperature and R denotes the universal gas constant [105]. Moreover, the activation free energy for nucleation can be expressed as:

$$\Delta G^* = K\frac{\gamma^3}{\Delta\mu^2}, \tag{13}$$

where K is a constant, γ is the interfacial energy between the liquid phase and crystalline nucleus, and $\Delta\mu$ is the chemical potential difference between the liquid and crystal. The interfacial tension between the crystal nucleus and the melt for the mixed SSS-CCC (tristearin-tricaprin) TAG system has been estimated to be abound 4 mN/m [107]. The chemical potential difference can be expressed as:

$$\Delta\mu = \frac{\Delta H_m \Delta T}{T_m}, \tag{14}$$

where ΔH_m is the enthalpy of melting, T_m is the melting temperature and ΔT is the supercooling, *i.e.* $\Delta T = T_m - T$ [105].

Typically, TAG samples tend to crystallize first into the least stable α polymorph when rapidly cooled from a molten state. Lower cooling rates and/or smaller supercooling conditions are required to achieve a direct crystallization into the more stable β' or β polymorphs. A study conducted by Sato and Kuroda [57] provides an example supporting these general crystallization principles. This study investigated the kinetics of isothermal crystallization of molten PPP samples cooled to different temperatures, see Fig. 6a [57]. The results revealed that the crystallization rate increased in the order α > β' > β. Moreover, it was observed that the melt-mediated polymorphic transition at a given temperature occurred faster compared to the solid state transition, as seen in the comparison between the empty green squares and pink triangles shown at $T > 45$ °C in Fig. 6a. The results also demonstrated that the transformation rate is slower than the crystallization rate for a given polymorph at the same temperature (compare the empty and filled symbols of the same type in Fig. 6a).

The increase in crystallization rate with larger degrees of supercooling is commonly attributed to the formation of a higher in number of smaller in size crystalline domains [105,111]. This phenomenon is often associated with the simultaneous growth of multiple nuclei. Recently, Co and Marangoni proposed a model for fat crystallization using thermodynamic and mass-transfer variables [111]. The authors argued that this outcome is not solely driven by the formation of a larger quantity of crystalline nuclei, but also arises from the impeded mass transfer observed at low temperatures. They correlated the viscosity of the molten material at the start of the crystallization process, suggesting that larger crystal sizes would be observed in samples with lower viscosities (*i.e.* crystallizing at higher temperature), whereas smaller crystalline domains would emerge under higher degrees of supercooling. Consequently, the unfavorable mass-transfer conditions at low temperatures inhibited crystal growth, resulting in the formation of smaller crystalline domains [111].

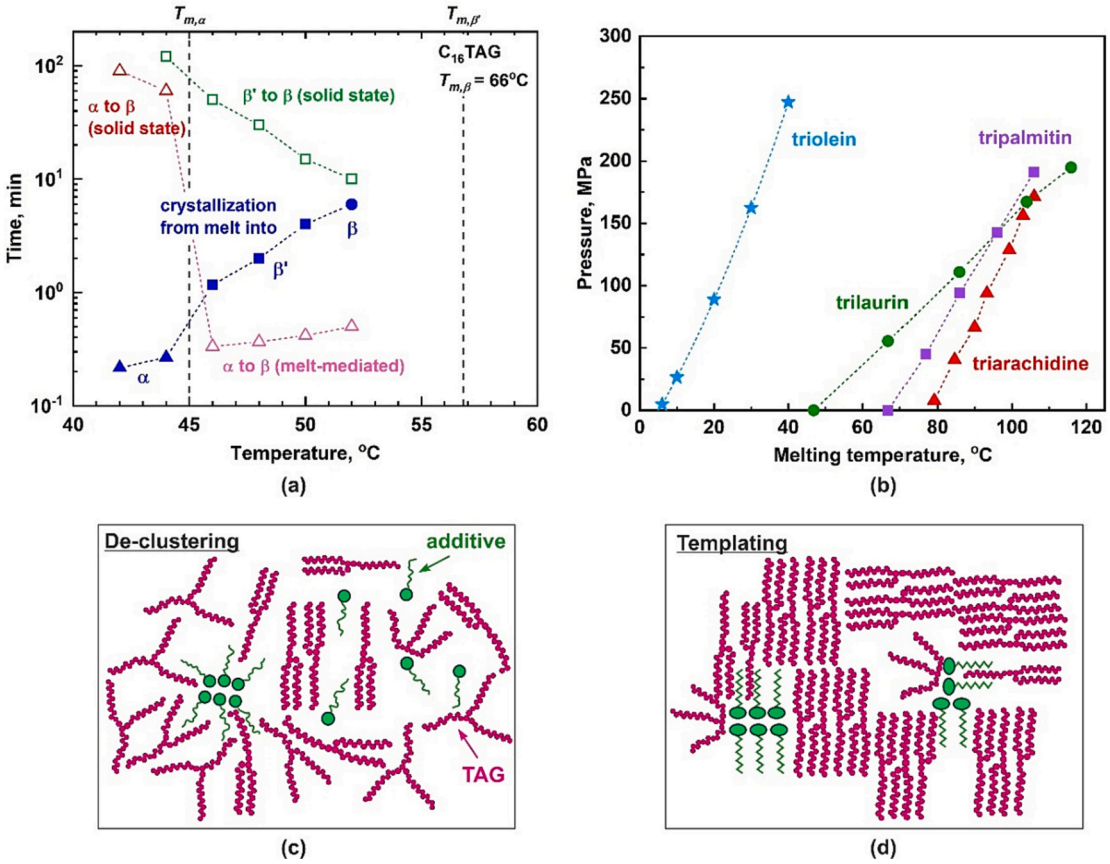

Fig. 6. Impact of external factors on the TAG crystallization. (a) Effect of temperature. Time required for tripalmitin crystallization (blue filled symbols) or polymorphic phase transition (empty red, pink and green symbols) is depicted as a function of temperature. The experiments were performed under isothermal conditions. Different polymorphs are denoted by distinct symbols: α – triangles, β' – squares, and β – circles. Data from Ref. [57]. (b) Effect of pressure on the melting temperature of β-TAGs. Blue stars: triolein ($C_{18:1}$TAG); green circles – trilaurin (C_{12}TAG); purple squares – tripalmitin (C_{18}TAG) and red triangles – triarachidine (C_{20}TAG). Data from Refs. [108–110]. (c,d) Effect of additives. Two opposite scenarios are possible – additives might either promote crystal nucleation and growth (templating effect) or hinder it (de-clustering effect). Further detailed explanations are provided in the text. (For interpretation of the references to colour in this figure legend, the reader is referred to the web version of this article.)

3.3.2. Other external factors affecting the TAG crystallization process

In addition to thermal treatment, the crystallization behavior of TAGs can be influenced by various external factors, including applied pressure, shear, and sonication.

The crystallization of LLL and OOO under applied pressure has been studied in Refs. [108–110, 112]. The results indicate that increased pressure had a similar effect to those of decreased temperature. Specifically, higher pressures led to reduction in nucleation induction time and to increase in the crystallization growth rate. Additionally, an increase in the melting temperature of TAGs was observed under higher pressures, as shown in Fig. 6b [108–110]. These findings are in good agreement with the Clausius-Clapeyron relation that describes the pressure-temperature (*p-T*) phase diagram for a given material:

$$\frac{dp}{dT} = \frac{\Delta H_m}{T\Delta V}, \tag{15}$$

where dp/dT is the slope of the tangent curve separating the liquid and solid region in the *p-T* phase diagram, ΔH_m is the molar enthalpy of fusion, and ΔV is the difference in the molar volume between the liquid and crystalline states [105]. As the melting temperature increases upon application of hydrostatic pressure at given temperature, the supercooling will increase, thereby enhancing the driving force for nucleation and crystal growth [105].

Another factor known to influence the TAGs crystallization is the application of shear [105,110–116]. This influence is particularly significant for products with high fat content, such as chocolates, margarine, and butter, where the properties of the fat crystals substantially impact end product characteristics, such as appearance, spreadability, and texture [105,114]. The application of shear has been observed to accelerate the rate of polymorphic transformations in lipids. Notably, with the development of specialized experimental set-ups in synchrotron facilities, it has become possible to monitor *in-situ* the lipid microstructure evolution under shear flow. These studies have revealed that the aggregation microstructure is also influenced by the application of shear, leading to the formation of an oriented crystal network [105,113,115]. In specific experiments with cocoa butter samples crystallized under shear, an increase in the Young modulus and elastic storage modulus was demonstrated [117,118]. Further insights into the effect of shear effect on lipid crystallization can be found in Ref. [105].

The impact of ultrasound on crystallizing TAG was investigated in various studies [105,119–122]. Similarly to the effects observed with the application of pressure or shear, sonication led to a notable acceleration in the crystallization rate of tripalmitin β' and β polymorphs during isothermal crystallization. Additionally, the application of sonication also decreased the induction time for nucleation, resulting in an increased number of crystals forming in the sample [119,122]. Furthermore, when sonication was used during an isothermal crystallization of trilaurin or tripalmitin, the most stable β polymorph was observed to form solely, while under equivalent thermal conditions without ultrasound treatment, both β' and β crystals were detected [122].

Next, we consider the effect of additives over the crystallization

process.

3.3.3. Effect of additives

In the real TAG-containing systems, TAG molecules are typically found in complex mixtures that include other chemical compounds, such as surfactants, monoacylglycerols (MAGs), diacylglycerols (DAGs), free fatty acids, phospholipids, glycolipids, and others. The presence of these minor components can significantly impact the crystal nucleation and growth through two distinct pathways [93,105,123–128]. Firstly, they can promote and accelerate the nucleation and growth processes. Alternatively, they may act as retardants, see schematics in Fig. 6c,d.

The nucleation promoting effect is often associated with a templating effect, which becomes apparent when additives share structurally similar acyl chains with the crystallizing TAG molecule and are present at concentrations exceeding their solubility limit. Under these conditions, the additives may crystallize before the TAG, acting as templates for the other TAG molecules to grow on, thereby accelerating the overall crystallization rate, see Fig. 6d [105].

Direct experimental evidence supporting the templating effect was acquired in Ref. [129]. In this study, the authors investigated the structural aspects of palm oil crystallization in the presence of 8 wt% pre-dissolved monopalmitin (C_{16}MAG), using a microbeam X-ray diffraction method with a beam size of 5 × 5 μm^2. Their investigation demonstrated that the pre-crystallized MAG indeed promoted the crystallization of palm oil and aligned the palm oil crystals. However, during the course of storage, the palm oil and monopalmitin crystals separated. This separation was likely due to the Ostwald ripening process of the monopalmitin crystals, which migrated and concentrated into larger spherulitic crystals [129].

The templating effect holds significance not only for surfactant-TAG systems but also for the crystallization of TAGs in the presence of other longer chain TAGs [130]. This effect was demonstrated in a study exploring the isothermal crystallization of coconut oil in the presence of longer chain length monoacid TAGs seeds. The study revealed that PPP or SSS seeds promoted the crystallization of coconut oil (CNO) regardless of the polymorphic form of the saturated TAG seed. A reduction in the crystallization induction time from 12 min (for CNO without added seeds) to 1.5–6.5 min in the presence of seed crystals was observed at 20 °C. Among the crystallization promoters, the β' seed crystals proved to be the most effective, with an induction time of 1.5 min for β'_{PPP} and 2 min for β'_{SSS} seed crystals. This phenomenon was attributed to the matched lattice structures between the crystallizing CNO and the nucleation seed. Note that the thermodynamically stable polymorph for CNO is the orthorhombic β'. Therefore, the presence of β' seed crystals accelerated the CNO nucleation by epitaxial growth [130].

An increase in the onset crystallization temperature was also observed when saturated MAGs were dissolved in coconut oil, which primarily consists of TAG molecules with saturated acyl chains [123]. Similarly, an increase in the onset crystallization temperature was observed for unsaturated MAGs crystallizing with palm olein [123], whereas saturated MAGs of hydrogenated palm oil accelerated both nucleation and crystallization rates in palm oil [124].

Conversely, when additives are present at lower concentrations, they may retard the crystallization processes by preventing nucleus formation. This "de-clustering" effect is typically attributed to the attractive molecular interactions between the additive and TAG molecules, thus causing a hindered nucleation or alternatively – hindered crystal growth by coating the already formed nuclei (steric hindrance) [105,123]. Additives having significantly different acyl chains compared to those of the TAGs exert a lesser influence on the crystallization processes.

At the molecular level, the presence of vacancies in the crystalline lattice of TAGs has been observed when the TAGs crystallize in the presence of surfactant molecules [105,127]. Studies show that selected emulsifiers may be incorporated within the TAG lattice at concentrations of 10 wt% without changing it [127]. However, as the surfactant molecules are smaller than the TAG molecules, their incorporation leaves unfilled space that enhances the mobility of the neighboring molecules [128]. This mobility promotion effect was found to be significant for the β phase. In contrast, no significant changes were observed in the α phase because, the hydrocarbon chains are not well oriented here even in the absence of additives [55–57,66]. A stronger effect was observed at lower surfactant concentrations (up to about 8 wt %), whereas it reached saturation for higher surfactant concentrations (10 wt% or more) [128].

The presence of emulsifiers upon TAG crystallization can also influence the sizes of TAG particles formed [131]. In experiments where long-chain SSS was dissolved in soybean oil and then flash-cooled to liquid nitrogen temperature, the influence of the addition of polyglycerol polyricinoleate (PGPR) surfactant was studied. The results showed that the size of the obtained particles was affected by the PGPR/SSS *w*/w ratio. Specifically, when this ratio was below 1, larger particles were formed, with sizes of approximately 1 μm for PGPR/SSS = 0.5 and around 2 μm for PGPR/SSS = 0.25. In contrast, when this ratio was 1 or higher, the average size of the formed tristearin particles was approximately 300 nm [131].

The impact of the presence of organic or inorganic solid particles on the crystallization of molten TAGs has also been investigated [125,126]. The main difference between these additives and the previously considered surfactant molecules is the absence of hydrocarbon chains, as well as their negligible (or zero) solubility in the TAGs. Consequently, they serve as seeds for a heterogeneous nucleation process, regardless of the considered concentration or temperature conditions.

Experiments with molten trilaurin, trimyristin and tripalmitin samples with added 1 wt% particles showed that in all cases, the initial crystallization temperature increased by 1 to 8 °C (*e.g.*, for the trilaurin + graphite sample) compared to the initial crystallization temperatures observed in the absence of additives [125]. Furthermore, these particulate additives were observed to promote crystallization into more thermodynamically stable polymorphs. In the case of trilaurin, an increase in talc particles concentration or a reduction in their sizes was found to enhance the crystallization process [126]. The structural characteristics of the resulting crystals remained unaffected by the presence of additives, as demonstrated by X-ray diffraction measurements. Notably, the presence of additives did not impact the melting points of the samples [125,126].

4. Polymorphism in mixtures of triglycerides

In this section the phase behavior of model monoacid TAG mixtures is reviewed. These investigations are primarily conducted to provide a framework for understanding the considerably more complex phase dynamics exhibited by natural TAG oils. In Section 4.1, we examine the fundamental categories of TAG mixing. Section 4.2 presents the main features observed in the phase diagrams for binary TAG systems, along with a summary table outlining the main phase diagrams documented in the literature. Section 4.3 discusses the mixing of more complex TAG systems. The kinetic aspects of TAG mixtures crystallization are discussed in Section 4.4, while Section 4.5 presents an overview of the available information concerning the TAG mixing with other chemical compounds.

4.1. Types of triglyceride mixing

Triglyceride mixing leads to a rich phase behavior and formation of various polymorphs. Three main types of mixing behavior have been identified for bulk TAGs: miscible solid solution phases, immiscible eutectic phases and molecular compound forming phases, see Fig. 7 [132].

A miscible solid solution is formed when all molecules in a binary or more complex mixture crystallize simultaneously, and neither of the components solidifies without containing some fraction of the other component. In this scenario, only two phases can exist – a homogeneous

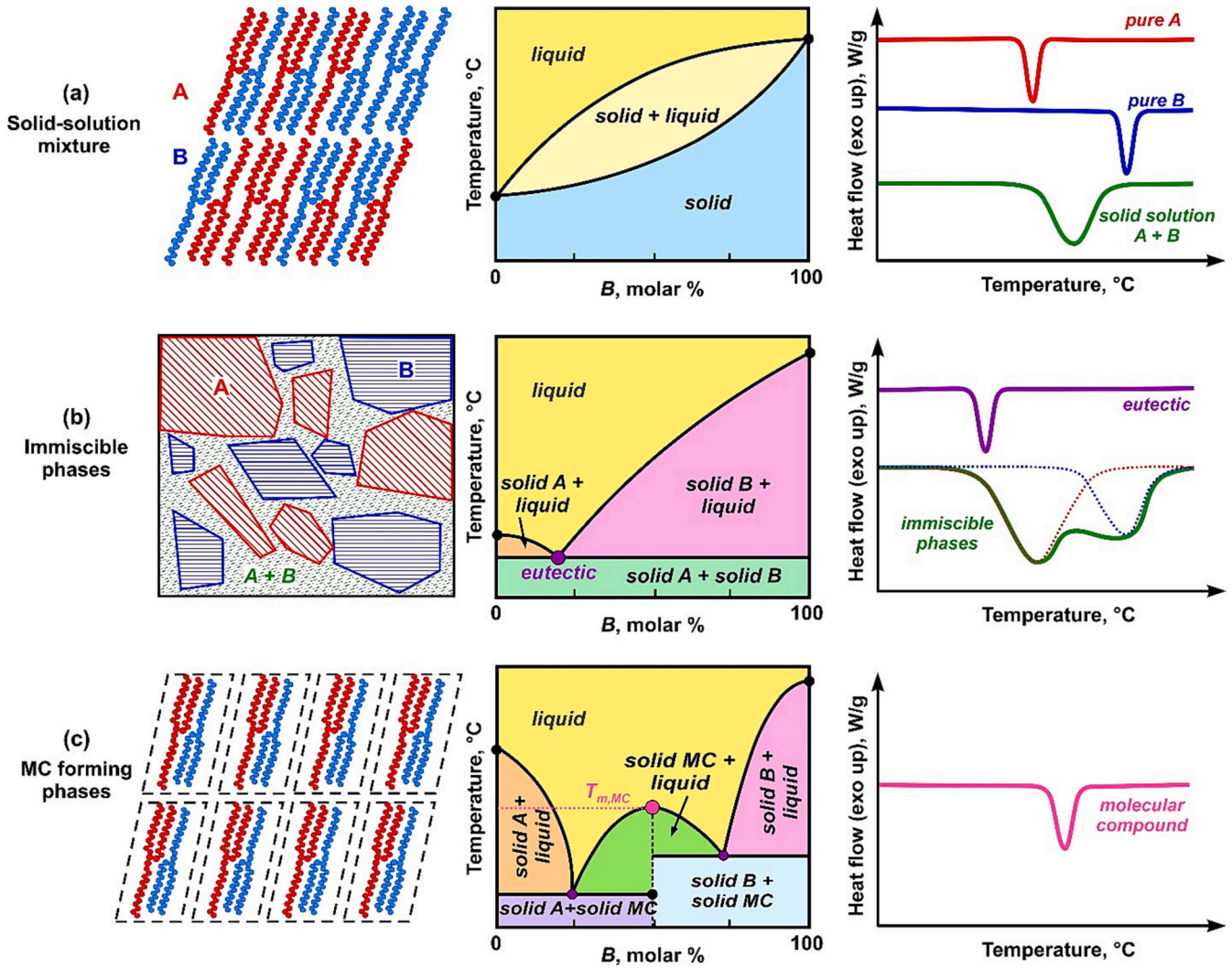

Fig. 7. Mixing behavior observed in TAG systems. (a) Solid-solution mixture. (b) Formation of immiscible eutectic phases. (c) Molecular compound forming mixture. Schematic representation of the molecular arrangement, typical phase diagram and DSC (differential scanning calorimetry) signal which would be detected upon heating of different TAG mixtures are shown in each case. Adapted from Ref. [132] and expanded.

liquid solution or a solid solution, see the phase diagram shown in Fig. 7a. Notably, solid solution mixtures exhibit a single melting point with a maximum situated between the melting points of the pure components, see Fig. 7a. This behavior is commonly observed in chemical compounds that have similarities in terms of melting points, chain lengths, polymorphic forms, and molecular volumes [132].

The prevalent phase behavior observed in mixtures of TAGs is the formation of immiscible eutectic phases, see Fig. 7b. Within these mixtures, TAG molecules phase separate into distinct domains characterized by different compositions and structures. Immiscible phase-forming mixtures exhibit distinct melting temperatures, corresponding to the individual melting points of the components within the mixture [132]. In the X-ray scattering curves, this behavior is reflected with the presence of wide peaks with multiple maxima.

The formation of eutectic is usually associated with the reduction in the crystalline order within the layers due to the higher number of structural defects resulting from the combination of two different types of molecules. This diminished order leads to enhanced molecular mobility and a lower melting point for the resulting mixture when compared to the pure constituents, see Fig. 7b [104,132].

The third type of mixed phases, *i.e.* those of molecular compounds (MCs) are defined by their distinct structural and thermodynamic characteristics that differ significantly from those of the individual TAGs [132]. These MCs are typically observed in systems where specific interactions occur between the different molecular species, allowing the stabilization of aliphatic chain packing and glycerol-glycerol arrangement upon MC formation [133]. Systems that form MCs exhibit a single, narrow melting peak, and the position of the peak maximum shifts as the proportion of one of the components changes [133]. The phase diagram for MC-forming systems essentially consists of two distinct eutectic-forming phase diagrams, denoted by the vertical dashed line in Fig. 7c.

Molecular compounds have been primarily observed in mixed-chain TAGs, particularly when at least one of the FA is unsaturated, for example in $C_{16}C_{18:1}C_{16}$-$C_{18:1}C_{16}C_{18:1}$, $C_{18}C_{18:1}C_{18}$-$C_{18}C_{18}C_{18:1}$, and others [65,140–145]. The prevalence of oleoyl chains ($C_{18:1}$) in these mixtures suggests that the main driving force for the formation of molecular compound is the π-π interaction among olefinic groups [65]. However, a molecular compound has been also observed for enantiomer mixture of *sn*-10:0/10:0/16:0 ($C_{10}C_{1_0}C_{16}$) and *sn*-16:0/10:0/10:0 ($C_{16}C_{10}C_{10}$) [45]. Therefore, further investigations are needed to provide a detailed explanation for this peculiar behavior.

4.2. Mixing in binary triglyceride systems

Nearly a century ago, the Joglekar and Watson [136] presented one of the first phase diagrams for a binary mixture of tripalmitin and

tristearin. This diagram showed a eutectic point at approximately 72% PPP + 28% SSS, see Fig. 8a. Later on, the phase behavior of diverse binary monoacid saturated mixtures was studied by other researchers, see Refs. [69, 132, 134–139, 146–151] and Table 3. In most of these studies, the eutectic phase behavior prevails within the β phases, whereas miscible solid solutions emerged for TAG mixtures crystallizing in both the α and β' phases, particularly when the samples undergo rapid cooling from their molten state [149,150].

In addition to the polymorphic form, the mixing/demixing behavior in TAGs is also influenced by the chain length disparities of the fatty acid residues [139]. When the chain length difference is relatively small, up to 2C-atoms ($\Delta n \leq 2$), TAGs tend to form completely miscible metastable α and β' phases. However, for systems with larger chain length differences, partial phase separation is observed, particularly in systems like LLL-PPP or LLL-SSS mixtures, see Fig. 8b [54,104,132,139].

4.2.1. Alpha phases

The miscibility of binary TAG mixtures with a chain length difference of $\Delta n = 2$ in α phase is attributed to the considerable molecular freedom of acyl chains, particularly of the carbon atoms near the chain-end. As already discussed, this makes α phase somewhat similar to the rotator phases observed in alkanes, which allows deviation from the optimal packing and formation of mixed α phases [55–57,61,62]. Although it has been generally accepted that a single mixed solid solution forms in rapidly cooled binary TAG mixtures with a chain length difference $\Delta n = 2$, newly obtained experimental results suggest that more than one mixed solid solution of α phase type may form in such mixtures [148,149,151].

One of the earliest reports indicating the potential formation of multiple α-forms can be found in Ref. [151], where an equimolar mixture of tripalmitin and tristearin was investigated. The authors observed the formation of a single symmetrical peak in SAXS at 48 °C. However, upon further cooling to 45 °C, a shoulder peak emerged at a higher angle, indicating a shorted *d*-spacing. In a more recent study, Himawan et al. [148] investigated the phase behavior of this mixture at different TAG ratios. The researchers concluded that two co-existing α phases are observed in mixtures containing 40 to 80% SSS when cooled at rates between 1 and 20 °C/min [148].

In another study, we observed similar demixing in the α-forms of

Table 3
Literature for phase behavior of monoacid saturated mixtures of TAGs. Most of the data is obtained *via* (synchrotron) X-ray scattering measurements.

Mixture	Phase behavior	References
$C_{12}TAG$ + $C_{14}TAG$	α, β' – miscible solid solution phase β – phase separation, eutectic phase $C_{12}TAG > 90\%$ - PPP incorporated inside the LLL crystals: α_{LLL}, β'_{LLL}, β_{LLL}	[139]
$C_{12}TAG$ + $C_{16}TAG$	$C_{12}TAG < 50\%$: LLL dissolved in PPP phases: $\alpha_{PPP} \rightarrow \beta_{PPP}$ $50\% < C_{12}TAG < 90\%$: β'_{LLL} + $\alpha_{PPP} \rightarrow \beta_{LLL} + \beta_{PPP}$ eutectic phases for all polymorphs	[69,137,139,146]
$C_{12}TAG$ + $C_{18}TAG$	Analogous to LLL + PPP	[69,137,139,147]
$C_{14}TAG$ + $C_{16}TAG$	β: MMM < 15%, MMM – dissolved in PPP otherwise – eutectic phases	[69]
$C_{16}TAG$ + $C_{18}TAG$	α, β' – miscible solid solution phase β – phase separation, eutectic phase	[69,104,116,134–138,148,149]
$C_{16}TAG$ + $C_{20}TAG$	Eutectic	[69]
$C_{18}TAG$ + MCT*	MCT > 2.5 wt% promotes formation of β phase	[152]
$C_{18}TAG$ + $C_{20}TAG$	Eutectic	[69]
Other binary saturated TAG mixtures with mixed acyl chains		[54,69,153–156]

* MCT = medium chain TAGs containing predominantly CaCaCa and CCC TAGs.

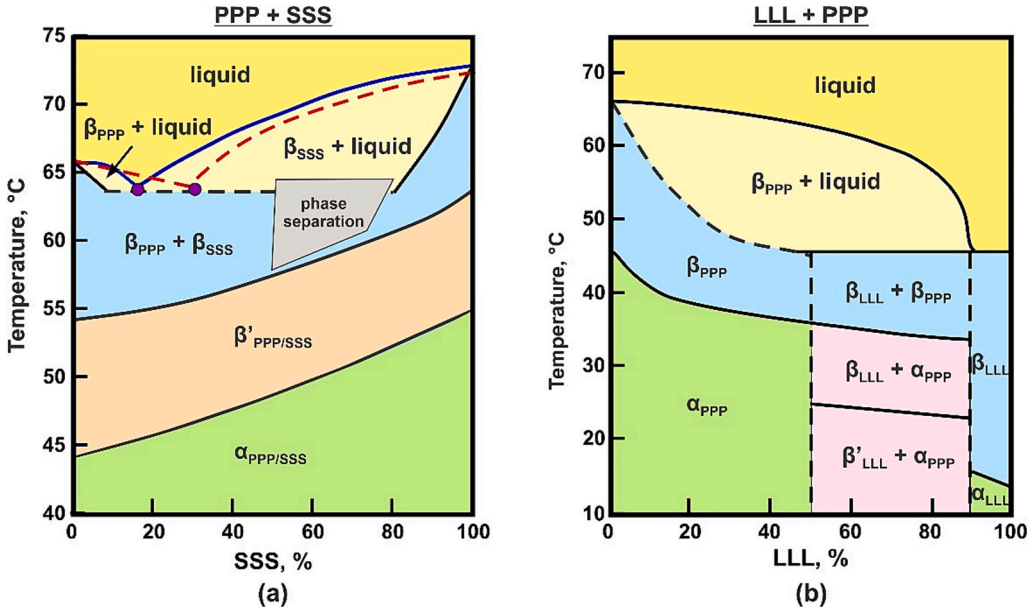

Fig. 8. Typical phase diagrams for binary TAG mixtures. (a) Tripalmitin-tristearin mixture ($\Delta n = 2$). Formation of mixed solid solutions is reported for α and β' polymorphs, whereas phase separation and eutectic phase is observed in the most stable β polymorph. Adapted from Ref. [134]. Blue and red lines show the melting temperature of β phase as reported in Ref. [69, 134, 135] and [104,136–138], respectively. Note that later studies reported a partial phase demixing even for α and β' phases, see text for more details. (b) Trilaurin-tripalmitin mixture ($\Delta n = 4$). A partial phase separation is reported for this mixture even in the least stable α- and β'-forms. Adapted from Ref. [139]. Note that these phase diagrams show the largest possible area of existence for α, β', and β polymorphs. The TAGs have monotropic behavior, *i.e.* the β phase has lowest Gibbs energy for the whole temperature interval and once formed, the phase transition is irreversible unless the sample is melted. (For interpretation of the references to colour in this figure legend, the reader is referred to the web version of this article.)

other binary TAG mixtures with $\Delta n = 2$, including LLL-MMM and MMM-PPP [151]. This phase separation became evident when examining the tertiary SAXS peak, see Fig. 9a. In this reflection, two distinct maxima were clearly observed, although there was a slight overlap between the peaks. It is worth noting that this difference in peak positions is three times smaller when considering the primary SAXS reflection, making it potentially easy to be overlooked, as the main d_{001} reflection often exhibits a shape close to Gaussian. Nevertheless, by performing experiments with various cooling rates (ranging from 1 °C/min to 25 °C/s), we demonstrated that α phase separation consistently occurred, regardless of the cooling protocol. In all cases, a phase enriched in longer TAG molecules was formed at higher temperatures, while the main fraction of the shorter molecules crystallized alongside with a small fraction of the longer TAGs at lower temperatures, see Fig. 10a,b [151].

A detailed analysis of the peak positions shows that the repeat distance of the layers in the mixed systems consistently falls between those of the pure α_{LLL} and α_{MMM}, see Fig. 9b. Furthermore, both d_{001} distances decreased with an increase in the concentration of the shorter LLL molecules. These findings indicate that there is no specific LLL to MMM ratio where the molecules assemble together in the mixed α phase. Instead, their ratio within a given phase depends on the total number of molecules present in the crystallizing sample. Formation of pure α_{LLL} crystals was observed for LLL concentrations exceeding 83 wt% in the mixture [151].

As initially proposed by Pizzirusso et al. [104], the most probable explanation for the intermediate lamellae spacings in the two α-forms is that the terminal ethyl groups of longer TAG molecules protrude between the neighboring lamellae. This protrusion results in a "steric repulsion", leading to an increased distance between the corresponding planes in the mixed phase relative to the pure phase of the shorter TAG [104,151]. This hypothesis is supported also by the results obtained with coarse-grained MD simulations for tripalmitin-tristearin binary mixture [104], see the discussion for β-forms below.

The mass density of the α phases in SSS-PPP mixture was found to decrease monotonically with the increase of PPP concentration, see the green triangles in Fig. 11a [89]. We should note, however, that the MD simulations only revealed the formation of one mixed α phase, characterized by a predominantly random distribution of SSS and PPP molecules within the layers. This result could be attributed to the relatively small size of the used model (comprising a total of 270 TAG molecules) and to the considerably higher cooling rate applied in the simulations. Even the fastest cooling rate achievable in experiments, attained by directly inserting a molten sample into a pre-cooled chamber, remains about seven orders of magnitude lower compared to the quenching procedure modeled in the MD simulations [151].

The mixed α crystals underwent polymorphic transformations into β'- or β-forms upon heating at temperatures close to the bulk melting temperature of the shorter TAG present in the mixture or when the samples were stored for a prolonged period of time [151]. For LLL-MMM mixtures crystallized in α-form, the transition directly led to the formation of the most stable β polymorph, even though some very short-living β' crystals (undetected in our experiments) could be formed in the experimental procedure used [151].

4.2.2. Beta phases

In mixed TAG systems, β phases typically exhibit eutectic demixing behavior. This phenomenon underscores that the most stable polymorph is significantly less tolerant of deviations from optimal packing compared to the α and β' phases.

The decrease in the melting point at the eutectic composition is attributed to the less effective packing of the TAG molecules in the crystals, resulting from the protrusion of the terminal ethyl groups of the longer TAG into the interlamellar spacing [104]. Moreover, results from MD simulations studies on PPP-SSS mixtures indicated that the 7:3 PPP:SSS mixture (which is the closest one studied to the eutectic composition, see Fig. 8a) has the lowest density and, correspondingly, the highest number of defects (voids) in the interlamellar space due to the inclusion of incompatible molecules, see Fig. 11 [104]. This higher disorder resulted in a slightly lower melting temperature for this composition. The MD simulation demonstrated also that the acyl end-chains of the longer SSS molecules exhibit significantly greater conformational freedom when surrounded by the shorter PPP molecules, in contrast to the limited freedom of the terminal groups in PPP molecules surrounded by longer SSS molecules. This result also supports the conclusion that the longer acyl chains of SSS molecules primarily disrupt the packing due to their end-chains being unable to fit well within the crystalline structure of the shorter PPP molecules [104].

Detailed SAXS/WAXS study of saturated monoacid TAG mixtures

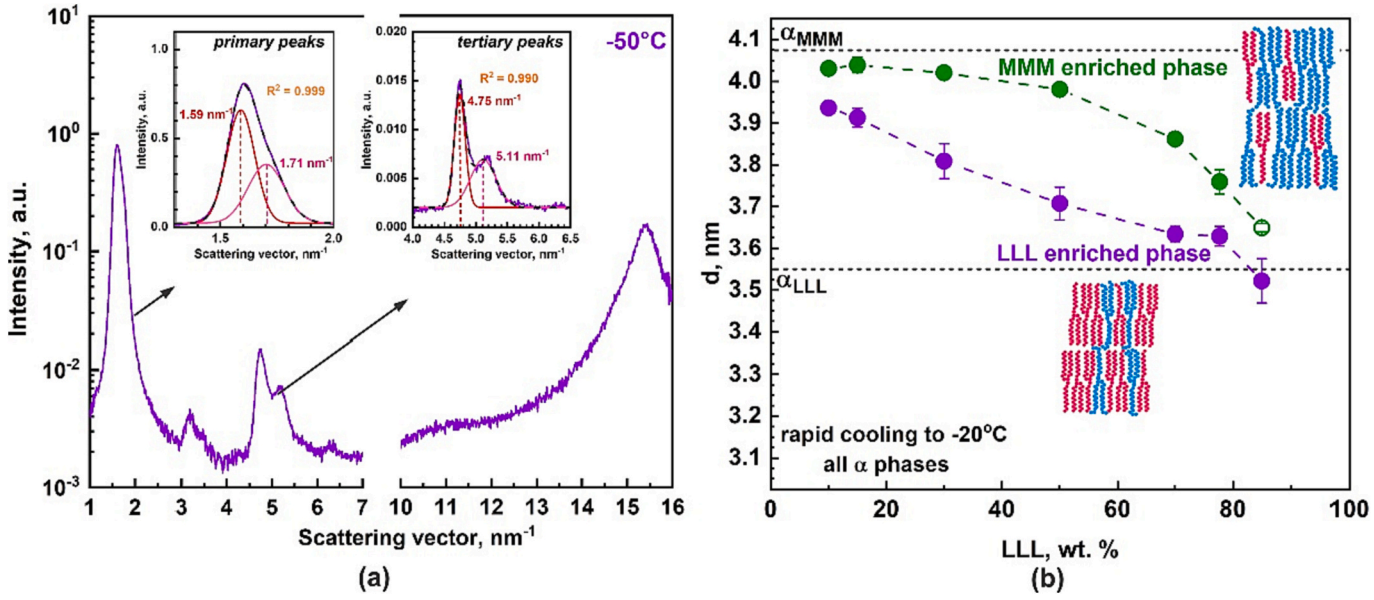

Fig. 9. Demixing of the alpha phase observed in LLL-MMM mixtures. (a) SAXS/WAXS spectra of a bulk LLL:MMM = 1:1 mixture, obtained after rapidly cooling the sample from its melt to −50 °C. The inset displays the peak deconvolution analysis, revealing the presence of two co-existing α phases. (b) Lamellar spacing in the mixed α phases formed upon rapid cooling from the melt to −20 °C. Two points are shown for each LLL-MMM composition as two different types of domains are observed. Adapted from Ref. [151]. Copyright © 2023, American Chemical Society.

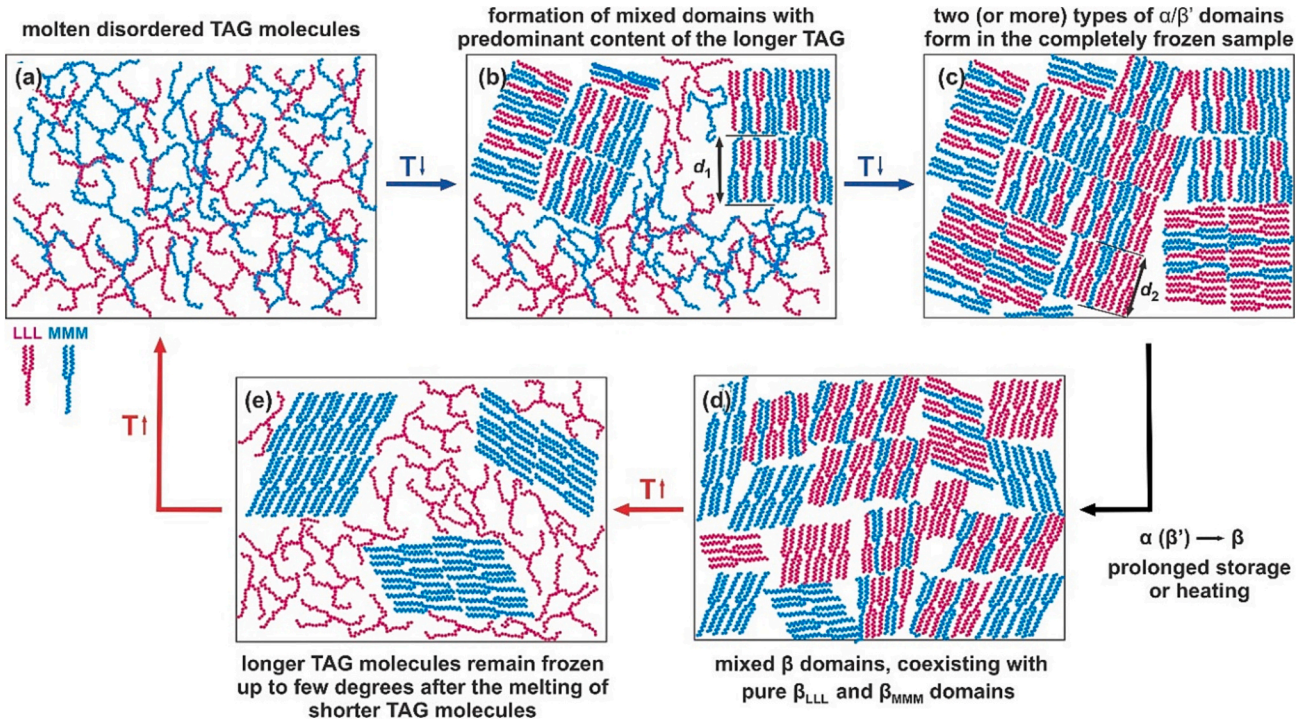

Fig. 10. Illustrative presentation of the molecular reconfigurations observed during the cooling and heating processes of a binary LLL-MMM mixture. Reprinted with permission from Ref. [151]. Copyright © 2023, American Chemical Society.

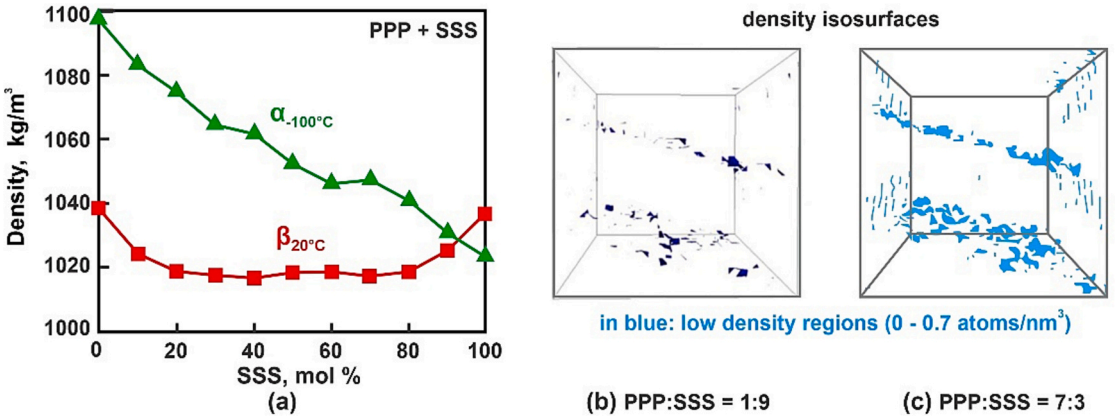

Fig. 11. Results from coarse-grain MD simulations for PPP-SSS mixtures. (a) Densities calculated for α phases at −100 °C (green triangles) and β phases at 20 °C (red squares) for SSS-PPP mixtures. (b,c) Density isosurfaces for β phase formed in PPP:SSS = 1:9 and 7:3 systems shown in (b) and (c) respectively. The blue colored areas show the regions in which the density is found to be between 0 and 0.7 atoms/nm^3 (*i.e.* voids in the interlamellar space). Note that these regions are significantly expanded in the 7:3 mixture compared to 1:9 mixture. Adapted from Ref. [104]. (For interpretation of the references to colour in this figure legend, the reader is referred to the web version of this article.)

with $\Delta n = 2$ revealed the presence of three distinct types of β domains within these mixtures, see Fig. 10d [151]. Each of the two mixed TAG species formed pure β domains, in addition to a distinct type of mixed domains comprising both TAGs. Notably, the *d*-spacing of the mixed β domains remained unaffected by changes in the sample composition. However, the proportion of the three domain types varied in response to shifts in mixture composition, see Fig. 12a.

These domain types were consistently observed in various binary TAG mixtures that contained TAGs with chain length varied from 8 to 16C-atoms. In each case, mixed β domains and β domains originating from the dominant TAG species in the mixture were present. However, when one of the TAG species constituted less than *ca.* 15 wt% of the mixture, its distinct pure domains might not be present, see Fig. 12a [151].

The analysis of the interlamellar spacings within the binary mixed β phases revealed that these spacings are intermediate between those corresponding to the pure components used to prepare the mixture, see Fig. 12b. Additionally, using the average number of C-atoms in the FA residues, $\bar{n}$, it is possible to establish a linear relationship between all distinct interlamellar spacings for β phases. This relationship is applicable for both pure TAGs and binary mixed TAG domains with even-numbered FA acyl chains [151]:

$$d_\beta \approx 0.222\bar{n} + 0.4682 \text{ nm} \quad (16)$$

As an illustrative example, the average number of C-atoms for LLL–MMM mixture is 13.

In the equimolar binary TAG systems studied, the onset of melting for the most stable β polymorphs occurred as the bulk melting temperature

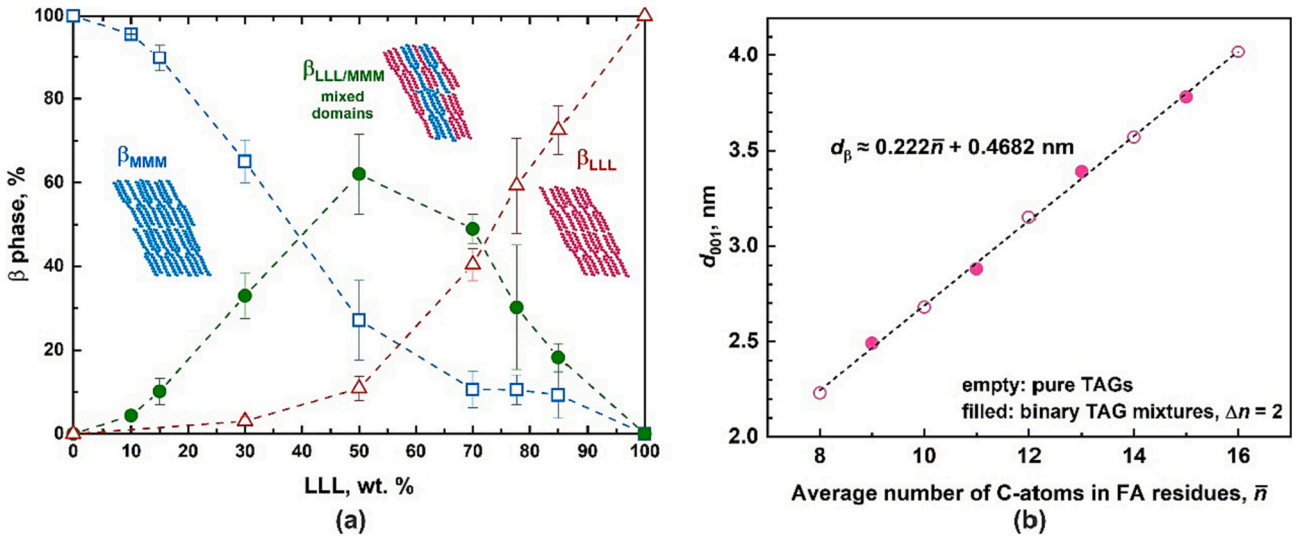

Fig. 12. β phases in binary TAG mixtures. (a) Distribution of different β phase types identified in binary LLL-MMM mixtures with varying compositions: β_{MMM} – blue empty squares; β_{LLL} – red empty triangles; mixed $\beta_{LLL/MMM}$ – filled green circles. Adapted from Ref. [151]. (b) Lattice spacing for β phases formed by pure TAGs (empty symbols) or their binary mixtures (filled symbols). Data exhibits a universal linear relationship. Data from Ref. [151].

of the β phase of the shorter TAG component within the mixture was approached. Interestingly, above this temperature, the SAXS peak corresponding to the β phase of the longer TAG in the mixture persisted and even displayed a slight increase in its area. This observation indicates that, at least in part, the longer TAG molecules included in the mixed domains retained their crystalline state above the melting temperature of the shorter TAG. These longer molecules aligned alongside the chemically equivalent domain types, see Fig. 10e. The complete melting of the sample occurred at slightly higher temperatures, close to those required for the melting of the pure longer chain length TAG present in the mixture [151].

4.3. *Mixing in ternary and more complex triglyceride systems*

The available experimental data on the polymorphic phase behavior of ternary or more complex TAG mixtures remains scarce, despite some recent development in this area.

Pellegrino et al. [116] recently reported a 3D ternary phase diagram for a mixture composed of PPP, SSS, and OOO triglycerides, see Fig. 13. This particular system was selected because the acyl chains present in these TAGs are major constituents of some naturally occurring fats like cocoa butter and lard. The authors reported the following key observations for this ternary system [116]: At low OOO concentrations (0.001 to 0.005 wt%), the phase behavior of the PPP–SSS system remained unaffected by the presence of OOO. With the increase of OOO content (0.007 to 0.2 wt%), the PPP-SSS blend was unable to accommodate all liquid OOO molecules, resulting in a system rearrangement towards a solid solution containing the two saturated TAGs, alongside the liquid OOO. At higher OOO concentrations, the system behaved as a dispersion of mixed PPP–SSS crystals in a liquid OOO medium.

In another study, a range of mixtures containing 3 to 6 distinct monoacid TAGs were examined [151]. These mixtures were designed to mimic the overall FA composition found in CNO. Starting with the predominant components present in CNO (LLL and MMM), the complexity of the investigated mixtures was systematically increased. However, despite achieving the same total FA composition in the most complex six-component TAG mixture as that of CNO, the arrangement of the acyl chains, observed polymorphic phases, and their respective melting temperatures were different from those of the CNO which contains TAG molecules with different acyl groups attached to a single glycerol (mixed acid chain TAGs).

In CNO, approximately 80% of all molecules possess mixed acid chains, whereas the analyzed model mixtures exclusively consisted of TAG molecules with monoacid chains. The structural analysis showed that the average lamellar spacing in the most complex six-component monoacid mixture was comparable to that in the natural CNO. However, due to the preference of the monoacid molecules to pack with molecules of similar structures, the synthetic mixture exhibited complex phase behavior including over 5 distinct domain types upon cooling from the molten state. Moreover, the final melting temperature at which all molecules underwent solid-to-liquid phase transition, remained considerably higher compared to the value measured for CNO (55 °C *vs.* 28 °C) [151].

The performed model experiments showed that the main conclusions made for the binary TAG mixtures remain valid for the significantly more complex systems of monoacid TAGs [151]. Specifically:

- Upon cooling, at a specific temperature T, only the TAGs which has higher melting points ($T_m > T$) may crystallize, while the other TAG species remain in a liquid state.
- Crystallization in monoacid TAG mixtures always starts from the longest TAG species.
- TAGs co-crystallize with the most similar molecules, provided there is a sufficient time for molecular rearrangement.
- Complex mixtures typically yield a combination of co-existing α/β' and/or β-type domains. The quantity and polymorphic structure of these domains depends primarily on the number of TAG components within the mixture and the applied cooling protocol.
- The number of different domain types present in the most stable β phase of a TAG mixture with k mixed TAG species in the mixture is $(2k-1)$: k single-component β phases for each TAG species and $(k-1)$ binary mixed β phases comprised of neighboring chain length molecules.
- The structure of the β phases does not depend on the thermal history of the sample (which is not true for the α and β' phases).
- Melting of TAG mixtures starts from the shortest molecular species with the lowest melting temperature. Consequently, mixtures containing TAGs with notably different melting points exhibit a wide temperature range wherein frozen domains coexist with melted TAGs.

Fig. 14 presents illustrative experimental results that support these conclusions. In particular, the coexistence of liquid and solid domains, along with the initial crystallization of the longest TAG species present

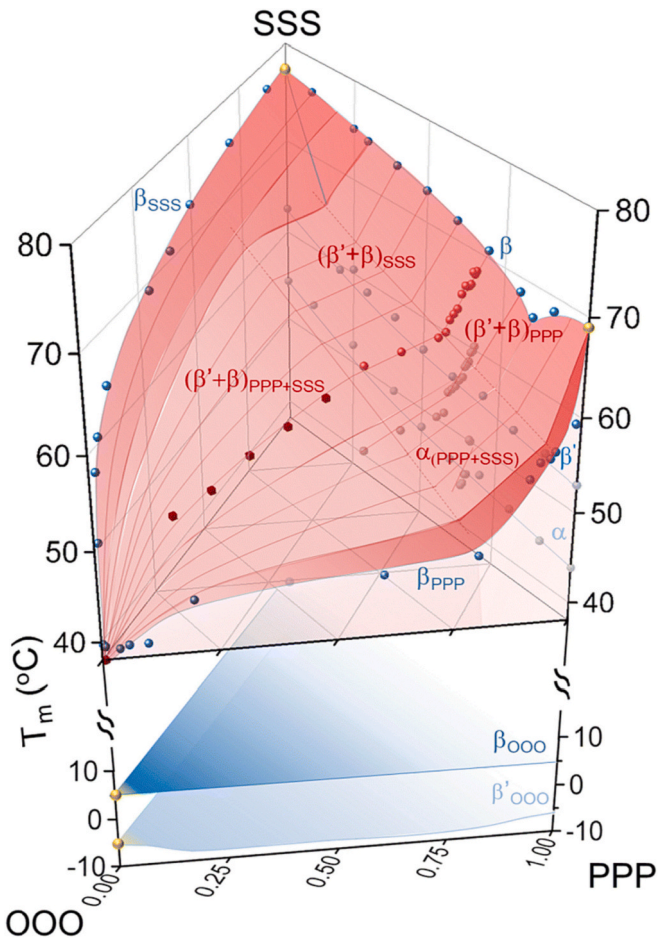

Fig. 13. 3D phase diagram for ternary PPP-SSS-OOO TAG mixture. Binary mixtures are shown with blue circles, whereas the investigated ternary systems are shown with red circles. The upper phase space (shown in red) identifies the higher melting β-form of the ternary blends. The surface beneath it shows the ternary phase transitions for $(\beta' + \beta)_{PPP}$ and $\alpha_{PPP/SSS}$ alongside the binary PPP-SSS phase transitions for β' and α polymorphs. The lower phase space reports the phase behavior and thermal transition for the α- and β-forms of OOO. The figure and its description are reproduced from Ref. [116]. (For interpretation of the references to colour in this figure legend, the reader is referred to the web version of this article.)

in the mixture, is shown in Fig. 14a. This figure presents experimental results from a step-wise cooling experiment involving a four-component TAG mixture (CCC:LLL:MMM:PPP = 15:50:20:15). The SAXS signal reveals that upon cooling to 35 °C and maintaining the sample at this temperature, a single scattering peak emerges around 10 min after equilibrium is achieved. The intensity of this peak initially increases and then stabilizes. Further cooling is required to initiate additional crystallization, as evidenced by the green curves at 27 °C. At this lower temperature, a second peak emerges at a slightly higher scattering vector position, indicating the formation of domains with shorter interlamellar spacing. The sample must be cooled even further to allow the crystallization of the shortest TAG species in the mixture (CCC). This process is clearly observed through the formation of a separate peak at even higher scattering vector position at temperature ≤ 10 °C. It is worth noting that while the primary reflection reveals the formation of a broad peak with three main maxima, the tertiary SAXS peak shows the presence of at least five distinct domain types. More details about the phase behavior of this and other TAG mixtures can be found in Ref. [151].

Fig. 14b displays a scattering curve illustrating the β phases formed within CCC:LLL:MMM:PPP = 15:50:20:15 TAG mixture. According to the general rule, in this four-component mixture, the formation of seven distinct types of domains is anticipated, (7 = 2 × 4–1). This is indeed validated by the experimental observations, as demonstrated by the peak deconvolution analysis in Fig. 14c. These phases include the four pure β phases: β_{CCC}, β_{LLL}, β_{MMM}, and β_{PPP}, alongside three binary mixed phases: $\beta_{CCC/LLL}$, $\beta_{LLL/MMM}$ and $\beta_{MMM/PPP}$. Note that the quantitative analysis of the molecule species distribution based on peak areas suggests the possibility that some mixed β phases may contain a certain percentage of even shorter TAG species. However, the presence of these shorter species does not impact the overall interlamellar spacing in the mixed domains detected by X-ray scattering experiments [151].

4.4. Kinetic aspects of triglyceride mixtures crystallization

Much like the crystallization process in pure TAGs, the kinetics of crystallization in TAG mixtures is deeply influenced by the applied cooling protocol. In broad terms, α phases tend to form under higher cooling rates, while the more stable β' and β phases are favored at lower cooling rates (< 1–2 °C/min) [142,152].

Study of the isothermal crystallization in PPP-SSS mixtures showed that the β phase required the largest supercooling (about 9–13 °C below its melting point) for initiation of crystallization [134]. In contrast, significantly smaller supercoolings were sufficient for crystallization into the β' phase (3.5–8.5 °C) or α phase (< 1 °C). The crystallization kinetics of α phase was the fastest, followed by the β phase. It was argued that the faster crystal growth rate observed in the β phase compared to β' is mainly due to the larger supercooling required for the initiation of crystallization. When accounting for this difference, no significant variations in the crystallization rates were observed upon variation of the mixture composition for samples containing at least 40 wt% SSS. However, the driving force argument was unable to explain the crystallization rate observed on the other side of the eutectic (prevailing PPP). It was shown that the addition of small amounts of SSS to the PPP samples significantly decreased the crystal growth rate. This effect was explained with potential higher mass transfer resistance in mixed samples compared to the pure PPP samples [134].

Furthermore, the isothermal crystallization experiments showed that the mixtures with intermediate compositions required longer induction times for beginning of the crystallization, compared to samples where one component dominated or in pure samples. This observation was explained with the presence of higher activation free energies for crystallization in the mixed formulations as opposed to the boundary cases, see Fig. 15. The apparent induction time for crystallization decreased with decreasing temperature, aligned with the reduction in the nucleation energy barrier under these conditions [134].

4.5. Triglyceride mixing with other chemical compounds (alkanes, fatty acids, surfactants)

A limited information regarding the phase behavior of TAG mixtures with other chemical compounds can be found in Refs. [138, 157–160].

The mixing behavior of MMM, PPP and SSS with *n*-henetriacontane (C_{31}) was studied in Ref. [159]. These mixtures were found to exhibit eutectic behavior. Below the melting temperature of the mixture, alkane and TAG molecules underwent phase separation, resulting in the formation of alkane-rich crystals coexisting with TAG-rich crystals. The position of the eutectic composition depended on the chain length of the FA residues in the TAG molecule. The molar fraction of the alkane in the eutectic composition was approximately $\chi_{C31} \approx 0.2$ for C_{31}-MMM; $\chi_{C31} \approx 0.4$ for C_{31}-PPP, and $\chi_{C31} \approx 0.75$ for C_{31}-SSS mixtures. A decrease in crystalline size was observed for PPP and SSS mixtures with C_{31}, attributed to the potential inhibition of crystal growth caused by the adsorption of C_{31} molecules on the surface of the growing crystals [159]. However, the constructed phase diagrams were relatively coarse, and the polymorphic phase transitions were not examined in detail.

Other studies investigated the solid-liquid phase equilibria within mixed systems of TAGs and fatty acid [138,160]. Formation of eutectic

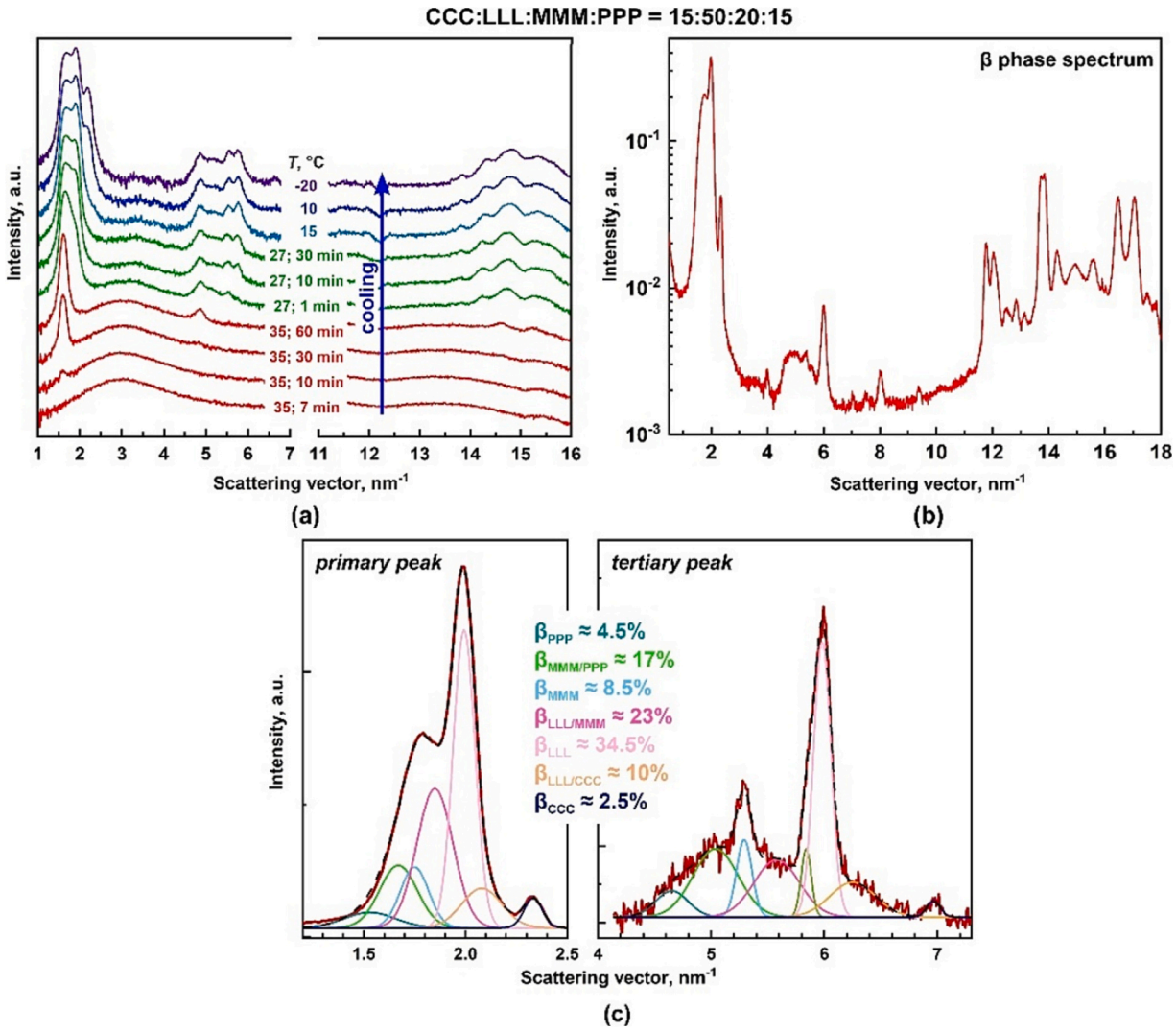

Fig. 14. Polymorphism in CCC:LLL:MMM:PPP = 15:50:20:15 TAG mixture. (a) SAXS/WAXS curves obtained upon 1.5 °C/min cooling from 70 °C and isothermal storage at 35 °C for 1 h, then subsequent cooling to 27 °C and storage for another 30 min and finally cooling to −20 °C. (b) SAXS/WAXS spectrum of the β phase. (c) Peak deconvolution analysis for the spectrum shown in (b). The red thick curves show the original signal obtained from the SAXS measurements. The other colored peaks show different phases as denoted on the figures and the black dashed curves show the cumulative fits. Adapted from Ref. [151]. See the main text for more detailed interpretation. (For interpretation of the references to colour in this figure legend, the reader is referred to the web version of this article.)

point was observed for SSS-palmitic acid, whereas a solid solution forming phase at least close to the pure SSS boundary was suggested for the SSS mixture with unsaturated linoleic acid. Further investigations will be needed to gain a deeper understanding of the molecular arrangement within such TAG and fatty acid mixtures.

The available information about the TAG mixtures crystallization in the presence of added surfactants is also quite limited. In a recent study we demonstrated that the phase behavior of surfactant-TAG mixtures is strongly influenced by the molecular characteristics of the surfactant [157]. For example, *co*-crystallization between a six-component TAG mixture (with total FA composition mimicking the one in natural CNO) was observed with polyoxyethylene (2) oleyl ether surfactant ($C_{18:1}EO_2$). This surfactant did not affect the inner molecular structure of the TAG domains and even contributed to the overall melting enthalpy of the mixture.

In contrast, when investigating another surfactant with oleic tail (monoolein, $C_{18:1}$MAG) in combination with the same TAG mixture, a phase separation occurred after the formation of the most stable β polymorph. Monoolein molecules phase separated into a distinct phase with a characteristic melting temperature specific for the pure surfactant. The characteristic interlamellar spacing in the TAG structure remained unaffected by the presence of monoolein. The melting enthalpy of the mixed TAG-monoolein system, however, corresponded to the one for TAG molecules alone without any increase due to the melting or pure monoolein domains. This result shows that the surfactant molecules in fact influenced the TAG molecules structure, disturbing partially their order and decreasing to some extent the related melting enthalpy [157].

Experiments were performed also in the presence of 10 wt% MAGs with saturated hydrophobic chains. Similarly to the case of unsaturated monoolein, these samples exhibited phase separation. The MAG crystals melted independently when their melting temperature was reached. In some cases, this melting temperature was higher than the melting temperature of the studied TAG mixture [157].

4.6. *Triglyceride crystal network formation*

The natural TAG fats and oils, being complex heterogeneous mixtures of mixed-acid TAGs, usually exhibit a complex phase behavior at room temperature, due to the simultaneous co-existence of liquid and solid fractions. The structural organization of these mixtures has attracted significant attention, as it determines their macroscopic

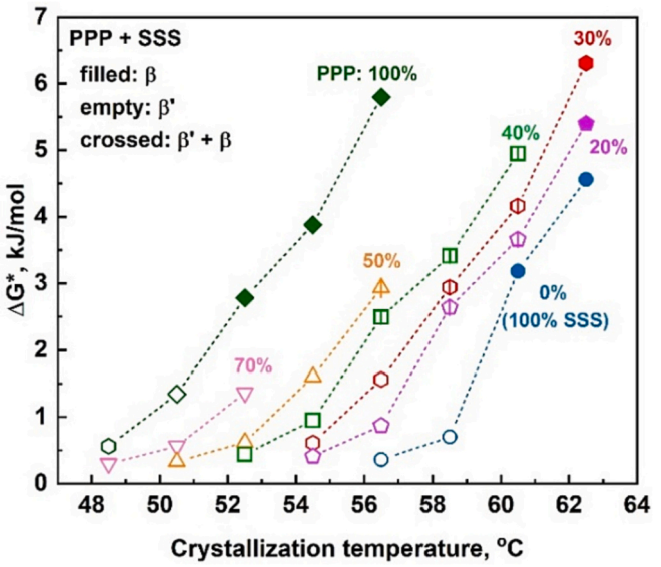

Fig. 15. Activation free energy of nucleation (ΔG*) as a function of crystallization temperature for PPP-SSS mixtures with varying compositions. Different symbols show different compositions of the PPP:SSS mixture: dark green rhombus, 100:0; reversed pink triangles, 70:30; orange triangles, 50:50; green squares, 40:60; red hexagons, 30:70; purple pentagons, 20:80; blue circles, 0:100. Filled symbols indicate the type of polymorphic phase which is observed to form under the investigated conditions: filled symbols – β; empty symbols – β'; crossed symbols – β' + β. The experiments are performed by cooling the molten sample down to the given temperature and allowing it to crystallize under isothermal conditions. Data is from Ref. [134]. (For interpretation of the references to colour in this figure legend, the reader is referred to the web version of this article.)

functionality (*e.g.* their rheological and optical properties). Two main approaches have been used to describe the nanoscale structure of these mixtures. The initial attempts considered them as classical polycrystalline materials, containing chains of linear arrays of solid particles entrapping the liquid oil in between them [161,162]. The particles within the chains were considered to interact through van der Waals forces. Later studies showed, however, that this model is unable to predict the measured non-linear dependence of the elastic modulus (E) on the volume fraction of solid fats, in the rage of *ca.* $\Phi \approx 20$–30% [163,164].

Nearly 40 years later, another idea emerged – to describe the fats with high solid content as fractal colloidal oleogels of polycrystalline particles [164–166]. In this approach, the individual crystallites are considered to arrange in crystal stacks, which in turn aggregate to form clusters. After further aggregation among the clusters, crystalline flocs are formed which serve as building blocks for the formation of fractal crystalline network, see Fig. 16 [164,165,167]. Using this idea, Marangoni and co-authors developed a mechanical model which accurately predicts the yield stress and the elastic modulus of the fats using the relations:

$$\sigma^* \sim \frac{6\gamma}{a_d}\Phi^{1/(A-D)};\ E = \frac{\sigma^*}{\varepsilon^*} \approx \frac{6\gamma}{a_d\varepsilon^*}\Phi^{1/(A-D)}, \tag{17-18}$$

where σ^* is yield stress, ε^* is critical strain beyond which the material begins to flow, γ is solid-liquid interfacial tension (≈ 4–10 mN/m for TAGs [107,171]), a_d is primary particle diameter, Φ is volume fraction of the solids, A is Euclidean dimension of the embedding space, and D is fractal dimension of the particle arrangement in the flocs [168–170]. Assuming a weak-link rheological regime, the fractal dimension of a fat crystal network D can be determined from the slope of log-log plot of yield stress *vs* volume fraction of the solids as [170]:

$$D = 3 - \left(\frac{d(log\sigma^*)}{d(log\Phi)}\right)^{-1} \tag{19}$$

Note that, by definition, the (mass) fractal dimension relates the mass of an object, M, to its size, R, *i.e.* $M \sim R^D$ [172]. For Euclidean objects $D = 1$ for rods, $D = 2$ for disks, and $D = 3$ for spheres, whereas for fractal objects D could be intermediate. The surface fractal dimension, D_S, represents quantitative measure of roughness and it is used for objects whose surface, S, is proportional to their size: $S \sim R^{Ds}$. $D_S = 2$ for smooth objects and vary between 2 and 3 for fractal objects [172].

Although the developed model [170] gave accurate prediction about the mechanical properties of the crystalline fat networks, the question about the structural units constituting this network remained open until 2010 when Acevedo and Marangoni directly visualized the TAG crystal network nanostructure using cryogenic transmission electron microscopy (cryo-TEM) [173,174]. The authors prepared mixtures of fully hydrogenated canola oil (FHCO, which contains TAGs with ≈ 88% stearic FA residues) and high oleic sunflower oil (HOSO, main FA is oleic) and cooled them so that FHCO froze, while HOSO remained in a liquid state. Afterwards, HOSO was extracted from the crystalline network using cold isobutanol and the network was mechanically disrupted to allow direct observation of the single nanocrystal units, see Fig. 17 [173].

These observations revealed highly anisotropic platelet-like crystallites with average length varying between *ca.* 150 and 350 nm, depending on the FHCO/HOSO ratio, average width between *ca.* 50 and

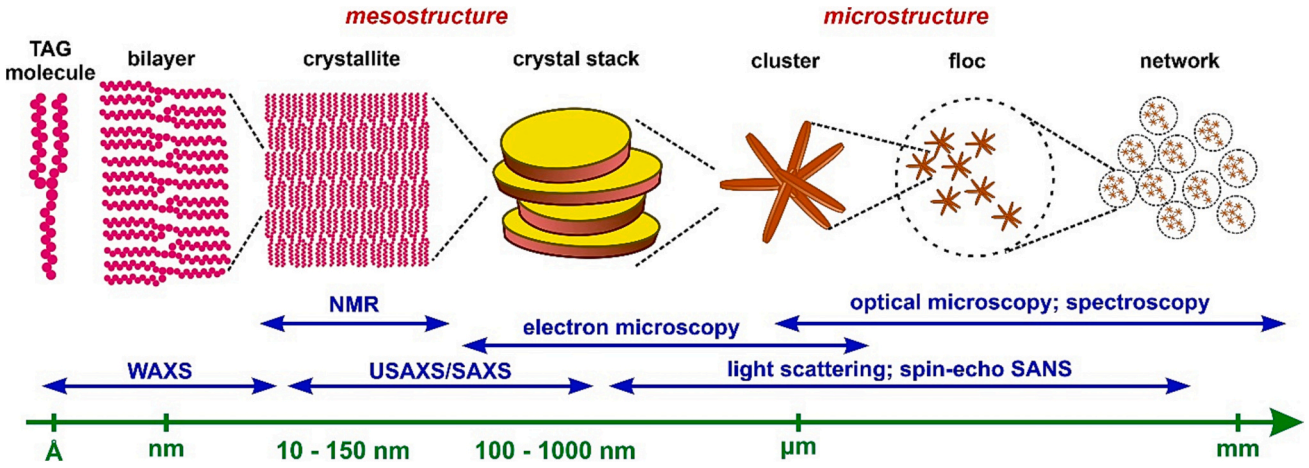

Fig. 16. Schematic presentation of the hierarchical structure of crystalline fat systems at different length scales. The main experimental methods which are used to study the meso- and micro-structure of these materials are also shown. Adapted from Ref. [167].

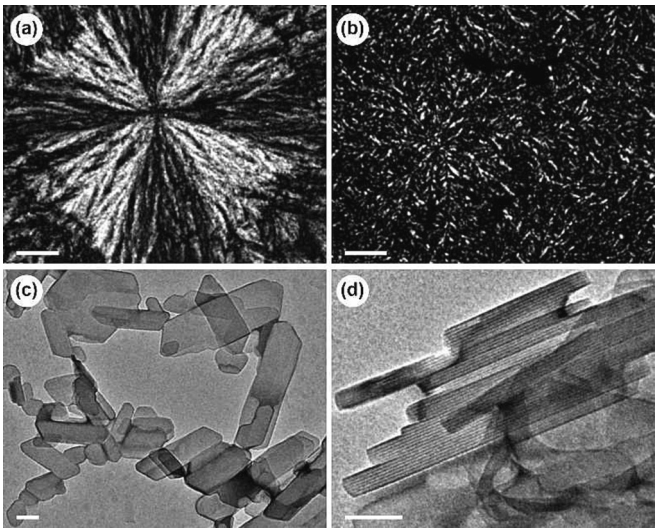

Fig. 17. Microscopy images of TAG crystals. (a,b) Polarized optical microscopy of: (a) 100% FHCO and (b) 50% FHCO +50% HOSO. The addition of HOSO lead to reduction of spherulite size and a decrease in network density. Scale bars: 50 μm. (c,d) Cryo-TEM pictures of individual nanocrystals extracted from such samples. The crystals have platelet shape. The individual TAG layers are visualized when the side view of the platelets is observed as shown in (d). Scale bars: 100 nm. The images are adapted and reprinted with permission from Ref. [173] Copyright © 2010, American Chemical Society.

150 nm, and thickness of 30–50 nm [173]. Note that similar platelets are observed in cooled TAG dispersions as discussed in Section 6.3 below. However, the preparation procedure of the platelets shown in Fig. 17 and in Fig. 25 below are very different – the platelets in Fig. 17 are extracted from TAG crystalline network in absence of any surfactant/aqueous phase, whereas the platelets shown in Fig. 25 are obtained starting from emulsified TAGs.

Similar domain dimensions were obtained when these bulk TAG samples were analyzed with SAXS and the obtained spectra were examined using Scherrer's equation:

$$\xi = \frac{K\lambda}{FWHMcos\theta}, \tag{20}$$

where ξ is the crystalline domain size, K is the shape factor (usually for crystals of unknown shape $K = 0.9$ is used), λ is the X-ray wavelength, FWHM is the Full Width at Half of the Maximum peak height expressed in radians, and θ is the diffraction angle at which the peak is observed [173,175]. While the Scherrer formula gives information for the average crystallite thickness only, it has been shown that additional information about the TAG thicknesses distribution can be obtained from SAXS spectra when the Bertaut-Warren-Averbach method is applied [176]. This method is based on Fourier analysis of the obtained peak shapes.

The results from cryo-TEM and SAXS experiments were in an excellent agreement with each other and demonstrated directly the effect of the cooling rate over the obtained crystallite sizes. For example, the volume weighted mean thickness of PPP crystals were 54 and 86 nm for quickly and slowly cooled samples, respectively, see Fig. 1 in Ref. [176]. Furthermore, the effect of shearing conditions during the crystallization over the final crystallite sizes was also demonstrated in these studies, see Ref. [174]. Analysis of spin-diffusion NMR experimental results showed that the TAG thicknesses distribution can be also obtained using this technique [167].

Additional information about the structure of TAG crystalline networks was obtained from USAXS experiments, related computer simulations and modeling of crystalline nanoplatelets aggregation [164,177–180]. The USAXS technique measures the morphology on length scales between *ca.* 1 nm and 2–5 μm [164,181]. A non-linear regression analysis should be made of the obtained scattering signal, $I(q)$, to extract information about the characteristic sizes of the scattering entities, as well as information about their surface characteristics, see Fig. 18. It was shown that the crystalline TAG structure can be modeled successfully using Guinier-Porod and Unified Fit models with maximum of three slopes and two radii of gyration [164,180]. The Unified Fit equation in which the scattering objects are approximated as spheres is written as [180]:

$$I(q) = Gexp\left(-\frac{q^2R_{gi}^2}{3}\right) + \frac{B}{q^P}exp\left(-\frac{q^2R_{gi-1}^2}{3}\right)\left[erf\left(-\frac{qR_{gi}}{\sqrt{6}}\right)\right]^{3P}. \tag{21}$$

In this equation, the first term describes the Guinier region which is valid for $q \leq q_1$, whereas the second term represents the Porod power law region, valid for $q \geq q$ [180]. G and B are constants which are related to the volume of the scatterers and to their specific surface area, respectively. R_g is the radius of gyration of the scattering objects: for the smallest length scale, $2 \times 10^{-3} < q < 2 \times 10^{-2}$ Å^{-1}, the average size of the crystalline nanoplatelets (R_{g1}) can be obtained, whereas the average size of the larger aggregates is estimated from the analysis of the scattering signal obtained at smaller scattering vectors (larger length scale), $4 \times 10^{-4} < q < 2 \times 10^{-3}$ Å^{-1} [179].

The slopes of the curve, characterized by Porod exponent, P, measures the internal structure of the entities/aggregates and can be related to the fractal dimensions of the scattering structure:

$$|P| = -2D + D_S, \tag{22}$$

where D is the fractal dimension and D_S is the surface fractal dimension [172]. The value of $|P|$ ranges from *ca.* 1 to 4 and, in general, the smaller the value of $|P|$ is, more open the structure is [172]. Thus $|P| = 1$ shows rod-like structure, $|P| \approx 2$ suggests presence of cluster of particles, whereas $|P| = 4$ implies uniformly dense objects with a smooth surface [181]. The values of D and D_S, depending on the value of Porod exponent, are summarized in Table 4. Further detailed information about the mathematical modeling of the crystalline fat networks is available in the original papers [177–180].

The analysis of the crystalline networks formed in various mixed TAG systems showed that the slope at highest scattering vectors in the USAXS region, $2 \times 10^{-3} \lesssim q \lesssim 3 \times 10^{-2}$ Å^{-1}, was caused by 2-dimensional objects with either smooth, rough or diffuse surfaces, $|P| \approx 4$. TAG nanoplatelets having smooth surfaces were suggested when $|P| = 4$, TAG nanoplatelets with rough surfaces are observed when $|P| \approx 3.7$–3.9, and TAG nanoplatelets coated with liquid oil were proposed when $|P| \approx 4.1$–4.3 [179,180,182]. The average radius of gyration for these nanoplatelets was found to be between 20 and 150 nm [179].

At intermediate q values, $4 \times 10^{-4} \lesssim q \lesssim 2 \times 10^{-2}$ Å^{-1}, the slope was found to vary between ca. -1 and − 2 [179,180,182]. Slope of $|P| = 1$ was interpreted as caused by the presence of 1-dimensional objects which were termed "TAGwoods", i.e. long cylindrical aggregates formed from the individual crystalline nanoplatelets, see the schematics in Fig. 18. The formation of TAGwoods was found to be especially pronounced in samples crystallized at higher cooling rates [182]. The intermediate slopes ($|P| \approx 1.5$) were interpreted as indicating the presence of mixture of non-aggregated crystalline nanoplatelets and deformed TAGwoods or the formation of incomplete TAGwood aggregates, whereas slope of $|P| \approx 2$ showed the formation of clusters [179].

The slope at the smallest scattering vectors showed that the aggregates of TAGwoords can be evenly distributed in space ($|P| = 3$) when the platelets have clean surfaces and the system is allowed to relax sufficiently long. Otherwise, usually slopes between −3.5 and − 4.5 were observed showing aggregates with rough or diffuse surfaces, respectively [179].

The effects of cooling rate, crystallization temperature, shearing conditions and emulsifier addition over the properties of TAG crystalline networks were also studied. The observed results were in a good agreement with the trends discussed in Sections 3.3, 4.2 and 4.4 above.

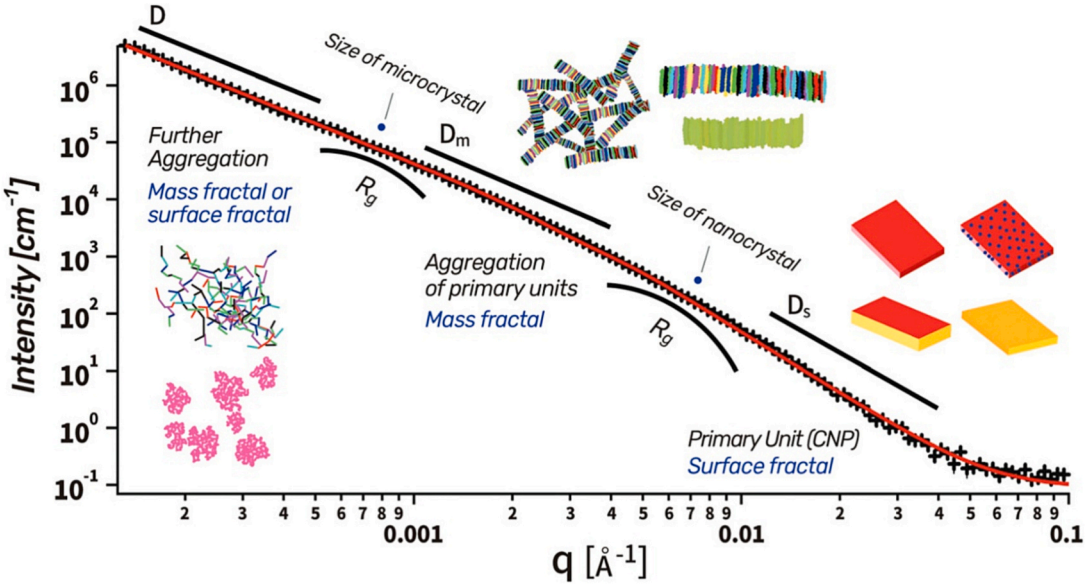

Fig. 18. Schematic representation of USAXS spectra of a model edible fat. Three structural levels at different length scales are shown, characterized by the extracted radii of gyration (R_g, from the bends in the curves) and slopes which can be related to the surface fractal dimension of the structure (D_s) or the mass fractal dimension (D_m) for aggregates of the particular structure. United-fit model has been used for data description. The figure is reprinted with permission from Ref. [164]. Copyright © 2020, The Royal Society of Chemistry.

Table 4
Mass and surface fractal dimensions for different values of Porod exponent and their physical interpretation.

Porod exponent, P	Mass fractal dimension, D	Surface fractal dimension, D_S	Interpretation
$\|P\| = 1$	$D = 1$	$D_S = 3$	Rod-like structures
$1 \leq \|P\| < 3$	$D = \|P\|$	$D_S = 3\|P\|$	$\|P\| \approx 2$ – cluster of particles
$3 \leq \|P\| < 4$	$D = 3$	$D_S = 6 - \|P\|$	Rough surface; uniform distribution in space
$\|P\| = 4$		$D_S = 2$	Smooth surface
$\|P\| > 4$	–		Larger aggregates with diffuse surface/ nanoplatelets coated with oil

Further detailed information can be found in Ref. [180] and the cited original papers therein.

5. Polymorphism at triglyceride-air and triglyceride-water interfaces

The following section provides a concise overview of the phase behavior of TAG molecules situated at the oil-water and oil-air interfaces. Despite the (somewhat) limited information available on this subject, we have included several intriguing results. The studies of these model systems help researchers to understand the properties of the real interfaces encountered in diverse applied areas, including the cleaning of soiled substrates, stabilization of disperse systems, wetting of TAG systems, and others.

5.1. Phase behavior of triglycerides' Langmuir-Blodgett monolayers

The phase behavior of Langmuir-Blodgett monolayers with pure or mixed TAG systems has been the subject of several studies [46,183–185]. These studies revealed that the transition from "gas" to "condensed film" phase for 2D (two dimensional) TAG monolayers spread over an air-water interface occurs when the area per molecule reaches approximately 63 ± 2 Å^2, a significant change from the initial 110Å^2 area employed in the beginning of the experiment. The surface pressure at the transition is $\pi \approx 8$–10 mN/m.

Similar results were obtained for all studied pure TAGs (C_{16}TAG, C_{18}TAG and C_{20}TAG, known also as triarachidin, AAA), as well as for three distinct binary mixtures formed by these TAGs. The critical surface pressure at which the monolayer collapsed to a multilayer structure ranged between approximately 40 and 48 mN/m. There was a slight decrease in this critical surface pressure with the increase of FA chain length, *i.e.* $\pi(C_{20}TAG) < \pi(C_{18}TAG) < \pi(C_{16}TAG)$.

At the air-water interface, the molecules adopted a trident conformation, with all alkyl chains oriented towards the air, while the glycerol group remains in contact with the water phase. The estimated monolayer thickness was determined to be 1.49 nm for PPP [184], 1.75 nm for SSS, and 2.19 nm for AAA molecules, corresponding to tilt angles of 46°, 49° and 59°, respectively [185]. Formation of multilayer crystals was observed upon increased surface pressures, see the schematics shown in Fig. 19.

Atomic force microscopy (AFM) studies of Langmuir-Blodgett monolayers, deposited on mica upon a forced compression of 20 mN/m, revealed that incomplete phase separation took place in PPP-SSS monolayers, while complete separation was observed for PPP-AAA. Interestingly, for SSS-AAA monolayers, no separation was observed and the mixed monolayer exhibited nearly complete mixing [184].

5.2. SSS arrangement at oil-water interface studied by atomistic MD simulations

Atomistic molecular dynamic simulations were performed with two layers of SSS molecules enclosed between aqueous phases, both in the presence and absence of water-soluble surfactant [186]. The results of these simulations, carried out at temperatures of 300 K and 350 K, revealed that tristearin molecules adopted a trident conformation, with the glycerol head groups pointing towards the aqueous interface. This conformation exhibited three primary variations, depending on the $\angle T_1T_2T_3$ angle, where T_a represents the position of the *sn-a* acyl chain with respect to the *xy* plane.

Approximately 44% of the molecules studied, adopted a tripod-type structure ($\angle T_1T_2T_3 \approx 60°$), around 19% assumed a linear structure ($\angle T_1T_2T_3 \approx 180°$), 27% were in a kinked orientation ($\angle T_1T_2T_3 \approx 120°$), and the remaining 10% appeared as "defects" in the ordered structure. The acyl chains of SSS molecules were hexagonally packed, with a lattice

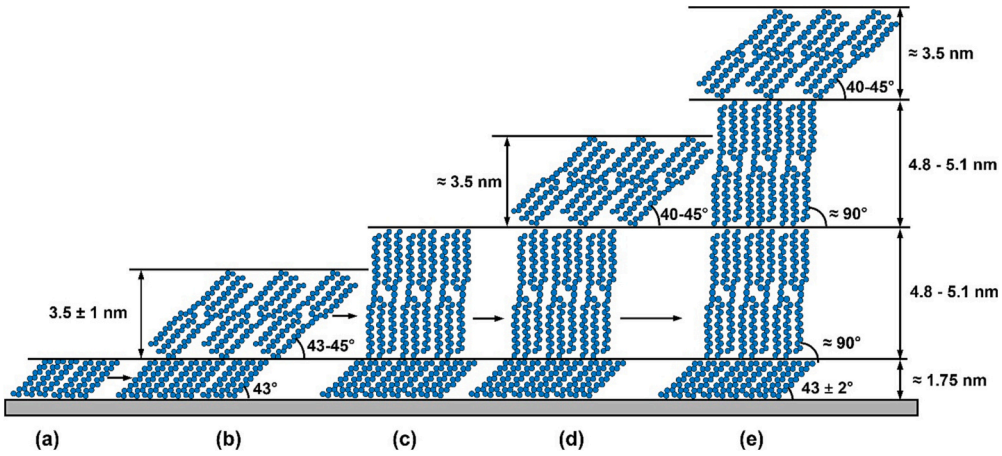

Fig. 19. Schematic representation of the structures formed by thin SSS layers in contact with water. (a) Monolayer structure comprising of SSS molecules in trident conformation. The TAG acyl chains are proposed to be tilted at ≈ 43° with respect to the interface. This structure is formed at surface pressure $\pi \leq 5$ mN/m, and also around the thicker domains formed at $\pi \geq 10$ mN/m. (b) Stable thin crystals formed at $\pi \approx 10$ mN/m. (c) Metastable crystal. Such structure is formed when the film is compressed to $\pi \approx 20$ mN/m and then immediately withdrawn. (d,e) Structure of thicker 2D-crystals observed after 30–60 min of isobaric compression at $\pi > 20$ mN/m. Adapted from Ref. [183].

constant ≈ 0.46 nm. The average area per molecule at 300 K was around 0.59 nm^2, slightly below the experimental value (≈ 0.62 ± 0.01 nm^2 [185]) [186]. The glycerol headgroups were typically situated at an approximate distance of 0.8 nm from each other, although a few head groups were even closer, at ≈ 0.6 nm.

The impact of surfactant addition (sodium linear alkylbenzene sulfonate, LAS) on the properties of the SSS bilayer was also investigated by the authors. Interestingly, the spontaneous incorporation of LAS surfactant molecules into the SSS layer, up to a SSS:LAS molecules ratio of 3:1, had minimal effect on the packing order of the TAG molecules. A slight lateral expansion combined with thinning in the transverse direction was observed when the SSS:LAS molecules ratio exceeded 9:1. Nonetheless, the hexagonal arrangement remained intact, albeit with some packing defects around the LAS surfactant tails that were inserted between the SSS acyl chains. The inclusion of surfactant molecules, however, led to a decreased temperature at which the gel-to-liquid phase transition occurred for SSS molecules [186].

In a separate study, coarse-grained MD simulations were employed to investigate SSS ordering at oil-air and oil-water interfaces in the presence of two oil-soluble surfactants: PGPR or monoolein [187]. The results showed that $C_{18:1}$MAG surfactant promoted the ordering of SSS molecules normal to the interface, while the PGPR surfactant reduced the ordering even below the level observed in the absence of surfactant. The authors explained these findings with the similarity in length between the $C_{18:1}$MAG and SSS chains, which enhanced ordering, whereas the branched and bulkier polymeric PGPR surfactant diminished the ordering, thereby limiting the potential for interfacial crystallization [187].

An experimental study comparing the effect of the same two surfactants on the crystallization of canola oil in the presence of hydrogenated canola oil reached similar conclusions [188]. The addition of $C_{18:1}$MAG surfactant to the canola oil + hydrogenated canola oil mixture led to pronounced interfacial crystallization, resulting in an additional Pickering-type stabilization for the prepared water-in-oil emulsions. By contrast, when the same system was studied with PGPR surfactant instead of $C_{18:1}$MAG, direct nucleation of the continuous phase occurred without evidence of interfacial crystallization. An association between $C_{18:1}$MAG and SSS in the liquid state was proposed to explain the observed differences.

5.3. Isolated triglyceride-water interface studied by synchrotron X-ray scattering experiments

A recent and intriguing study, conducted by MacWilliams et al. [43], has showcased the advancement in X-ray scattering techniques. In this study, the researchers investigated the interfacial crystallization of mono- and diacylglycerol emulsifier (MDG, monoacylglycerols content of 56%, total FA composition ≈ 80% stearoyl chains and ≈ 18% palmitoyl chains) dissolved in MCT TAG oil (≈ 57% C_8 and 43% C_{10} FA residues). This investigation was conducted both in the presence and absence of sodium caseinate and whey protein isolate (WPI) proteins. The researchers employed interfacial tension measurements through the drop shape analysis technique, combined with complementary X-ray scattering experiments. Notably, their X-ray experiments directly examined an oil-water interface that was confined within a glass capillary. To realize this experiment, they precisely controlled the position of the X-ray beam and systematically irradiated the entire height of the capillary, see Fig. 20a [43].

The results of the study showed that the addition of proteins to the MCT-MDG mixture led to a reduction in the temperature at which MAGs crystallization occurred at the oil-water interface. A comparison between the crystals formed in a bulk MCT + 0.27 wt% MDG sample and the same oily solution placed in contact with an aqueous phase was performed by SAXS/WAXS measurements. Both samples were stored for 12 h at 4 °C, prior to the measurements. Notably, in the absence of oil-water interface, no crystallization occurred in the bulk TAG. Conversely, the sample containing oil-water interface displayed several intensive peaks. This observation strongly suggested that MDG adsorption at the interface served as a nucleation site, facilitating further crystallization through an interfacial heterogeneous nucleation mechanism. Additionally, two distinct lamellar structures corresponding to β-crystal polymorphs of monostearin (C_{18}MAG) and monopalmitin (C_{16}MAG) were observed with lattice long spacings of 49.7 and 44.5 Å, respectively [43].

The presence of adsorbed protein at the interface did not alter these long spacings or the polymorphic forms [43]. However, the quantity of MDG crystals in the bulk MCT-MDG lipid solution, both in the presence and absence of proteins, was not equivalent. In the absence of proteins, the quantity of crystals was about half of what was found in presence of proteins. This difference was explained by the decreased temperature required for interfacial crystallization in the systems containing proteins. Consequently, the amount of crystals in the system with protein was reduced compared to the system without protein when both were examined at the same temperature [43].

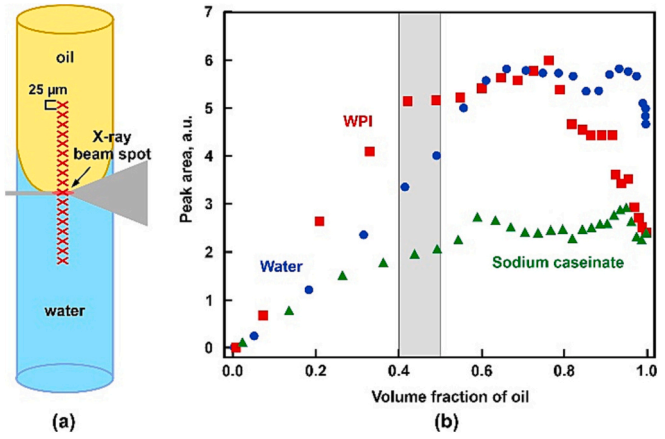

Fig. 20. SAXS study of interfacial MDG crystallization at TAG-water interface. (a) Schematic representation of glass capillary filled with aqueous solution in contact with MCT + MDG solution. A beam spot size of 25 μm (vertical) and 250 μm (horizontal) has been used to monitor the scattered signal at different positions within the samples. (b) Area of the peak observed at $q = 0.127$ Å^{-1} corresponding to monostearin crystals as a function of the beam position within the height of the sample. Different symbols denote the different aqueous solutions investigated: blue circles – water; green triangles – 0.1 wt% sodium caseinate solution; red squares – 0.1 wt% WPI solution. Efficiency of the promotion effect for the interfacial MAG crystallization is: WPI > water > sodium caseinate. Adapted from Ref. [43]. (For interpretation of the references to colour in this figure legend, the reader is referred to the web version of this article.)

An analysis of the peak representing the monostearin crystals as a function of the scanning X-ray position, provided additional insights into the interfacial MAG crystallization within the studied systems, see Fig. 20b. A noticeable increase in the concentration of monostearin crystals was observed in the interface region for the sample containing WPI, indicating a crystal promotion effect. The peak area observed in this case was even larger than the one measured for the bare oil-water interface, suggesting that the mere displacement of WPI from the oil-water interface by MDG could not account entirely for the observed results. Two possible explanations were proposed by the authors for the enhancement of MAG crystallization at the oil-water interface in the presence of WPI protein: (1) The globular nature of WPI adsorbed at the oil-water interface might effectively increase the 'thickness' of the interfacial region. This increase in the thickness could provide additional MDG adsorption sites, leading to an increased MDG content able to crystallize at the interface and/or (2) The crystals hydrophobicity might be decreased due to the protein adsorption over them. This would allow them to protrude more extensively into the aqueous phase [43]. Further investigations are required to determine the precise mechanism promoting the monostearin crystallization at the oil-water interface in the presence of WPI protein.

5.4. *Surface hydrophobicity of triglyceride layers*

The hydrophobicity of thin TAG layers was evaluated by performing three-phase contact angle measurements in Refs. [44, 157, 189]. To perform these experiments, a small quantity of the molted TAG under investigation was placed onto a pre-hydrophobized glass slide. Another pre-hydrophobized glass slide was then positioned on top to create a uniform thin layer of molten TAG. A precise control over the storage conditions of the investigated substrates allowed a comparison between the hydrophobicity of α- and β-forms of TAGs. The results showed that the three-phase contact angle, measured through the aqueous droplet placed over the TAG substrate, was ≈ 110° for deionized water-MMM system for MMM substrate in either α or β phase [44]. This value decreased when the deposited solution contained pre-dissolved surfactant, see Fig. 21a. For example, the angle was ≈ 100° for 0.5 wt% sodium dodecyl sulfate (SDS) solution deposited on α_{MMM} substrate, whereas it decreased further to approximately 60° for SDS-β_{MMM} substrate [44]. Similar values were also reported for nonionic polysorbate 20 surfactant (Tween 20) [157].

The consistent trend of β substrates exhibiting greater hydrophilicity in comparison to the layers in α phase was observed across all studied systems, see Fig. 21b and Ref. [44]. A slight reduction in the disparities between the angles measured with α and β phase substrates was observed when an oil-soluble surfactant was added to the aqueous phase through pre-solubilization within water-soluble surfactant micelles. For example, for 0.5 wt% SDS + 0.5 wt% Brij 30 (polyoxyethylene (4) lauryl ether) system, the measured three-phase contact angles were ≈ 43° for α_{MMM} and ≈ 28° for β_{MMM} substrates [44].

The experiments involving various model TAG mixtures composed of monoacid TAG molecules showed that the measured three-phase contact angles exhibited no significant dependence on the specific composition of the TAG substrate. Similar contact angle values were observed for both the LLL:MMM = 1:1 mixture and a more complex six-component TAG mixture (with a total FA composition equivalent to that found in natural CNO) in the presence of both water-soluble and oil-soluble surfactants added to the aqueous phase. These angles were approximately 40–55° for substrates in β-form [157].

The measured three-phase contact angle for CNO-deionized water system was ≈ 83° at 10 °C, slightly diminishing to ≈ 71° at 20 °C. When water-soluble surfactant solutions were introduced, the three-phase contact angles with CNO decreased to around 45°. Upon further addition of oil-soluble surfactant to the system, these angles decreased even further to 25–30° [189].

We note that in other studies involving TAG layers, the formation of super hydrophobic β surfaces was demonstrated [190–192]. However, these substrates were prepared by depositing a small amount of molten TAG onto a plastic substrate, allowing it to crystallize and undergo a polymorphic phase transition at an open TAG-air interface. This process led to the formation of fractal structures on the TAG surface, due to the fat blooming upon the α to β polymorphic transformation. As a result, the surface area increased significantly, yielding contact angles with water as high as 150–160°. The initial contact angles at smooth TAG-water interfaces were ≈ 110° [190], similar to the findings in Ref. [44].

6. Emulsified triglycerides

Polymorphic phase transitions in emulsified TAGs are studied mostly in the context of preparation of solid lipid nanoparticles (SLN), nanostructured lipid carriers (NLC, blends of liquid and solid lipids) and stabilization of water-in-oil or oil-in-water emulsions for applications in food and cosmetic industries.

SLN are usually produced from oil-in-water emulsions that are prepared by melting the oily phase, emulsifying it, and subsequently cooling it until the dispersed drops solidify. Numerous studies show the potential of SLN for encapsulation of lipophilic bioactive ingredients such as drugs, vitamins, antioxidants, fragrances, flavors, pigments, unsaturated fatty acids and others [54,63,193–198]. The polymorphic transitions influence strongly the stability, rheology and appearance of the final products containing SLNs. Therefore, to achieve quality products with a good long-term stability one should understand and control the polymorphism of the dispersed lipid [199].

The main difference between the crystallization in bulk and in emulsions lies in the amount of crystallizing material in one entity. Just 1 ml of oil contains sufficient material for production of over 10^{12} emulsion droplets with 1 μm diameter or 10^{15} drops with 100 nm size. Consequently, in the absence of other components, a heterogeneous nucleation mechanism in bulk is usually observed due to the inevitable presence of foreign particles, whereas in emulsion drops a homogeneous nucleation usually takes place unless the surfactant adsorption layer serves as a site for heterogeneous nucleation at the drop surface, Section

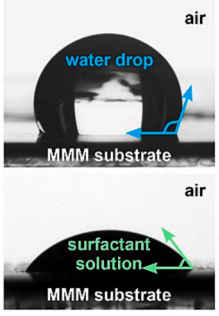

(a)

Aqueous surfactant solution, wt. %	Contact angles for different substrates, °		
	MMM		CNO, 10°C
	α phase	β phase	
deionized water	110 ± 2[a]	109 ± 1[a]	83 ± 1
0.5 SDS	99 ± 4	61 ± 5	
0.5 SDS + 0.5 Brij 30	43 ± 3	28 ± 4	
1.5 Tween 20		68 ± 6	48 ± 1
1.5 Brij S20 + 0.5 Brij30	61 ± 3	56 ± 4	34 ± 1

(b)

Fig. 21. Hydrophobicity of TAG layers. (a) Illustrative pictures showing water droplet placed over MMM substrates in absence (top) and in presence (bottom) of surfactant. Significant difference in the wetting is observed in the two cases. (b) Three phase contact angles measured for aqueous solution drops placed over MMM or CNO substrates. Data from Refs. [44, 157, 189]. Additional data is available in the cited references. [a] Data is for MMM substrate with pre-dissolved 0.5 wt% Brij 30 surfactant. Similar values are reported in Ref. [190] for pure MMM substrates.

6.2 [54]. Moreover, the emulsified systems exhibit a substantial increase in their surface-to-volume ratio, which in turn amplifies the influence of the surface-related effects.

The nucleation mechanism significantly influences the onset crystallization temperature, T_{cr}. Supercooling of >20 °C, compared to the temperature at which the bulk crystallization begins, has been reported for 60–150 nm TAG particles. Specifically, trilaurin particles exhibit a supercooling of about 50 °C, see Fig. 22a [38,200]. However, this comparison does not account for the fact that the drops freeze in the unstable α phase, while the melting occurs from the stable β phase. When supercooling is calculated as the temperature difference between the melting point of the α phase and T_{cr}, a consistent value of ≈ 24 °C is found for trilaurin, trimyristin, tripalmitin, and tristearin, see the empty red stars in Fig. 22b [200]. In contrast, the melting behavior of bulk and emulsified TAGs shows only minor effect of drop size for drop diameters exceeding 100–200 nm. A slight decrease in melting temperature by 3–5 °C compared to the bulk has been observed for smaller particulates [200]. This phenomenon can be quantified using the Gibbs-Thomson equation:

$$ln\frac{T_{m,r}}{T_m} = -\frac{2\gamma_{sl}V_S}{r\Delta H_m}, \quad (23)$$

where $T_{m,r}$ is the melting temperature of particle with size r, T_m is the melting temperature of the bulk material, γ_{sl} is the interfacial tension between liquid and frozen material, V_S is the specific volume of the solid and ΔH_m is the melting enthalpy [201].

A study involving femtoliter surface droplet arrays also demonstrated a significantly decreased crystallization temperature for smaller droplets in contrast to bulk TAG [202]. This study focused on two types of immobilized MMM droplets, with volumes of 2 or 7 femtoliters, deposited onto a silicon wafer surface. These droplets assumed the shape of a spherical cap. Their phase behavior was studied with synchrotron SAXS technique. A notable advantage of this method is its ability to create stable surfactant-free droplets. The results showed a decrease in crystallization temperature from around 36 °C for bulk MMM (observed upon 1 °C/min cooling), to 30 °C for larger volume MMM droplet array, and further to 27 °C for the smaller droplets. The smaller droplets exhibited faster crystallization kinetics, attributed to their lower initial crystallization temperature and their greater surface area-to-volume

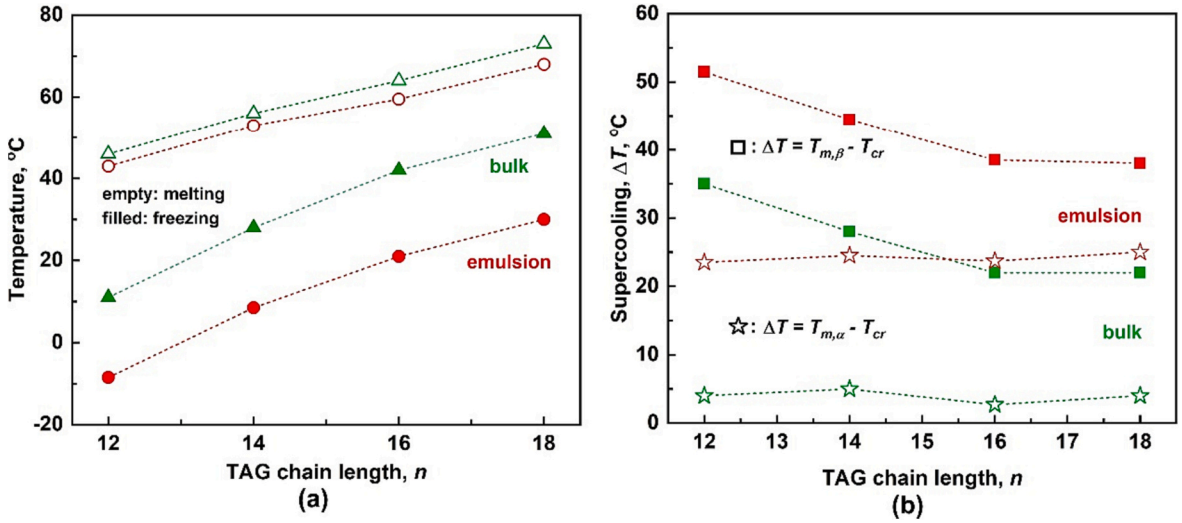

Fig. 22. Comparison between melting and freezing temperatures for bulk and nanoemulsified TAGs of different chain lengths. (a) Melting (empty symbols) and crystallization (filled symbols) temperatures for bulk (green triangles) and nanoemulsified (red circles) TAGs. (b) Comparison between the supercoolings observed in bulk and in emulsions. A chain length dependence is observed when the supercooling is defined as $\Delta T = T_{m,\beta} - T_{cr}$ (squares). However, this chain length dependence disappears when the fact that the freezing occurs into α phase is accounted for by defining $\Delta T = T_{m,\alpha} - T_{cr}$ (stars). The studied emulsions contain TAG droplets with sizes ≈ 100 ± 25 nm. Data is from Ref. [200]. (For interpretation of the references to colour in this figure legend, the reader is referred to the web version of this article.)

ratio. Moreover, these findings suggested that the crystallization process within the droplets occurs *via* a surface nucleation mechanism, with the nucleus originating at the triple boundary between solid, lipid, and water [202]. Note that although these droplets possess a femtoliter volume, their volume is about four orders of magnitude larger compared to the 100 nm surfactant-stabilized droplets studied in Ref. [200], where even lower crystallization temperatures were demonstrated.

6.1. Polymorphic transformations

The available experimental results show that the main phase transition sequence observed in bulk TAGs remains unchanged for emulsified TAGs. However, significant alterations occur in terms of kinetics, particularly when an adsorbed surfactant layer or other additives are introduced within the emulsion drops, see Table 5 [38,41,54,203–208]. Generally, polymorphic phase transitions exhibit accelerated rates within fine particles [38,54]. Additionally, TAGs with shorter chain lengths, especially those containing saturated FA tails, exhibit faster polymorphic transformations compared to TAGs with longer and/or unsaturated tails [54,194,200].

Two main effects are usually invoked to explain the enhanced rate of polymorphic transformations [38]. First, the total Gibbs energy of the emulsified system is higher compared to that of bulk materials due to the excess surface energy contribution. This leads to a reduction of the melting point (Gibbs-Thomson effect, eq. 23). Moreover, the polymorphic transitions may be initiated on the surface by the surfactant adsorption layers or due to the presence of planar defects. Second, the presence of lattice defects, such as dislocations or stacking faults, can trigger the polymorphic transitions. These defects are found in higher concentrations within nanometer sized particles compared to the bulk phases [38,41].

An example highlighting the role of TAG chain length can be found in Ref. [200]. In this study, particles of LLL and MMM with diameters around 100 nm, stabilized by phospholipids/bile salts, were shown to exhibit α → β phase transition within a few minutes of preparation. In contrast, comparable particles prepared with the longer SSS retained a significant amount of the α phase even after several hours of storage [200]. It is important to note that this comparison was made under identical storage temperatures, without considering the temperature difference between the melting point of the respective TAG and the storage temperature. This temperature difference is important as it defines the height of the energy barrier that must be surmounted for a particular phase transition to occur. As shorter TAGs possess lower melting temperatures, the molecules within these particles have to climb over a reduced energy barrier for polymorphic transition. Therefore, the observed difference may not be solely attributed to the chain length difference.

More recent study reported that approximately 86% of SSS microparticles with sizes 50–500 μm, remained in the α phase even after a two-months storage period at 25 °C. Furthermore, nearly all particles retained the α phase when stored at 4 °C [199]. Further dedicated experiments are needed to distinguish between the two effects at play.

Table 5
Summary of the influence of various factors on the rate of polymorphic phase transitions observed in TAG dispersions.

Factor	Promotes the stability/formation of:	Explanation
Cooling rate	α phase (rapid) β phase (slow $\lesssim$ 1–2 °C/min)	Nucleation rate increases with decrease of temperature
Storage temperature	α phase ($T_{st} << T_{m,\alpha}$) β phase ($T_{st} \gtrsim T_{m,\alpha}$)	Depends on the comparison between storage temperature and $T_{m,\alpha}$
Smaller particle size	β phase	Smaller particles – higher surface area, higher number of defects
Surfactant adsorption layer	β phase ($T_{surf,m} < T_m$)	Mainly depends on the comparison between melting temperature of TAGs and surfactant. Typically, unsaturated surfactants – lower melting temperature, ensures the molecular mobility needed for α → β transition; saturated surfactants form solid shells and suppress α → β transition
	α phase ($T_{surf,m} \gtrsim T_m$)	
Additives	β phase	solid additives – provide a seed for heterogeneous nucleation; molecules incorporated into TAG lattice – cause formation of defects in it

6.2. Effect of surfactants/additives

The surfactants stabilizing the nanodroplets/nanoparticles also influence significantly the polymorphic transitions. Two distinct effects have been observed: (1) Stabilization of metastable polymorphs when saturated surfactants are present at the droplet surface and (2) Facilitation of the formation of the most stable phase when surfactants have unsaturated tails or a branched structure, see Table 5. These effects are explained with the melting properties of the surfactant molecules and the related molecular mobility at the oil-water interface [42,187,194,204,207–210].

Saturated surfactants, with hydrophobic tail akin to or longer than the length of the acyl chains of TAG molecules, tend to order and solidify on the drop surface at temperatures resembling lipid crystallization temperature. This leads to the creation of an interfacial crystalline layer that serves as a template for subsequent TAG crystallization near the droplet surface through interfacial heterogeneous mechanism. In contrast, unsaturated surfactant molecules possess significantly lower crystallization temperature, and they remain relatively disordered even during TAG crystallization upon cooling. In this scenario, lipid molecules adjacent to the interface do not organize into ordered layers, but crystallize with multiple defects in the crystal structure.

Microbeam X-ray scattering experiments conducted on palm mid-fraction oil droplets demonstrated directly these conclusions, see Fig. 23 [211]. When the interfacial crystallization mechanism was operative due to the presence of a crystallizable surfactant, a preferential

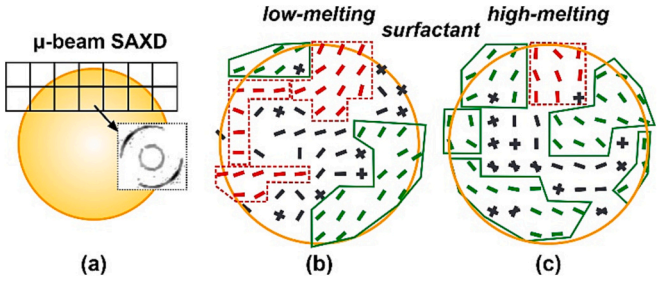

Fig. 23. Effect of surfactant melting temperature for lamellar arrangement in lipid emulsion drops studied by μ-SAXD (microbeam small angle X-ray diffraction) technique. (a) Schematic illustration of the experimental technique. An individual SAXD spectra is obtained from each individual position across the droplet by consecutive scanning using synchrotron radiation X-ray source and highly precise X-ray focusing optics. The microbeam dimensions are 5 × 5 μm^2. (b,c) Interpretation of the obtained results, illustrated for crystallization of palm mid fraction droplet stabilized by: (b) Tween 80 or (c) Tween 80 + high-melting temperature sucrose palmitic acid oligoester (P-170). Each dash represents the orientation of the lamellar planes in the studied spot. The X symbols show randomly oriented lamellar planes. A preferential orientation of the lamellar planes parallel to the drop surface is observed in the presence of P-170 surfactant (see green domains), whereas in the drop stabilized by Tween 80 surfactant solely, the lamellar planes are orientated both in parallel and perpendicular (red domains) to the drop surface. Adapted from Ref. [211]. (For interpretation of the references to colour in this figure legend, the reader is referred to the web version of this article.)

formation of lamellar layers parallel to the drop surface was evident, Fig. 23c. In contrast, when the same emulsion was prepared in the presence of surfactant which hydrophobic tails remained fluid under the studied conditions, no such preferable lamellar plane orientation was observed, Fig. 23b.

The same experimental approach, employing high-intensity synchrotron X-ray radiation with a finely focused microbeam, was applied to investigate the oil crystallization within water-in-oil (w/o) emulsions [212]. The studied fat blend comprised inter-esterified palm stearin/lauric kernel solid fat and rapeseed liquid oil, combined in 1 to 3 ratio. The w/o emulsions were stabilized by PGPR alone or by combination of PGPR and distilled saturated monobehenoyl (C_{22}MAG). The obtained results showed that the addition of crystallizable C_{22}MAG promotes the overall fat crystallization by an increase in both the initial crystallization temperature and the overall solid fat content within the emulsions. At the same time, the addition of C_{22}MAG led to a reduction in the size of the formed fat crystals. Furthermore, microbeam X-ray analysis revealed that the lamellar planes of fat crystals positioned close to the oil-water interface were arranged nearly parallel to the interface for both systems (PGPR ± C_{22}MAG). This finding was interpreted as indicative for the appearance of interfacial crystallization mechanism in both systems [212].

We note that a similar interfacial crystallization mechanism was proven to be crucial in the formation of fluid particulates with various non-spherical shapes prior to their freezing [213–216]. Micrometer-sized droplets of long-chain alkanes, alkenes, alcohols, TAGs, or mixtures thereof were observed to undergo transformations into varied polyhedral, hexagonal, tetragonal, and triangular platelets, rods, fibers and even swimmer-like particles upon cooling. These shape transformations occurred when the surfactant adsorption layer solidified before the lipid material inside the drops froze. It was shown that the surface crystallization allows the formation of well-ordered multilayers of plastic rotator phases adjacent to the drop surface. These multilayers exhibit sufficient mechanical strength to counteract the inner capillary pressure of the liquid oil enclosed within the droplets. Hence, a significant increase in the drop surface area becomes possible, even in the presence of a positive interfacial tension. Such deformations are not possible when the surfactant adsorption layer remains in a liquid state when the lipid molecules undergo a liquid-to-solid phase transition [62,213–216]. Moreover, synchrotron X-ray scattering experiments conducted on these droplets revealed the emergence of plastic rotator phases within the droplets containing a crystallized surfactant adsorption layer, while no such phases were detected in the emulsion samples stabilized by surfactants with shorter tails which remained fluid when the emulsified drops froze [217].

The lamellar arrangement, predominantly influenced by the melting temperature of the adsorbed surfactant, also determines the flexibility of the lipid-water interface and the ease with which polymorphic transformations occur within the droplets. A fluid interface enveloped by unsaturated surfactant molecules retain its flexibility, facilitating molecular rearrangement and thereby enabling polymorphic phase transitions. Conversely, the crystallized interface created by saturated surfactants is substantially stiffer, preserving the stability of the thermodynamically metastable α and β' polymorphs [204]. These rigid layers play also a role in stabilizing the respective emulsions against partial coalescence [196,211].

Besides the long-chain saturated surfactants, a good long-term stability of the metastable α polymorph within tristearin nanoparticles was observed with poly(vinyl) alcohol, PVA. The results show that approximately 40% of the TAG remains in the α phase even after two years of storage at 23 °C. Notably, this percentage increases more than twice, up to 85%, when the particles are stored in a refrigerator at 4 °C [218]. This remarkably slow α → β transition rate has been attributed to the formation of a different than usual, less-ordered α polymorph. When examined using SAXS/WAXS, this phase exhibits the characteristic short-distance peak at 0.42 nm, but the peak for characteristic lamellar thickness within the SAXS region is notably diminished in samples cooled at a rate of 0.5 °C/min or completely absent in the samples cooled at 70 °C/s [218,219]. Further investigations are needed to describe the structure and occurrence of this less-ordered α phase [218]. A similar retarding effect over the α → β polymorph transition was observed for diglyceride surfactants as well [220].

Polymorphic phase transitions in TAGs are also investigated in the presence of various additives in the context of potential application for SLN development as controlled delivery vehicles or encapsulation systems in food, cosmetics and pharmaceutical formulations. In most cases, these additives have been found to promote the formation of thermodynamically stable polymorphs [199,218].

For example, a study involving micrometer-sized tristearin particles demonstrated that the addition of 10 wt% ethyl oleate, oleic acid, isopropyl myristate, or MCT oil let to an almost instantaneous α → β transition. When glyceryl monooleate or tocopheryl acetate (vitamin E) were incorporated within the particles, the transition occurred over a span of approximately 3 h at 25 °C. In the absence of additives, the majority of particles remained in the metastable α-polymorph even after a two-month storage period. As in the case of surfactants, it was suggested that liquid additives provide the necessary molecular mobility to facilitate tristearin rearrangement and induce the polymorphic transformation [199].

The polymorphic form of the TAGs also plays an important role in the release kinetics of active pharmaceutical ingredients (API). The prevailing understanding is that API release is governed by a diffusion-based mechanism. Hence, the porosity of the particles determined by their polymorphic state, along with the concentration of the encapsulated API, has a significant impact on the release kinetics. A study focused on the release of caffeine encapsulated within α- or β-polymorph SSS microspheres demonstrated that the polymorphic phase and the thermal protocol used to prepare β polymorph both influenced the kinetics of caffeine release, as well as the maximum concentration which can be released [221].

In a study exploring SLN of fully hydrogenated sunflower oil (FHSFO, dominant TAG – SSS) and their potential application as carriers for food colorants, it was discovered that the addition of β-carotene at concentrations up to 37.5 wt% to FHSFO did not yield to altered TAG structure upon crystallization [195]. The position of the SAXS peak remained unchanged, with only a slight broadening of the peak observed as the β-carotene concentration increased. This subtle broadening indicated the formation of less ordered inner structure, a notion supported by a marginal lowering of the melting temperature. The incorporated β-carotene remained included within the TAG structure as an amorphous material.

The α → β polymorphic transition was found to proceed relatively quickly (< 30 min) in these samples due to their stabilization by unsaturated surfactants (Tween 80 and sunflower lecithin) and the small particle sizes. Interestingly, despite the average drop size measured by dynamic light scattering being approximately $Z_{ave} \approx$ 120–170 nm, these particles exhibited a strongly asymmetric platelet-like three-dimensional morphology. They possessed average dimensions of 300 nm in length, 100 nm in width and just 7–9 nm in height, as determined through AFM analysis. It was suggested that the carotene-loaded particles had an inner TAG core featuring two TAG layers organized in double chain-length structures. This core was encapsulated by an inner surface layer comprised of the non-crystalline additive, complemented by an outer surfactant layer, see Fig. 24 [195].

The formation of such platelets has been observed in various β-form TAG particles, as discussed in the following section.

6.3. Shape of triglyceride particles in different polymorphic forms

In the literature, it has become widely accepted that the α-form TAG nanoparticles typically have spherical shape, while TAG nanoparticles in the β polymorph are characterized by a platelet shape

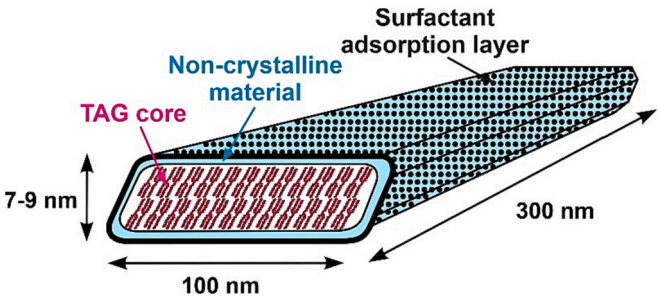

Fig. 24. Schematic structure of β-carotene loaded fully hydrogenated sunflower oil particles. Adapted from Ref. [195].

[26,198,207,222–225]. A collection of illustrative electron micrographs is presented in Fig. 25.

In these studies, the authors directly visualized the inner molecular arrangement of the TAG molecules into lamellar layers oriented parallel to the surface of the particles. The layered structure was observed for both α- and β- particles, as shown in Fig. 25b-d. It has been suggested that the darkest planes appearing in the pictures shown in Fig. 25b,d are the glycerol backbones of TAGs, while the brighter parts represent the FA acyl chains [207]. The repeat distance between the layers, which can be directly measured from the cryo-TEM images, was consistently found to be very similar to the characteristic distance measured for bulk samples of the same chemical composition. Interestingly, in some cases, even a stepped-like structure was demonstrated to appear at the periphery of the particles, Fig. 25c [224]. Similar conclusions about the varying crystalline thickness across the TAG particles were also demonstrated by precise AFM measurements in Ref. [226].

Although many studies demonstrated that platelet-like particles appear when TAG nanodrops crystallize into the β-form, to the best of our knowledge, currently there are no direct *in-situ* observations of this spherulite to platelet transition. Therefore, it remains unknown whether the α → β phase transition is able to induce particle shape change and what would be the mechanism underlying this transformation. Alternatively, it may be possible that the platelet shape is achieved initially upon cooling from melt as previously demonstrated for alkane emulsion droplets of various sizes [213–217,227,228]. In our opinion, it seems unlikely that the polymorphic transition would be able to change the thickness of the solid particles from about 40–50 concentric layers into 10 or less completely parallel layers. Furthermore, the transition from spherical into platelet particle is also related to significant surface area increase which would also increase the energy of the system. We note also that in most of the available micrographs of α and β particles, both platelets and spherical objects are seen, although with different frequency. Finally, it should be pointed out that a microbeam X-ray study of 2D LLL spherulites grown between poly ethylene terephthalate films, demonstrated that the orientation of the long-chain axis of the LLL molecules remained unchanged after a polymorphic β' to β transition [223]. No shape changes were observed either, hence the authors concluded that the transformation occurred in a well-controlled manner through a template effect of the mother β' phase [223].

Note that similar platelet-like structures were observed also in bulk TAG mixtures containing solidified longer TAGs, mixed with liquid TAGs containing shorter or unsaturated FA residues. These crystalline nanoplatelets served as primary units for the formation of 1-dimensional cylindrical aggregates (TAGwoods) which aggregate further to form fractal crystalline network in the fat volume, see Section 4.6 for details [164,173,174,176–180,182].

The effect of surfactant type and the initial drop size over the observed morphologies of the particles, also remains unclear. For example, platelet-like PPP particles are observed to form predominantly from nanoemulsions, stabilized by polysorbate surfactants, while spherical particles were prepared under identical conditions in presence of sodium caseinate, see Fig. 25e,f. Furthermore, in a study of micrometer-size TAG particles, the α → β transition was directly observed *via* optical microscopy in Refs. [44, 157], see also the

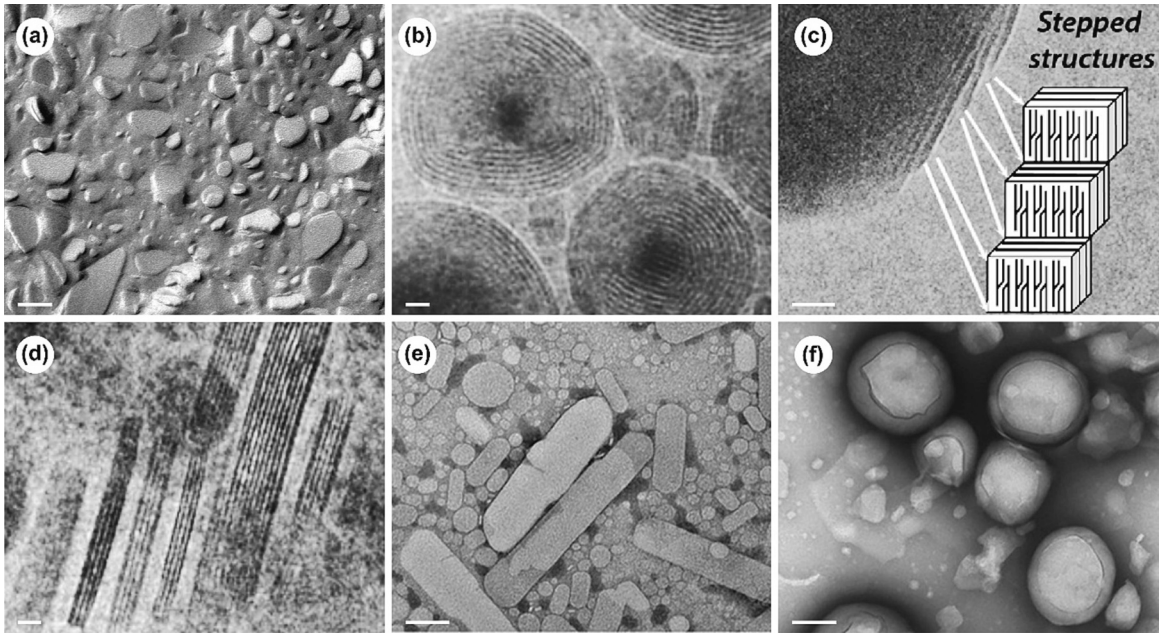

Fig. 25. Microscopy images of TAG nanoparticles. (a) Freeze-fracture TEM image of 20 wt% β-MMM suspension, stabilized by soybean lecithin S100 and sodium glycocholate. (b-d) Cryo-TEM images of TAG nanoparticles. (b,d) Spherical, α-PPP (b) and platelet-like β-PPP particles stabilized by saturated soybean lecithin S100–3 and sodium glycocholate. (c) Particle prepared from olein fraction of anhydrous milk fat, stabilized by sodium caseinate. A stepped structure at the oil-water interface is observed. (e) Platelet like particles co-existing with spherical particles obtained from PPP nanoemulsion, stabilized by Tween 20 surfactant. (f) Spherical PPP particles, stabilized by sodium caseinate. Scale bars: (a,e,f) 100 nm; (b,c,d) 20 nm. The images are adapted and reprinted with permission from: (a) Ref. [229], copyright © 2014, American Chemical Society; (b,d) Ref. [207], copyright © 2007, American Chemical Society; (c) Ref. [224], copyright 2015 © Elsevier; (e,f) Ref. [197], Wiley – open access.

discussion for the concomitant cold-bursting phenomenon in Section 6.6 below. The polymorphic transition was easily detected due to the different mass densities of the α and β phases. Initially, upon crystallization from melt the TAG molecules arranged in the unstable α polymorph, which has lower mass density, as in the case of liquid TAG. Upon heating or prolonged storage, the α → β transition occurred. The β polymorph has higher mass density than the aqueous phase, hence this transition was manifested by a change in the position of the particles within the capillary, *viz.* the particles fell to the bottom of the capillary disappearing from the observed optical plane. No any shape changes were observed after this transition. Moreover, the cryo-TEM imaging of 20 nm SLN produced by the cold-bursting process did not showed any platelets present in the sample, see Fig. 26a. In contrast, depending on the surfactant stabilizing the emulsions – in some cases we observed the formation of non-spherical particles during the cooling process *via* the spontaneous drop self-shaping mechanism [214] or immediately when the drop crystallization occurred most probably *via* the so-called "crystal comet" mechanism, involving a dewetting of the (still) fluid component from the already frozen one [230,231].

Therefore, further experiments would be needed to reveal the exact mechanism of β-platelets formation, its relation to the α-spherulites and the influence of the processing conditions (cooling rate, initial drop size, surfactant type and concentration).

The shape of multicomponent TAG particles has been also studied. Small 20 nm nanoparticles prepared from six-component TAG mixture with total FA content resembling the one in natural CNO oil were found to be spherical in shape, see Fig. 26a [157]. As discussed for bulk TAG mixtures, section 4, a phase separation is expected to occur when the TAG molecules have significantly different FA acyl chains. This phase separation led to the formation of somewhat unusual shapes for particles prepared from the mixture of MCT and Compritol 888 ATO (comprising a mixture of *ca.* 15% MAGs, 50% DAGs and 35% TAGs with about 80% C_{22} FA acyl chains), see Fig. 26b,c [225]. The low-melting temperature MCT fraction was observed to phase separate, thus forming a liquid droplet sticking to one of the sides of the frozen Compritol 888 ATO platelets. Part of the formed structures at higher MCT content resembled the shape of a spoon (with the bowl being the MCT drop and the handle – the frozen nanoplatelet), thus they were termed as "nanospoons" [225].

The shape of the particles has been found to be important for various reasons. For instance, a study investigating the incorporation of α-tocopherol (vitamin E) into TAG nanoparticles composed of CaCaCa, PPP, of mixtures thereof showed that the best chemical stability of the encapsulated active ingredient was achieved when it was included within the liquid CaCaCa nanoparticles [197]. In contrast, the amount of α-tocopherol found to remain stable after two weeks storage in crystalline PPP particles was significantly lower (≈ 60–80% for PPP *vs.* about 95% for CaCaCa). This effect was particularly pronounced in particles with highly asymmetric platelet-like shape (Fig. 25e), whereas slightly higher chemical stability was observed in spherical PPP particles produced using sodium caseinate as emulsifier, see Fig. 25f. The observed effect was attributed to the potential exclusion of α-tocopherol from the crystalline structure of the ordered PPP molecules, demonstrating that the use of solid lipid carriers does not necessarily lead to increased stability of the encapsulated material. The results obtained from the CaCaCa-PPP 1:4 blend were found to be strongly influenced by the specific surfactant used in the initial nanoemulsion. However, they appeared to be intermediate between those obtained with solid and liquid nanoparticles [197].

Next, we discuss how the platelet shape of β-TAG may influence their arrangement within the aqueous dispersions at elevated TAG concentrations (5–20%).

6.4. *Stacking of β-platelet SLN*

The shape of dispersed particles is known to affect also the rheological properties of the dispersed systems. Interestingly, a gelation was observed at relatively low oil volume fractions (≈ 10 wt%) for systems containing TAG nanoparticles prepared from nanoemulsions stabilized by ionic surfactants (sodium glycocholate or cetylpyridinium chloride) in combination with phospholipid surfactants (lecithins) [208,232]. No such viscosity increase was observed in the absence of ionic surfactant [208]. As already discussed, these SLN are found to have strongly asymmetric platelet shape with thickness of a few molecular layers only and much larger diameter, leading to aspect ratio ≈ 12–15 [233].

The X-ray scattering analysis of these samples showed additional lamellar peaks present in the SAXS region for samples containing TAG particles at concentration above a threshold value, see Fig. 27a (note that these concentrations are lower than the one needed for sample gelation). This peak was explained with the spontaneous self-assembly of the thin platelet particles into stacked lamellae [222,229,233,234]. The stacks consisted of almost parallelly oriented particles with a rather narrow size distribution as directly observed by electron microscopy [222,233]. These ordered structures co-existed with isolated single platelets, see Fig. 27d.

The formation and disintegration of stacked particle assemblies was found to be a reversible process. It did not depend on the preparation conditions but only on the specific chemical compounds used, on the particle size and also (strongly) on the TAG concentration. The critical particle concentration above which the formation of stacks was observed was about 6 wt%, see Fig. 27b [229,233,234]. It depended on the specific TAG used as it determined the aspect ratio of the platelet particles. Particles prepared with longer TAGs were thinner and bigger

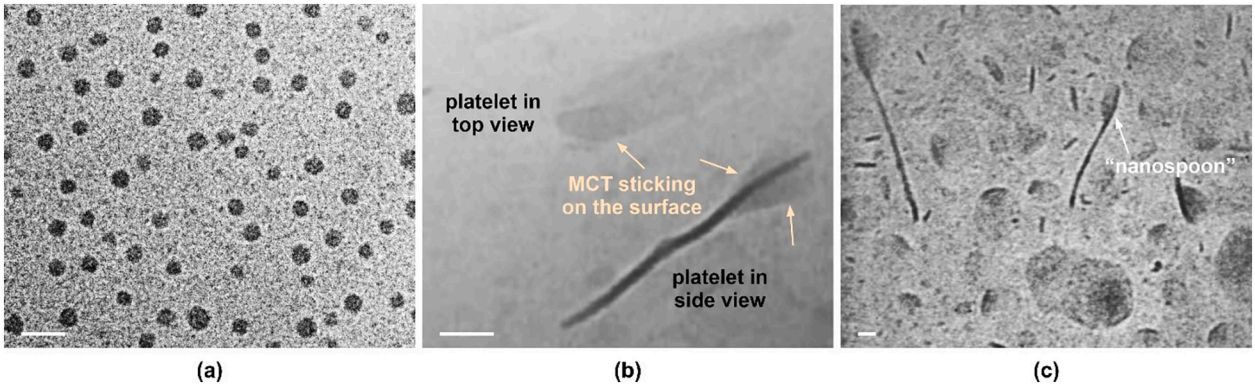

Fig. 26. Cryo-TEM images of mixed TAG nanoparticles. (a) Nanoparticles prepared *via* the cold-bursting process with six-component TAG mixture (CaCaCa:CCC:LLL:MMM:PPP:OOO = 7:8:50:18:10:7) and stabilized by Tween 20 + $C_{18:1}$MAG surfactants. (b,c) Nanoparticles prepared with MCT + Compritol 888 ATO mixture in 1:9 (b) and 3:7 (c) ratios. The phase separation between MCT and Compritol 888 ATO leads to the formation of platelets with sticking MCT droplets on their surface. Scale bars: 50 nm. Images in (b,c) are reproduced and adapted with permission from Ref. [225], copyright 2004 © Elsevier.

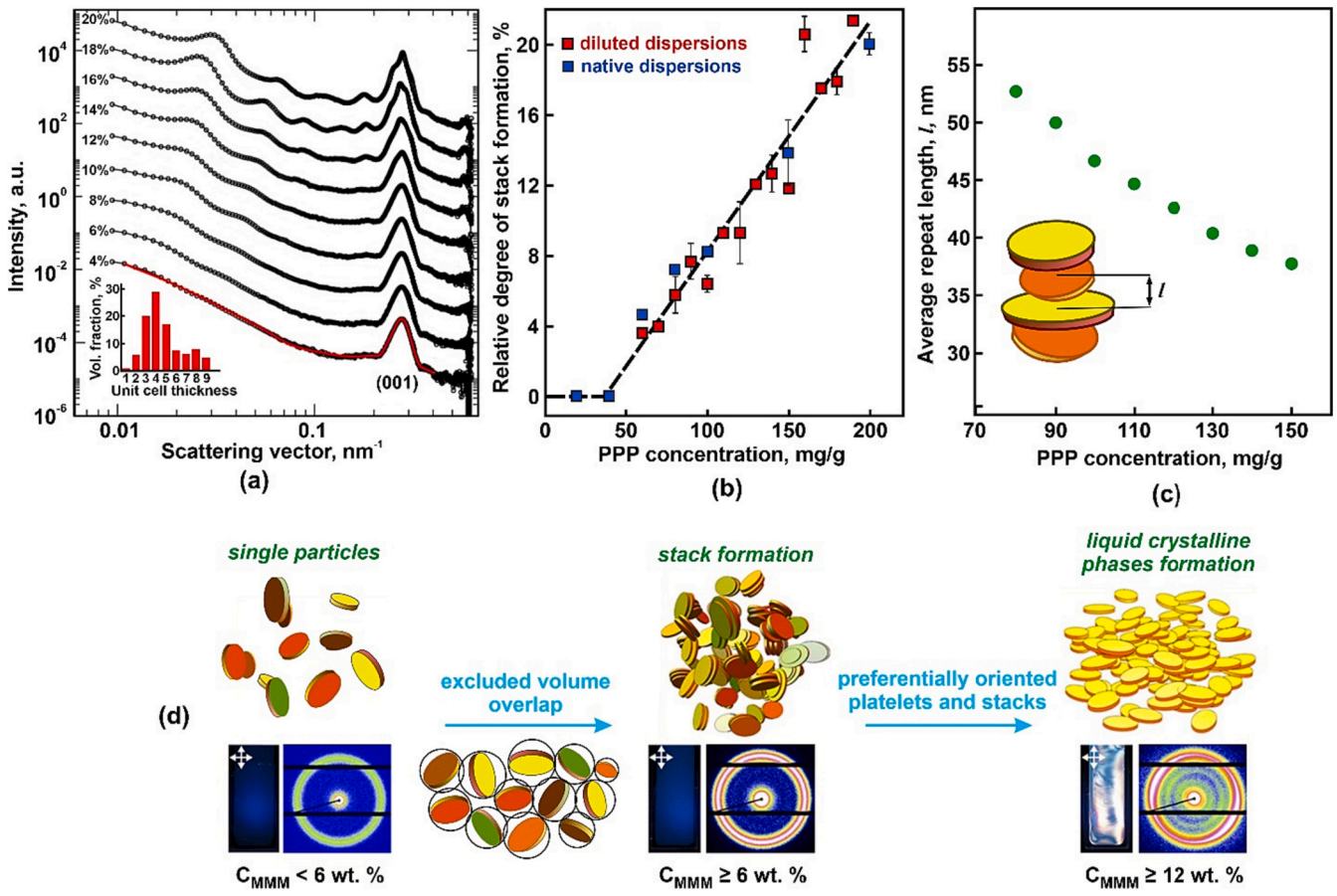

Fig. 27. Stack and liquid crystalline arrangement of β-TAG platelets. (a) SAXS patterns of MMM suspensions of different MMM concentrations. The inset shows the platelet thickness distribution as a function of the number of unit cells of MMM for 4% MMM dispersion. (b) Effect of PPP concentration on the relative degree of stack formation. (c) Effect of PPP concentration over the average repeat length, l = particle thickness + interparticle distance. (d) Schematic representation of the transitions observed in MMM suspensions, depending on the MMM concentration. The bottom section of the image displays illustrative 2D SAXS spectra and photographs of cuvettes filled with MMM suspensions captured under cross-polarized light. (a,d) Adapted and reprinted with permission from Ref. [229]. Copyright © 2014, American Chemical Society. (b,c) Adapted from Ref. [233].

in diameter, compared to the particles prepared from drops with similar sizes but containing shorter TAG molecules. Hence, lower concentrations were needed for particles prepared with longer TAGs. The increase of the TAG concentration led to a linear increase of the fraction of particles arranged in stacks, while the repeat distance between the platelets in an individual stack decreased, Fig. 27c [229,233]. Moreover, above a given TAG concentration, nematic liquid crystalline phase was observed, most probably due to the increased interactions between the individual stacks. For MMM suspension, the critical concentration for formation of birefringent liquid crystalline phase was ≥12 wt%, see Fig. 27d [229].

The observed self-assembly phenomenon was explained with the steric restrictions arising from the highly anisotropic particle shape and with the overlap of the particle exclusion volume above a given threshold concentration [233]. The free rotational movement of the anisotropic particles would be possible only if the spherical volume defined by their longest size is completely free of other particles. However, this exclusion volume is much larger compared to the particle volume *per se*. Furthermore, the ionic surfactant adsorption layer on the surface of the particles further increases the particle exclusion volume, due to the electrostatic repulsion between the particles. A comparison between the highest volume fraction for packing of spherical objects (≈ 74%) and the critical volume fraction at which the individual particles exclusion volumes starts to overlap, shows that the experimentally observed threshold value for formation of self-assembled structures is close to the theoretical one. This explanation was also in a good agreement with the experimental observations that: larger in size particles have greater tendency to associate in stacks; increase in fraction of arranged platelets when the concentration of the SLN was increased and also, the increase of ionic surfactant concentration at a given PPP concentration led to a decrease in the repeat unit distance [233].

A comprehensive analysis of the SAXS and SANS spectra obtained from such samples gave further details about the structure of lamellae stacks in different systems [234,235]. In particular, it was demonstrated that the specific surfactant used for stabilization of the 10 wt% PPP nanoparticle dispersion affected the preferential number of stacks found in a given system. For example, systems stabilized by DLPC (1,2-dilauroyl-*sn*-glycero-3-phosphocholine) or DOPC (1,2-dioleoyl-*sn*-glycero-3-phosphocholine) phospholipid emulsifiers arranged predominantly in stacks consisting of 3 particles, while mainly stacks with 2 particles were observed for S100 (purified soybean lecithin, ≥ 94% phosphatidylcholine, rich in doubly unsaturated 18:2 FA) stabilized dispersions [234]. This difference may be due to the different sizes of the platelets stabilized by DLPC or DOPC ($d \approx 135$ nm) compared to S100 ($d \approx 120$ nm).

These findings were used to prepare a nanocomposite suspension of platelets with partially condensed DNA positioned between the platelets with potential application in gene therapy [236].

6.5. Triglyceride nanoparticles studied by MD simulations

The direct methods for observation of the TAG particles structure

have achieved resolution down to a single lamellar plane [207]. More details about the specific molecular arrangement and conformations can be provided by MD simulations.

All-atom MD simulations of tripalmitin nanoparticle, $R_g \approx 5.5$ nm, stabilized by polyoxyethylene-10 oleyl ether nonionic surfactant (Brij O10, $C_{18:1}EO_{10}$) [47] shows that almost all TAG molecules located close to the surface adopt the trident conformation forming a shell of trident lipids with a thickness of *ca.* 2.3 nm. The limited number of non-trident molecules at the surface were located at the crystalline subcell surface of the trident molecules, thus protecting their hydrocarbon tails that would be otherwise exposed to water. The MD simulations were performed with 229 tripalmitin and 650 surfactant molecules making the number of TAG molecules located in the particle interior very limited. Nevertheless, the results showed that these molecules adopt preferentially chair and tuning fork conformations. Interestingly, the molecules in a given conformation tend to crystallize together forming a crystalline solid with considerable defects. It was suggested that these voids in the crystalline packing may be suitable spaces for incorporation of drug or other types of bioactive molecules [47]. Note that similar molece sized voids were independently found by SANS experiments for crystallizing trilaurin as discussed in Section 3.2 [93].

6.6. *Spontaneous cold-bursting process*

Finally, we show how the intricate comprehension of TAG polymorphism, the factors influencing the crystal nucleation ang growth and the polymorphic transformations, can be applied to gain a detailed understanding and control of novel phenomena observed in TAG-in-water

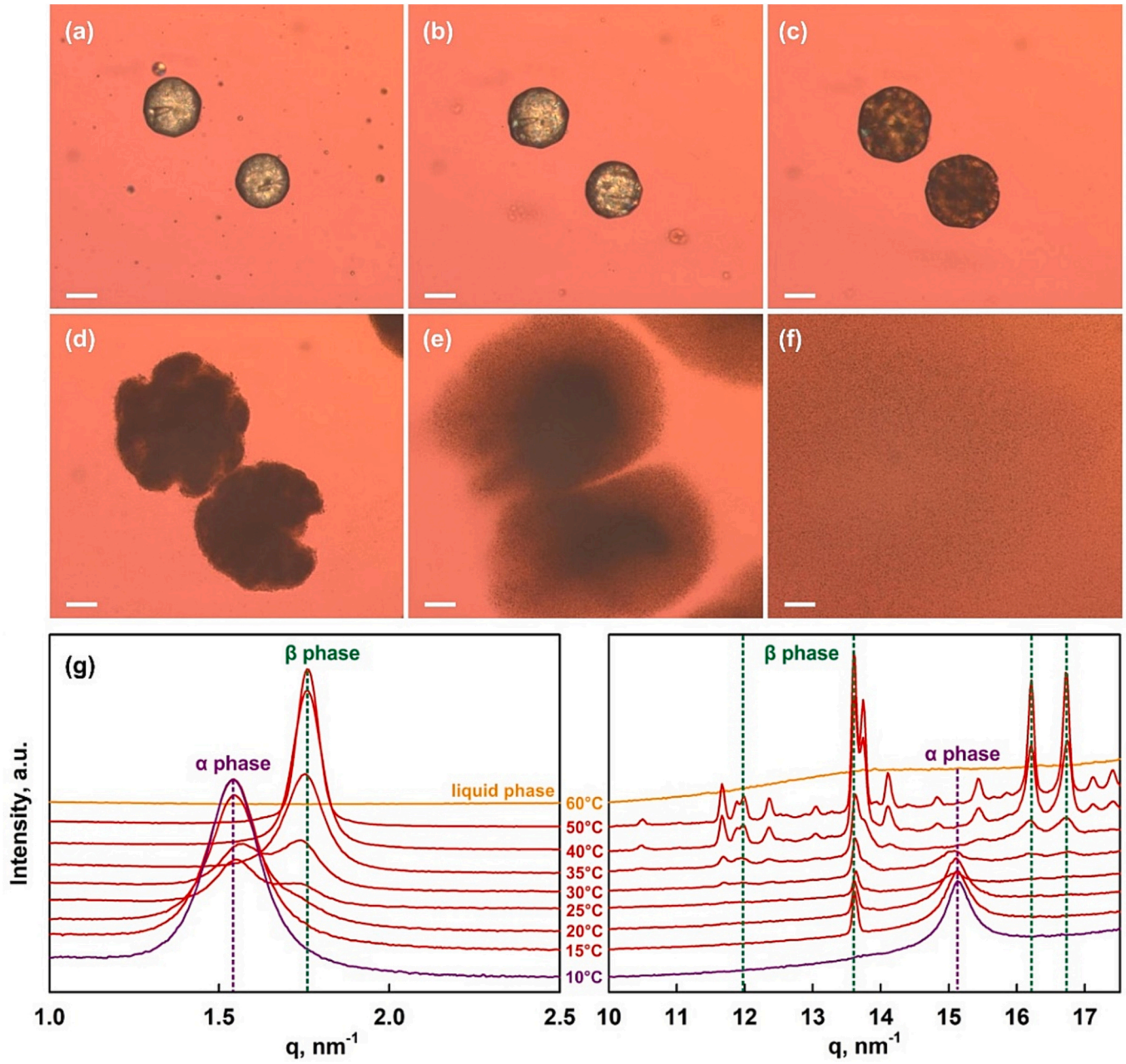

Fig. 28. Optical microscopy pictures illustrating the spontaneous cold-bursting process and SAXS/WAXS spectra showing the polymorphic transformations in the sample. (a-f) Optical microscopy images showing the spontaneous bursting of PPP particles, stabilized by Brij S20 and monoolein surfactants. Initial particle size is ≈ 90 μm, whereas the small drops formed after cold-bursting are with sizes ≈ 0.4 μm. Scale bars: 50 μm. (g) SAXS and WAXS spectra showing the α → β polymorphic transformation proceeding upon heating. Adapted and partially reprinted with permission from Ref. [44], copyright © 2020, American Chemical Society.

dispersions.

The polymorphic α → β phase transition in small micrometer and submicrometer TAG lipid particles, along with the associated increase in mass density and the formation of voids between the separate crystalline domains (see Section 2), has recently been identified as the cause of an unexpected and efficient phenomenon of spontaneous disintegration of TAG particles. This phenomenon, called "cold-bursting", is capable of generating particles as small as 20 nm (see Fig. 26a), starting from an initial coarse emulsion, solely through cooling and possible heating, without requiring any mechanical energy input. The process is termed "cold-bursting" because the initial mother particles can disintegrate spontaneously into thousands or millions of smaller nanoparticles simply by storing the sample at low temperatures [44,157,189]. The cold-bursting phenomenon, along with the related process of double emulsion formation are broadly applicable and were observed with numerous single TAGs [44], model mixtures of monoacid TAGs [157] and even with natural TAG oils, including coconut oil, cocoa butter, palm kernel oil and others [189].

Optical microscopy images, illustrating the cold-bursting process are presented in Fig. 28, along with a SAXS/WAXS spectra demonstrating the α to β transition in the frozen particles. The mechanisms underlying the observed phenomena are schematically shown in Fig. 29. Shortly, upon cooling, the fluid TAG droplets crystallize into the metastable α phase. Afterwards, upon prolonged storage or upon heating of the sample above the melting temperature of the unstable α-polymorph, a polymorphic phase transition from α- into β-form occurs, see SAXS/WAXS spectra in Fig. 28g. As explained in Section 6.3 above, this polymorphic transformation is easily detected even without structural analysis due to the mass density change observed. The β phase has higher mass density than water, thus once it is formed within the particles they sedimented to the bottom of the container.

This polymorphic transition causes the formation of inner nanoporous structure, allowing the continuous surfactant solution in which the TAG particles are dispersed, to penetrate inside the frozen particles, Fig. 29b. In the microscopy pictures, this process is observed as a significant increase of the particle volume accompanied with a disappearance of the bright colors observed in polarized light. Afterwards, either disintegration of the initial micrometer size particles into millions of nanometer-sized particulates or formation of double water-in-oil-in-water (w/o/w) emulsion droplets in the moment of particle melting was observed [44,157]. The disintegration process can be observed also at low temperatures ($T << T_m$), providing that there is sufficient time for aqueous phase penetration and subsequent disintegration. The double emulsion formation can be observed only after the TAG particle is melted. The double w/o/w drops form when the penetrated aqueous phase become trapped inside the melting lipid drop instead causing its disintegration.

A detailed investigation of the behavior of various TAG-surfactant combinations revealed that the behavior of a given system is governed by the wetting properties of the aqueous surfactant solution over the TAG substrate. In particular, for single component TAG particles, disintegration process was observed when the three-phase contact angle measured through the aqueous surfactant solution was $\theta \lesssim 50^\circ$ when measured through the aqueous phase, see Fig. 21 for the method of measurement. In contrast, for systems in which the aqueous solution was unable to wet well the TAG substrate, *i.e.* three-phase contact angle $\theta \gtrsim 100^\circ$, double emulsion droplets were typically formed [44].

The situation become more complicated for particles prepared with

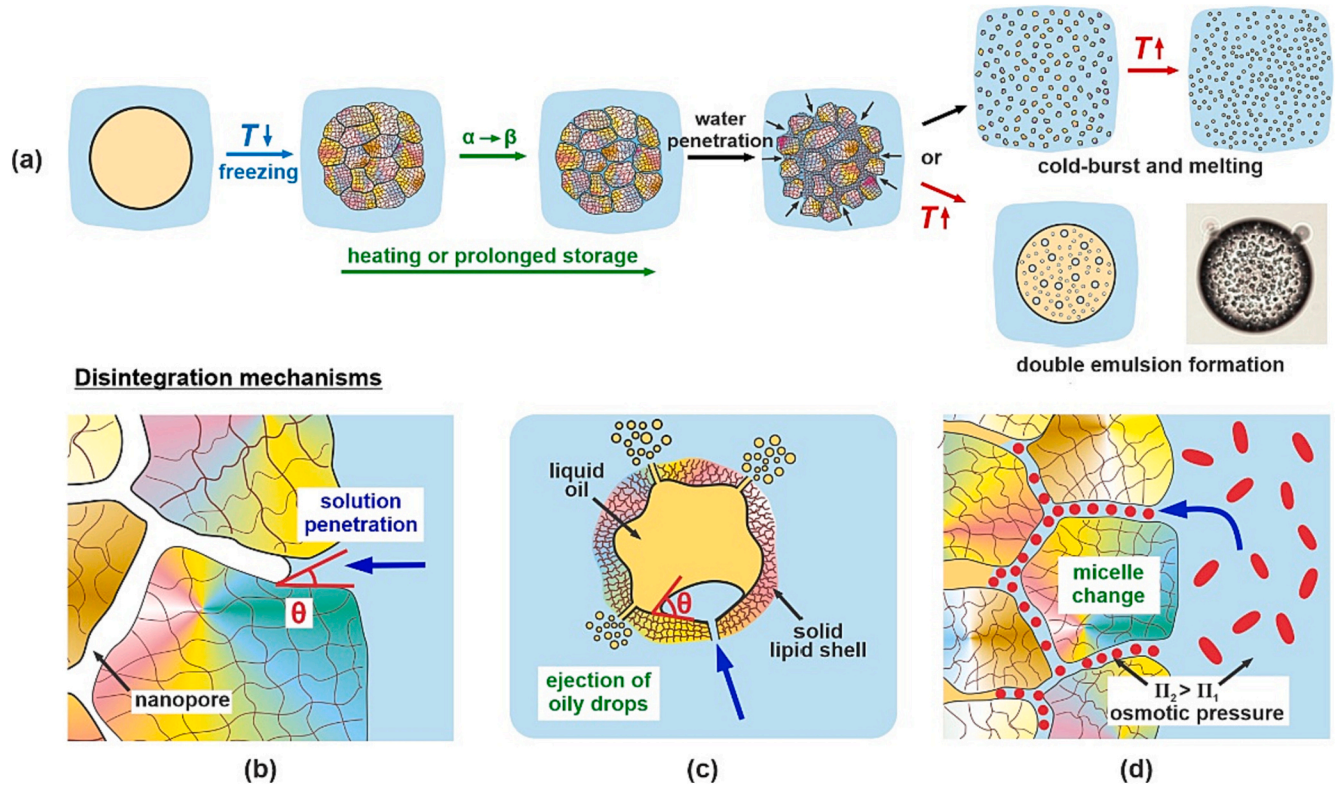

Fig. 29. Schematic illustration of the cold-bursting process and the related disintegration mechanisms. (a) Main stages observed upon cooling and heating of emulsified TAG samples. (b-d) Mechanisms identified to be operative for disintegration of the big TAG particles into nanoparticles. (b) Aqueous surfactant solution penetration into the inner nanoporous structure. This mechanism is operative for all systems. (c) Ejection of oily droplets due to the occurrence of lipid phase separation (operative only for TAG mixtures). (d) Formation of osmotic pressure gradient between the outer and inner aqueous phases. This mechanism is operative when the initial aqueous solution contains mixed surfactant micelles, dissolved salts or thread-like micelles. Illustrated on the picture is the concentration gradient arising from changes in the size and number of the surfactant micelles upon penetration of the surfactant solution into the inner nanoporous structure in the particle interior. Reproduced with permission from Ref. [157], copyright 2023 © Elsevier.

model monoacid TAG mixtures [157] or when natural TAGs were used [189]. The main reason is that the melting process in TAG mixtures does not occur in a narrow temperature interval around a given temperature. Instead, as discussed in Section 4, a co-existence between solid and liquid domains is observed in wide temperature interval. As a result, the wetting properties should no longer be considered only for the aqueous solution-frozen lipid interface, but also the molten lipid phase should be able to dewet the chemically similar frozen substrate to induce efficient particle disintegration. Such phase separation between TAG molecules with different FA moieties was observed, for example, in experiments with CNO drops in which an ejection of liquid drops was seen prior to the melting of the solid lipid particle shell, see Fig. 29c.

Another mechanism which turn to be particularly efficient for particle disintegration was the induction of osmotic pressure gradient between the continuous aqueous phase and the aqueous phase which has penetrated inside the TAG particle. Such osmotic pressure effect arises when the chemical composition of these two aqueous solutions is not completely identical. This effect was realized in practice by several possible ways: (1) By using aqueous surfactant solution containing large non-spherical molecular aggregates. This approach could be realized by either using combinations of water-soluble surfactants and some co-surfactants known to change the shape of the surfactant micelles or by solubilizing oil-soluble surfactants inside the water-soluble surfactant micelles [189]. In the case of oil- and water-soluble surfactant combination, bigger supramolecular aggregates were formed in the aqueous solution (the solution became turbid). Once these aggregates penetrated inside the nanoporous structure, the oil-soluble surfactant escaped from them because it adsorbed on the TAG surfaces (or was dissolved into the already molten TAG). As a result, higher in number and smaller in size water-soluble surfactant micelles were formed. Accordingly, the number of micelles inside the nanopores become higher inducing osmotic pressure gradient which sucked water into the nanoporous network and thus facilitated the particle disintegration, see Fig. 29d. (2) By adding electrolyte to the aqueous surfactant solution [237]. Using these approaches, we were able to prepare nanoparticles even with natural TAG oils and other pharmaceutically relevant lipids [189,237].

The co-existence between solid and liquid TAG domains at a given temperature, led to another somewhat unexpected result. Depending on the cooling and heating rate applied to a given sample, we were able to either observe complete particle disintegration process or to obtain double w/o/w emulsion droplets from systems with equivalent chemical composition [157]. The outcome was entirely kinetically controlled and a precise control over the system behavior was achieved by changing the applied cooling and heating protocol only. The most efficient disintegration was observed when the TAG particles were initially cooled quickly from melt and then slowly heated until melting. In contrast, most efficient water entrapment and double emulsion formation were observed when the drops were cooled slowly and then the frozen TAG particles were heated quickly. The cooling effect is easily understood considering the size of lipid domains formed – slow cooling allows the formation of smaller in number and bigger in size domains, whereas upon fast cooling the crystalline domains are higher in number and smaller in size. Accordingly, the slower heating ensures sufficient time for aqueous phase penetration and subsequent particle disintegration, whereas upon quick heating the aqueous phase become trapped inside the melting TAG droplets, see Fig. 30.

Further details about the mechanisms, applicability and parameters which can be used to control these fascinating processes can be found in the original papers [44,157,189,237].

7. Conclusions

This review paper explores the formation of triglyceride (TAG) polymorphs and the transitions between them in diverse scenarios. Beginning with the fundamental principles governing the crystallization process and polymorphic phase transitions in bulk monoacid TAGs, we demonstrate the universality of these principles, extending not only to mixed TAG systems and TAG layers, but also to significantly more complex emulsified systems. By adopting this comprehensive approach, we provide an in-depth overview that has not been previously depicted in other works discussing TAGs phase transitions and polymorphism [54,66,154,164].

The nucleation process from the molten state is always enhanced when suitable nucleation sites are available for heterogeneous nucleation. In bulk TAGs, this is attained by introducing surfactants at concentrations exceeding their solubility limit, provided that their hydrophobic tails are structurally similar to the FA residues within the TAG molecules. Similar approach can be applied to emulsified systems as well, where the presence of a crystalline surfactant adsorption layer often induces a heterogeneous nucleation, initiated on the surface of the droplets.

The formation of the least stable α polymorph is enhanced when higher cooling rates and/or greater supercooling are applied. The crystallization rate leading to the formation of hexagonal α phase is usually the fastest. Molecules in this α phase exhibit significant molecular freedom, allowing their chain-end groups to perform torsional oscillation. This feature makes the α phase similar to the rotator phases found in alkanes or to the “gel phases” typical for phospholipids and soaps. In contrast, significantly lower cooling rates or a prolonged storage time is required for formation of crystalline nuclei at temperatures exceeding the melting point of the less stable α and β’ polymorphs. Under such conditions, a direct crystallization into the most stable

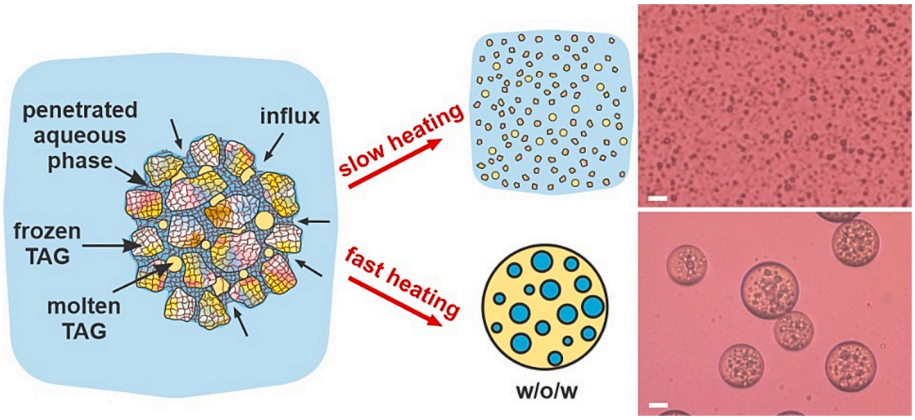

Fig. 30. Particle bursting *vs* double emulsion formation. Schematic presentation of the competition between these two processes observed in TAG drops containing mixed TAG molecules. The same surfactant-TAG system can exhibit both scenarios, depending on the applied cooling and heating rates. Reproduced with permission from Ref. [157], copyright 2023 © Elsevier.

triclinic β polymorph is possible.

The polymorphism in TAGs is of monotropic type, making the α → β' → β and α → β transitions irreversible. The presence of structural defects within the TAG structure always accelerates the polymorphic transitions for systems arranged in one of the less stable forms. This effect is usually attributed to the increase in the molecular mobility required for the rearrangement of the TAG molecules. Various approaches can achieve this effect, depending on the system studied. Examples include introducing foreign molecules, liquid additives, or particles into the TAG phase in both the bulk and emulsified systems. Additionally, in emulsions, this effect can be achieved by reducing the drop size or by using surfactants that remain fluid during the TAG crystallization.

The present review presents also numerous examples highlighting the significance of TAG polymorphism in various industrial applications. These examples range from the preparation of solid lipid nanoparticles to the preparation of viscous systems exhibiting nematic liquid crystalline order at relatively low lipid concentrations, attributed to the intricate lipid particle shape observed in β phase. The recently discovered "cold-bursting" process is also briefly reviewed, emphasizing how a comprehensive understanding of the TAG properties and polymorphism can guide the control of novel self-emulsification processes without any costly equipment. In this particular case, the production of nanoparticles with sizes down to 20 nm is achieved just by cooling and heating of the sample.

The recent development of highly brilliant synchrotron sources, combined with the powerful computational resources, has facilitated the direct investigation of the inner molecular arrangement of TAGs in a variety of scenarios. This progress has led to the elucidation of the mechanisms behind crystal network formation and its relation to the mechanical properties of fats, the observed stabilization/destabilization of disperse systems, the influence of the oil-water interface for TAG crystallization, the molecular details of TAG mixing, and more. However, there are many open questions which remain to be answered, including: the arrangement of TAG molecules in liquid state, the mechanism of formation of molecular compounds in TAG mixtures, the distinct roles of temperature and particle size for stabilization of the least stable phases, the mechanism behind the creation of β-nanoplatelets, and many others. Therefore, we anticipate that the current review will serve as a solid basis and will inspire the researchers to explore these and other related phenomena in lipid systems.

CRediT authorship contribution statement

Diana Cholakova: Conceptualization, Investigation, Visualization, Writing – original draft, Writing – review & editing. **Nikolai Denkov:** Conceptualization, Funding acquisition, Writing – review & editing.

Declaration of Competing Interest

The authors declare that they have no known competing financial interests or personal relationships that could have appeared to influence the work reported in this paper.

Data availability

Data will be made available on request.

Acknowledgements

The study was funded by Bulgarian Ministry of Education and Science, under the National Research Program "VIHREN", project ROTA-Active (no. KP-06-DV-4/16.12.2019).

References

[1] German JB, Dillard CJ. Crit Rev Food Sci Nutr 2006;46:57. https://doi.org/10.1080/10408690590957098.
[2] Foster R, Williamson CS, Lunn J. Nutr Bull 2009;34:4. https://doi.org/10.1111/j.1467-3010.2008.01738.x.
[3] Biermann U, Bornscheuer U, Meier MAR, Metzger JO, Schäfer HJ. Angew Int Ed Chem 2011;50:3854. https://doi.org/10.1002/anie.201002767.
[4] Hariri N, Thibault L. Nutr Res Rev 2010;23:270. https://doi.org/10.1017/S0954422410000168.
[5] Vucetic Z, Kimmel J, Totoki K, Hollenbeck E, Reyes TM. Endocrinology 2010;151:4756. https://doi.org/10.1210/en.2010-0505.
[6] Mattson MP, Allison DB, Fontana L, Panda S. Proc Nat Acad Sci U S A 2014;111:16647. https://doi.org/10.1073/pnas.1413965111.
[7] Wan Y, Wang F, Yuan J, Li J, Jiang D, Zhang J, et al. Gut. 2019;68:1417. https://doi.org/10.1136/gutjnl-2018-317609.
[8] Lin T-K, Zhong L, Santiago JL. Int J Mol Sci 2018;19:70. https://doi.org/10.3390/ijms19010070.
[9] Draelos ZD. J Cosmetic Derm 2018;17:8. https://doi.org/10.1111/jocd.12469.
[10] Chuberre B, Araviiskaia E, Bieber T, Barbaud A. JEADV 2019;33:5. https://doi.org/10.1111/jdv.15946.
[11] Pakkang N, Uraki Y, Koda K, Nithitanakul M, Charoensaeng A. J Surf Deter 2018;21:809. https://doi.org/10.1002/jsde.12189.
[12] Mitri K, Shegokar R, Gohla S, Anselmi C, Müller RH. Int J Pharm 2011;414:267. https://doi.org/10.1016/j.ijpharm.2011.05.008.
[13] Jenning V, Thunemann AF, Gohla SH. Int J Pharm 2000;199:167. https://doi.org/10.1016/S0378-5173(00)00378-1.
[14] deMan JM. Food Res Int 1992;25:471. https://doi.org/10.1016/0963-9969(92)90172-2.
[15] Kulkarni C. Nanoscale 2012;4:5779. https://doi.org/10.1039/c2nr31465g.
[16] Moens K, De Clercq N, Verstringe S, Dewettinck K. Cryst Growth Des 2015;15:5693. https://doi.org/10.1021/acs.cgd.5b00665.
[17] Chen J, Ghazani SM, Stobbs JA, Marangoni AG. Nat Commun 2021;12:5018. https://doi.org/10.1038/s41467-021-25206-1.
[18] Buscato MHM, Hara LM, Bonomi EC, GdA Calligaris, Cordoso LP, Grimaldi R, et al. Food Chem 2018;256:390. https://doi.org/10.1016/j.foodchem.2018.02.127.
[19] Lonchampt P, Hartel RW. Eur J Lipid Sci Technol 2004;106:241. https://doi.org/10.1002/ejlt.200400938.
[20] Inugala S, Eedara BB, Sunkavalli S, Dhurke R, Kandadi P, Jukanti R, et al. Eur J Pharm Sci 2015;74:1. https://doi.org/10.1016/j.ejps.2015.03.024.
[21] Nanjwade BK, Patel DJ, Udhani RA, Manvi FV. Sci Pharm 2011;79:705. https://doi.org/10.3797/scipharm.1105-09.
[22] Zheng M, Falkeborg M, Zheng Y, Yang T, Xu X. Coll. Surf. A 2013;430:76. https://doi.org/10.1016/j.colsurfa.2013.03.070.
[23] Hart SM, Lin XL, Thilakarathna SH, Wright AJ. Food Chem 2018;260:145. https://doi.org/10.1016/j.foodchem.2018.03.142.
[24] Borduas M, Spagnuolo PA, Marangoni AG, Corradini MG, Wright AJ, Rogers MA. Food Chem 2022;382:132326. https://doi.org/10.1016/j.foodchem.2022.132326.
[25] Jiao W, Li L, Yu A, Zan S, Chen Z, Liang Y, et al. Food Chem 2022;368:130723. https://doi.org/10.1016/j.foodchem.2021.130723.
[26] Huynh S, Wright AJ. J Am Oil Chem Soc 2018;95:161. https://doi.org/10.1002/aocs.12004.
[27] Clarkson CE, Malkin T. J Chem Soc 1934:666. https://doi.org/10.1039/JR9340000666.
[28] Larsson K. Acta Chem Scand 1966;20:2255. https://doi.org/10.3891/acta.chem.scand.20-2255.
[29] Bernstein J. Polymorphism in molecular crystals. 2nd ed. Oxford University Press; 2002.
[30] Heintz W. Jahresber. 1849;2:342.
[31] Duffy P. J. Chem. Soc. Lond. 1853;5:197.
[32] Duffy P. J Chem Soc Lond 1853;5:303.
[33] Ghazani SM, Marangoni AG. Cryst Growth Des 2023;23:1311. https://doi.org/10.1021/acs.cgd.2c01334.
[34] Lutton ES, Fehl AJ. Lipids 1970;5:90. https://doi.org/10.1007/BF02531101.
[35] Bailey AE, In Bailey AE, Hilditch TP, Longenecker HE, Markley KS. Melting and Solidification of Fats. Wiley (Interscience); 1950.
[36] Small DM. The physical chemistry of lipids: From alkanes to phospholipids. New York: Plenum; 1986.
[37] Takeguchi S, Sato A, Hondoh H, Aoki M, Uehara H, Ueno S. Molecules 2020;25:5086. https://doi.org/10.3390/molecules25215086.
[38] Higami M, Ueno S, Segawa T, Iwanami K, Sato K. J Am Oil Chem Soc 2003;80:731. https://doi.org/10.1007/s11746-003-0765-2.
[39] Kalnin D, Quennesson P, Artzner F, Schafer O, Narayanan T, Ollivon M. Progr. Colloid Polym Sci 2004;126:139. https://doi.org/10.1007/b93975.
[40] Tilley AJ, Dong Y-D, Chong JYT, Hanley T, Kirby N, Drummond CJ, et al. Soft Matter 2012;8:5696. https://doi.org/10.1039/c2sm00048b.
[41] Nelis V, Declerck A, De Neve L, Moens K, Dewettinck K, Van der Meeren P. Coll Surf A 2019;566:196. https://doi.org/10.1016/j.colsurfa.2019.01.019.
[42] Kalnin D, Schafer O, Amenitsch H, Ollivon M. Cryst Growth Des 2004;4:1283. https://doi.org/10.1021/cg030071k.
[43] MacWilliams SV, Clulow AJ, Kirby NM, Miller R, Boyd BJ, Gillies G, et al. J Colloid Interface Sci 2023;630:202. https://doi.org/10.1016/j.jcis.2022.10.069.

[44] Cholakova D, Glushkova D, Tcholakova S, Denkov N. ACS Nano 2020;14:8594. https://doi.org/10.1021/acsnano.0c02946.
[45] Craven PJ, Lencki RW. Food Funct 2012;3:228. https://doi.org/10.1039/c2fo00007e.
[46] Bursh T, Larsson K, Lundquist M. Chem Phys Lipids 1968;2:102. https://doi.org/10.1016/0009-3084(68)90036-4.
[47] Pink DL, Loruthai O, Ziolek RM, Wasutrasawat P, Terry AE, Lawrence MJ, et al. Small 2019;15:1903156. https://doi.org/10.1002/smll.201903156.
[48] Cebula DJ, McClements DJ, Povey MJW, Smith PR. J Am Oil Chem Soc 1992;69:130. https://doi.org/10.1007/BF02540562.
[49] Sadeghpour A, Parada ML, Vieira J, Povey M, Rappolt M. J Phys Chem B 2018;122:10320. https://doi.org/10.1021/acs.jpcb.8b06704.
[50] Larsson K. Eur. J. Lipid Sci. Techn. 1972;74:136. https://doi.org/10.1002/lipi.19720740302.
[51] Corkery RW, Rousseau D, Smith P, Pink DA, Hanna CB. Langmuir 2007;23:7241. https://doi.org/10.1021/la0634140.
[52] Pink DA, Hanna CB, Sandt C, MacDonald AJ, MacEachern R, Corkery R, et al. J Chem Phys 2010;132:054502. https://doi.org/10.1063/1.3276108.
[53] Golodnizky D, Shmidov Y, Bitton R, Bernardes CES, Davidovich-Pinhas M. J Mol Liq 2022;353:118703. https://doi.org/10.1016/j.jmolliq.2022.118703.
[54] Sato K. Crystallization of lipids. Fundamentals and applications in food, cosmetics, and pharmaceuticals. John Wiley & Sons; 2018.
[55] Larsson K. Arkiv Kemi 1964;23:35.
[56] Hernqvist L. Eur. J. Lipid Sci. Techn. 1984;86:297. https://doi.org/10.1002/lipi.19840860802.
[57] Sato K, Kuroda T. J Am Oil Chem Soc 1987;64:124. https://doi.org/10.1007/BF02546266.
[58] Sato K, Boistelle J. Crystal Growth 1984;66:441. https://doi.org/10.1016/0022-0248(84)90228-8.
[59] Norton IT, Lee-Tuffnell CD, Ablett S, Bociek SM. J Am Oil Chem Soc 1985;62:1237. https://doi.org/10.1007/BF02541834.
[60] Hagemann JW, Tallent WH, Kolb KE. J Am Oil Chem Soc 1972;49:118. https://doi.org/10.1007/BF02612641.
[61] Small DM. J Lipid Res 1984;25:1490. https://doi.org/10.1016/S0022-2275(20)34422-9.
[62] Cholakova D, Denkov N. Adv Colloid Interface Sci 2019;269:7. https://doi.org/10.1016/j.cis.2019.04.001.
[63] Bunjes H, Unruh T. Adv Drug Deliv Rev 2007;59:379. https://doi.org/10.1016/j.addr.2007.04.013.
[64] Sasaki M, Ueno S, Sato K, Garti N, Widlak NR. Cocoa Butter and Related Compounds. AOCS Press; 2012. https://doi.org/10.1016/B978-0-9830791-2-5.50009-8. Chapter 6.
[65] Motoyama M. Bull NARO Inst. Livest. Grassl Sci 2012;12:19.
[66] Bayes-Garcia L, Sato K, Ueno S, In Shahidi D, editors. Bailey's industrial oil and fat products. 7th ed. John Wiley & Sons; 2020. https://doi.org/10.1002/047167849X.bio020.pub2.
[67] Sato K, Goto M, Yano J, Honda K, Kodali DR, Small DM. J Lipid Res 2001;42:338. https://doi.org/10.1016/S0022-2275(20)31656-4.
[68] Kodali DR, Atkinson D, Small DM. J Phys Chem 1989;93:4683. https://doi.org/10.1021/j100348a055.
[69] Marangoni AG, Wesdorp LH. Structure and properties of fat crystal networks. CRC Press; 2012 [Chapter 9].
[70] Hagemann JW, Rothfus JA. J Am Oil Chem Soc 1983;60:1123. https://doi.org/10.1007/BF02671340.
[71] Van Langevelde A, Peschar R, Schenk H. Acta Crystallogr B 2001;57:372. https://doi.org/10.1107/s0108768100019121.
[72] Sirota E, King Jr H, Hughes G, Wan W. Phys Rev Lett 1992;68:492. https://doi.org/10.1103/PhysRevLett.68.492.
[73] Pradeilles JA, Zhong S, Baglyas M, Tarczay G, Butts CP, Myers EL, et al. Nature Chem 2020;12:475. https://doi.org/10.1038/s41557-020-0429-0.
[74] Knothe G, Dunn RO. J Am Oil Chem Soc 2009;86:843. https://doi.org/10.1007/s11746-009-1423-2.
[75] Ravotti R, Worlitschek J, Pulham CR, Stamatiou A. Molecules 2020;25:5572. https://doi.org/10.3390/molecules25235572.
[76] Mykhaylyk OO, Martin CM. Eur J Lipid Sci Techn 2009;111:227. https://doi.org/10.1002/ejlt.200800183.
[77] Bogatishcheva NS, Faizullin MZ, Popov AP, Nikitin ED. J Chem Thermodyn 2017;113:308. https://doi.org/10.1016/j.jct.2017.07.006.
[78] Sarı A, Biçer A, Karaipekli A, Alkan C, Karadag A. Solar energy mat. Solar Cells 2010;94:1711. https://doi.org/10.1016/j.solmat.2010.05.033.
[79] Wesdorp L. Liquid-multiple solid phase equilibria in fats: Theory and experiments, doctoral dissertation. TU Delft: Delft University of Technology; 1990.
[80] Liu R. Thermodynamic calculations of multicomponent phase compositions, masters dissertation. Dalhousie University; 2014.
[81] Moorthy AS, Liu R, Mazzanti G, Wesdorp LH, Marangoni AG. J Am Oil Chem Soc 2017;94:187. https://doi.org/10.1007/s11746-016-2935-1.
[82] Zeberg-Mikkelsen CK, Stenby EH. Fluid Phase Equilibria 1999;162:7. https://doi.org/10.1016/s0378-3812(99)00171-5.
[83] Seilert J, Floter E. Eur J Lipid Sci Technol 2021;123:2100010. https://doi.org/10.1002/ejlt.202100010.
[84] Seilert J, Moorthy AS, Kearsley AJ, Floter E. J Am Oil Chem Soc 2021;8:837. https://doi.org/10.1002/aocs.12515.
[85] Jensen LH, Mabis AJ. Acta Crystallogr 1966;21:770. https://doi.org/10.1107/S0365110X66003839.
[86] Gibon V, Blanpain P, Norberg B, Durant F. Bulletin des Sociétés Chimiques Belges 1984;93:27. https://doi.org/10.1002/bscb.19840930104.
[87] Van Langevelde A, Van Malssen K, Hollander F, Peschar R, Schenk H. Acta Crystallogr B 1999;55:114. https://doi.org/10.1107/s0108768198009392.
[88] Deng X. Effect of temperature on the wide angle X-ray diffraction of nanocrystalline triacylglycerols. Master of Science thesis, https://central.bac-lac.gc.ca/.item?id=TC-NSHD-56020&op=pdf&app=Library&oclc_number=1032967731; 2014.
[89] Pizzirusso A, Brasiello A, De Nicola A, Marangoni AG, Milano G. J Phys D Appl Phys 2015;48:494004. https://doi.org/10.1088/0022-3727/48/49/494004.
[90] Hsu W-D, Violi A. J Phys Chem B 2009;113:887. https://doi.org/10.1021/jp806440d.
[91] Hvolby A. J Am Oil Chem Soc 1974;51:50. https://doi.org/10.1007/BF00000012.
[92] Dafler J. J Am Oil Chem Soc 1977;54:249. https://doi.org/10.1007/BF02655165.
[93] Cebula D, McClements D, Povey MJW. J Am Oil Chem Soc 1990;67:76. https://doi.org/10.1007/BF02540630.
[94] Lencki RW, John Craven R. Cryst Growth Des 2012;12:4981. https://doi.org/10.1021/cg300901v.
[95] Peyronel F, Quinn B, Marangoni AG, Pink DA. Food Biophys 2014;9:304. https://doi.org/10.1007/s11483-014-9365-0.
[96] Campomanes P, Prabhu J, Zoni V, Vanni S. Biophys Rep 2021;1:100034. https://doi.org/10.1016/j.bpr.2021.100034.
[97] Cordina RJ, Smith B, Tuttle T. J Mol Graphics Modelling 2021;108:107996. https://doi.org/10.1016/j.jmgm.2021.107996.
[98] Brasiello A, Russo L, Siettos C, Milano G, Crescitelli S. Comp Aided Chem Eng 2010;28:625. https://doi.org/10.1016/S1570-7946(10)28105-1.
[99] Brasiello A, Crescitelli S, Milano G. Faraday Discuss 2012;158:479. https://doi.org/10.1039/c2fd20037f.
[100] Brasiello A, Crescitelli S, Milano G. Phys Chem Chem Phys 2011;13:16618. https://doi.org/10.1039/c1cp20604d.
[101] Cordina RJ, Smith B, Tuttle T. J Chem Theory Comput 2023;19:1333. https://doi.org/10.1021/acs.jctc.2c00975.
[102] Cordina RJ, Smith B, Tuttle T. Comput Chem 2023;44:1795. https://doi.org/10.1002/jcc.27128.
[103] Cordina RJ, Smith B, Tuttle T. J Chem Inf Model 2022;62:5601. https://doi.org/10.1021/acs.jcim.2c00972.
[104] Pizzirusso A, Peyronel F, Co ED, Marangoni AG, Milano G. J Am Chem Soc 2018;140:12405. https://doi.org/10.1021/jacs.8b04729.
[105] Sato K, Bayés-García L, Calvet T, Cuevas-Diarte MA, Ueno S. Eur. J. Lipid Sci. Techn. 2013;115:1224. https://doi.org/10.1002/ejlt.201300049.
[106] Kashchiev D. J Cryst Growth 2020;530:125300. https://doi.org/10.1016/j.jcrysgro.2019.125300.
[107] Fletcher PDI, Roberts NA, Urquhart C. J Ind Eng Chem 2016;34:382. https://doi.org/10.1016/j.jiec.2015.12.012.
[108] Ferstl P, Gillig S, Kaufmann C, Dürr C, Eder C, Wierschem A, et al. Ann N Y Acad Sci 2010;1189:62. https://doi.org/10.1111/j.1749-6632.2009.05179.x.
[109] Greiner M, Reilly AM, Briesen H. Agric. Food Chem 2012;60:5243. https://doi.org/10.1021/jf3004898.
[110] Masberg S. Differentialkalorimetrie (DSC) und differentialthermoanalyse (DTA) bei hohen drucken. PhD Thesis, https://d-nb.info/959480935/34; 1999.
[111] Co ED, Marangoni AG. Cryst Growth Des 2020;20:1628. https://doi.org/10.1021/acs.cgd.9b01363.
[112] Ferstl P, Eder C, Ruß W, Wierschem A. Int J 2011;31:339. https://doi.org/10.1080/08957959.2011.582870.
[113] MacMillan SD, Roberts KJ, Rossi A, Wells MA, Polgreen MC, Smith IH. Cryst Growth Des 2002;2:221. https://doi.org/10.1021/cg0155649.
[114] Bayés-García L, Patel AR, Dewettinck K, Rousseau D, Sato K, Ueno S. Curr Opin Food Sci 2015;4:32. https://doi.org/10.1016/j.cofs.2015.04.005.
[115] Mazzanti G, Marangoni AG, Idziak SHJ. Food Res Int 2009;42:682. https://doi.org/10.1016/j.foodres.2009.02.009.
[116] Pellegrino L, Tyagi G, Robles ESJ, Cabral JT. Phys Chem Chem Phys 2022;24:29413. https://doi.org/10.1039/d2cp02395d.
[117] Maleky F, Smith AK, Marangoni A. Cryst Growth Des 2011;11:2335. https://doi.org/10.1021/cg200014w.
[118] Maleky F, Marangoni A. Cryst Growth Des 2011;11:2429. https://doi.org/10.1021/cg200202u.
[119] Higaki K, Ueno S, Koyano T, Sato K. J Am Oil Chem Soc 2022;78:513. https://doi.org/10.1007/s11746-001-0295-y.
[120] da Silva TLT, Giacomozzi A, Martini S, Toro-Vazquez JF. Development of trans-free lipid systems and their use in food products3. Royal Society of Chemistry; 2022. https://doi.org/10.1039/9781839166532-00053.
[121] Jordens J, Gielen B, Xiouras C, Hussain MN, Stefanidis GD, Thomassen LCJ, et al. Van Gerven T. Chem Eng Proc – Proc Inten 2019;139:130. https://doi.org/10.1016/j.cep.2019.03.017.
[122] Ueno S, Ristic RI, Higaki K, Sato K. J Phys Chem B 2003;107:4927. https://doi.org/10.1021/jp027840f.
[123] Patel AR, Dewettinck K. Curr Opin Food Sci 2015;3:65. https://doi.org/10.1016/j.cofs.2015.05.010.
[124] Fredrick E, Foubert I, Van De Sype J, Dewettinck K. Cryst Growth Des 2008;8:1833. https://doi.org/10.1021/cg070025a.
[125] Yoshikawa C, Kida X, Sato K. J Oleo Sci 2014;63:333. https://doi.org/10.5650/jos.ess13155.
[126] Yoshikawa S, Kida H, Sato K. Eur. J. Lipid Sci. Techn. 2015;117:858. https://doi.org/10.1002/ejlt.201400420.

[127] Aronhime JS, Sarig S, Garti N. J Am Oil Chem Soc 1988;65:1144. https://doi.org/10.1007/BF02660571.
[128] Azoury R, Aronhime JS, Sarig S, Abrashkin S, Mayer I, Garti N. J Am Oil Chem Soc 1988;65:964. https://doi.org/10.1007/BF02544521.
[129] Verstringe S, Dewettinck K, Ueno S, Sato K. Cryst Growth Des 2014;14:5219. https://doi.org/10.1021/cg5010209.
[130] Mahisanunt B, Hondoh H, Ueno S. Cryst Growth Des 2020;20:4980. https://doi.org/10.1021/acs.cgd.0c00064.
[131] Garti N, Aserin A, Tiunova I, Binyamin H. J Am Oil Chem Soc 1999;76:383. https://doi.org/10.1007/s11746-999-0246-5.
[132] Larsson K, Quinn P, Sato K, Tiberg F. Lipids: Structure, physical properties and functionality. Bridgewater: The oily press; 2006 [Chapter 2].
[133] Watanabe S, Yoshikawa S, Arishima T, Sato K. J Am Oil Chem Soc 2018;95:447. https://doi.org/10.1002/aocs.12054.
[134] MacNaughtan W, Farhat IA, Himawan C, Starov VM, Stapley AGF. J Am Oil Chem Soc 2006;83:1. https://doi.org/10.1007/s11746-006-1167-1.
[135] Lutton E. J Am Oil Chem Soc 1955;32:49. https://doi.org/10.1007/BF02636501.
[136] Joglekar RB, Watson HE. J Soc Chem Ind 1928;47:365. https://doi.org/10.1002/jctb.5000475014.
[137] Kerridge R. J Chem Soc 1952:4577. https://doi.org/10.1039/JR9520004577.
[138] Costa MC, Boros LAD, Souza JA, Rolemberg MP, Krähenbühl MA, Meirelles AJA. J Chem Eng Data 2011;56:3277. https://doi.org/10.1021/je200033b.
[139] Takeuchi M, Ueno S, Sato K. Cryst Growth Des 2003;3:369. https://doi.org/10.1021/cg025594r.
[140] Engström L. Lipid 1992;94:173. https://doi.org/10.1002/lipi.19920940503.
[141] Moran DPJ. Polym Int 1963;13:91. https://doi.org/10.1002/jctb.5010130207.
[142] Koyano T, Hachiya I, Sato K. J Phys Chem 1992;96:10514. https://doi.org/10.1021/j100204a072.
[143] Minato A, Ueno S, Smith K, Amemiya Y, Sato K. J Phys Chem B 1997;101:3498. https://doi.org/10.1021/jp962956v.
[144] Minato A, Ueno S, Yano J, Smith K, Seto H, Amemiya Y, et al. J Am Oil Chem Soc 1997;74:1213. https://doi.org/10.1007/s11746-997-0047-7.
[145] Minato A, Yano J, Ueno S, Smith K, Sato K. Chem Phys Lipids 1997;88:63. https://doi.org/10.1016/S0009-3084(97)00045-5.
[146] Pereira E, Pereira DTV, Meirelles AJA, Maximo GJ. Fluid Phase Equilibria 2022;554:113327. https://doi.org/10.1016/j.fluid.2021.113327.
[147] Calligaris GA, da Silva TLT, Ribeiro APB, dos Santos AO, Cardoso LP. Chem Phys Lipids 2018;212:51. https://doi.org/10.1016/j.chemphyslip.2018.01.003.
[148] Himawan C, MacNaughtan W, Farhat IA, Stapley AGF. Eur. J. Lipid Sci. Techn. 2007;109:49. https://doi.org/10.1002/ejlt.200600179.
[149] Kellens M, Meeussen W, Hammersley A, Reynaers H. Chem Phys Lipids 1991;58:145. https://doi.org/10.1016/0009-3084(91)90120-Z.
[150] Kellens M, Meeussen W, Gehrke R, Reynaers H. Chem Phys Lipids 1991;58:131. https://doi.org/10.1016/0009-3084(91)90119-V.
[151] Cholakova D, Tcholakova S, Denkov N. Cryst Growth Des 2023;23:2075. https://doi.org/10.1021/acs.cgd.2c01021.
[152] Pattarino F, Bettini R, Bonda AF, Bella AD, Giovannelli L. Int J Pharm 2014;473:87. https://doi.org/10.1016/j.ijpharm.2014.06.042.
[153] Bhaggan K, Smith KW, Blecker C, Danthine S. Eur J Lipid Res Tech 2018;120:1800072. https://doi.org/10.1002/ejlt.201800072.
[154] Macridachis-González J, Bayés-García L, Calvet T. Molecules 2020;25:4562. https://doi.org/10.3390/molecules25194562.
[155] Bouzidi L, Narine S, Garti N, Widlak NR. Cocoa butter and related compounds. AOCS Press; 2012. https://doi.org/10.1016/B978-0-9830791-2-5.50007-4. Chapter 4.
[156] Knoester M, de Bruijne P, van Den Tempel M. Chem Phys Lipids 1972;9:309. https://doi.org/10.1016/0009-3084(72)90017-5.
[157] Cholakova D, Glushkova D, Pantov M, Tcholakova S, Denkov N. Coll. Surf. A 2023;668:131439. https://doi.org/10.1016/j.colsurfa.2023.131439.
[158] Garti N, Aronhime J, Sarig S. J Am Oil Chem Soc 1989;66:1085. https://doi.org/10.1007/BF02670089.
[159] Tapia-Ledesma C, Araujo-Diaz SB, Dibildox-Alvarado E, Ornelas-Paz JJ, Perez-Martinez JD. Thermochim Acta 2020;683:178455. https://doi.org/10.1016/j.tca.2019.178455.
[160] Costa MC, Boros LAD, Rolemberg MP, Krähenbühl MA, Meirelles AJA. J Chem Eng Data 2010;55:974. https://doi.org/10.1021/je900410j.
[161] Van den Tempel M. J Colloid Sci 1961;16:284. https://doi.org/10.1016/0095-8522(61)90005-8.
[162] Van den Tempel M. J Colloid Interface Sci 1979;71:18. https://doi.org/10.1016/0021-9797(79)90216-9.
[163] Nederveen CJ. J Colloid Sci 1963;18:276. https://doi.org/10.1016/0095-8522(63)90017-5.
[164] Marangoni AG, van Duynhoven JPM, Acevedo NC, Nicholson RA, Patel AR. Soft Matter 2020;16:289. https://doi.org/10.1039/c9sm01704f.
[165] Narine SS, Marangoni AG. Phys Rev E 1999;56:1908. https://doi.org/10.1103/PhysRevE.59.1908.
[166] Vreeker R, Hoekstra LL, den Boer DC, Agterof WGM. Colloids Surf 1992;65:185. https://doi.org/10.1016/0166-6622(92)80273-5.
[167] Voda A, Den Adel R, van Malssen K, van Duynhoven J. Cryst Growth Des 2017;17:1484. https://doi.org/10.1021/acs.cgd.6b00501.
[168] Narine SS, Marangoni AG. Phys. Rev. E 1999;60:6991. https://doi.org/10.1103/physreve.60.6991.
[169] Marangoni AG. Phys Rev B 2000;62:13951. https://doi.org/10.1103/PhysRevB.62.13951.
[170] Marangoni AG, Rogers MA. Appl Phys Lett 2003;82:1. https://doi.org/10.1063/1.1576502.
[171] Phipps LW. Trans Faraday Soc 1964;60:1873. https://doi.org/10.1039/TF9646001873.
[172] Schaefer DW. MRS Bull 1988;13:22. https://doi.org/10.1557/s088376940006632x.
[173] Acevedo NC, Marangoni AG. Cryst Growth Des 2010;10:3327. https://doi.org/10.1021/cg100468e.
[174] Acevedo NC, Marangoni AG. Cryst Growth Des 2010;10:3334. https://doi.org/10.1021/cg100469x.
[175] Miranda MAR, Sasaki JM. Acta Crystallogr 2018;A74:54. https://doi.org/10.1107/S2053273317014929.
[176] den Adel R, van Malssen K, van Duynhoven J, Mykhaylyk OO, Voda A. Eur J Lipid Sci Tech 2018:1800222. https://doi.org/10.1002/ejlt.201800222.
[177] Pink DA, Quinn B, Peyronel F, Marangoni AG. J Appl Phys 2013;114:234901. https://doi.org/10.1063/1.4847996.
[178] Peyronel F, Ilavsky J, Mazzanti G, Marangoni AG, Pink DA. J Appl Phys 2013;114:234902. https://doi.org/10.1063/1.4847997.
[179] Peyronel F, Pink DA, Marangoni AG. Curr Opin Colloid Interface Sci 2014;19:459. https://doi.org/10.1016/j.cocis.2014.07.001.
[180] Ramel PR, Co ED, Acevedo NC, Marangoni AG. Prog Lipid Res 2016;64:231. https://doi.org/10.1016/j.plipres.2016.09.004.
[181] Schaefer DW, Kohls D, Feinblum E. J Inorg Organomet Polym 2012;22:617. https://doi.org/10.1007/s10904-011-9643-y.
[182] Peyronel F, Quinn B, Marangoni AG, Pink DA. J Phys Condens Matter 2014;26:464110. https://doi.org/10.1088/0953-8984/26/46/464110.
[183] Zdravkova AN, van der Eerden JPJM. J Cryst Growth 2006;293:528. https://doi.org/10.1016/j.jcrysgro.2006.05.070.
[184] Zdravkova AN, van der Eerden JPJM. J Cryst Growth 2007;307:192. https://doi.org/10.1016/j.jcrysgro.2007.05.048.
[185] Zdravkova AN, van der Eerden JPJM. Cryst Growth Des 2007;7:2778. https://doi.org/10.1021/cg060701t.
[186] Hughes ZE, Walsha TR. RSC Adv 2015;5:49933. https://doi.org/10.1039/c5ra09192f.
[187] Green NL, Euston SR, Rousseau D. Coll Surf B 2019;179:107. https://doi.org/10.1016/j.colsurfb.2019.03.033.
[188] Ghosh S, Rousseau D. Cryst Growth Des 2012;12:4944. https://doi.org/10.1021/cg300872m.
[189] Cholakova D, Glushkova D, Tcholakova S, Denkov N. Langmuir 2021;37:7875. https://doi.org/10.1021/acs.langmuir.0c02967.
[190] Fang W, Mayama H, Tsujii K. Phys Chem B 2007;111:564. https://doi.org/10.1021/jp065589o.
[191] Hong B, Li D, Lei Q, Xu L, Fang W, Mayama H. Coll. Surf. A 2012;396:130. https://doi.org/10.1016/j.colsurfa.2011.12.056.
[192] Mayama H. Soft Matter 2009;5:856. https://doi.org/10.1039/B815005B.
[193] Wen J, Chen S, Chen G. Solid lipid nanoparticles. In: Roohinejad S, Greiner R, Oey I, Wen J, editors. Emulsion-based Systems for Delivery of food active compounds: Formation, application, health and safety. Croydon: John Wiley & Sons Ltd.; 2018. p. 121–38.
[194] Bunjes H. Curr Opin Coll Interface Sci 2011;16:405. https://doi.org/10.1016/j.cocis.2011.06.007.
[195] Schjoerring-Thyssen J, Olsen K, Koehler K, Jouenne E, Rousseau D, Andersen ML. J Agric Food Chem 2019;67:12273. https://doi.org/10.1021/acs.jafc.9b04215.
[196] Sato K, Ueno S. Curr. Opin. Coll. Interface Sci. 2011;16:384. https://doi.org/10.1016/j.cocis.2011.06.004.
[197] Schröder A, Sprakel J, Schroën K, Berton-Carabin CC. Eur. J. Lipid Sci. Techn. 2020;122:2000012. https://doi.org/10.1002/ejlt.202000012.
[198] Müller RH, Shegokar R, Keck CM. Curr Drug Discov Technol 2011;8:207. https://doi.org/10.2174/157016311796799062.
[199] Bertoni S, Passerini N, Albertini B, Pharm., 2021; 13: 1089. doi; https://doi.org/10.3390/pharmaceutics13071089.
[200] Bunjes H, Westesen K, Koch MHJ. Int J Pharm 1996;129:159. https://doi.org/10.1016/0378-5173(95)04286-5.
[201] Hunter RJ. Foundations of colloid sciencevol. 1. Oxford: Clarendon Press; 1987.
[202] Dyett B, Zychowski L, Bao L, Meikle TG, Peng S, Yu H, et al. Langmuir 2018;34:9470. https://doi.org/10.1021/acs.langmuir.8b01252.
[203] Lopez C, Ollivon M. J, Therm. Anal. Calorim 2009;98:29. https://doi.org/10.1007/s10973-009-0183-4.
[204] Salminen H, Helgason T, Aulbach S, Kristinsson B, Kristbergsson K, Weiss J. J Colloid Interface Sci 2014;426:256. https://doi.org/10.1016/j.jcis.2014.04.009.
[205] Sonoda T, Takata Y, Ueno S, Sato K. J Am Oil Chem Soc 2004;81:365. https://doi.org/10.1007/s11746-004-0908-5.
[206] Lopez C, Lesieur P, Keller G, Ollivon M. J Colloid Interface Sci 2000;229:62. https://doi.org/10.1006/jcis.2000.6988.
[207] Bunjes H, Steiniger F, Richter W. Langmuir 2007;23:4005. https://doi.org/10.1021/la062904p.
[208] Bunjes H, Koch MHJ, Westesen K. J Pharm Sci 2003;92:1509. https://doi.org/10.1002/jps.10413.
[209] Bunjes H, Koch MHJ. J Control Release 2005;107:229. https://doi.org/10.1016/j.jconrel.2005.06.004.
[210] Douaire M, di Bari V, Norton JE, Sullo A, Lillford P, Norton IT. Adv Colloid Interface Sci 2014;203:1. https://doi.org/10.1016/j.cis.2013.10.022.
[211] Arima S, Ueno S, Ogawa A, Sato K. Langmuir 2009;25:9777. https://doi.org/10.1021/la901115x.
[212] Wassell P, Okamura A, Young NWG, Bonwick G, Smith C, Sato K, et al. Langmuir 2012;28:5539. https://doi.org/10.1021/la204501t.

[213] Denkov N, Tcholakova S, Lesov I, Cholakova D, Smoukov SK. Nature 2015;528:392. https://doi.org/10.1038/nature16189.
[214] Cholakova D, Denkov N, Tcholakova S, Lesov I, Smoukov SK. Adv Colloid Interface Sci 2016;235:90. https://doi.org/10.1016/j.cis.2016.06.002.
[215] Cholakova D, Lisicki M, Smoukov SK, Tcholakova S, Emili Lin E, Chen J, et al. Nature Phys 2021;17:1050. https://doi.org/10.1038/s41567-021-01291-3.
[216] Cholakova D, Vinarov Z, Tcholakova S, Denkov N. Curr Opin Colloid Interface Sci 2022;59:101576. https://doi.org/10.1016/j.cocis.2022.101576.
[217] Cholakova D, Glushkova D, Valkova Zh, Tsibranska-Gyoreva S, Tsvetkova K, Tcholakova S, et al. J Colloid Interface Sci 2021;604:260. https://doi.org/10.1016/j.jcis.2021.06.122.
[218] Joseph S, Rappolt M, Schoenitz M, Huzhalska V, Augustin W, Scholl S, et al. Langmuir 2015;31:6663. https://doi.org/10.1021/acs.langmuir.5b00874.
[219] Rosenblatt KM, Bunjes H. Mol Pharm 2009;6:105. https://doi.org/10.1021/mp8000759.
[220] Oh J-H, McCurdy AR, Clark S, Swanson BG. J Am Oil Chem Soc 2005;82:13. https://doi.org/10.1007/s11746-005-1036-y.
[221] Pluntze AM, Cape JL, Klaus ND, Lyon DK. Int J Pharm 2023;5:122806. https://doi.org/10.1016/j.ijpharm.2023.122806.
[222] Unruh T, Westesen K, Bösecke P, Lindner P, Koch MHJ. Langmuir 2002;18:1796. https://doi.org/10.1021/la0110601.
[223] Ueno S, Nishida T, Sato K. Cryst Growth Des 2008;8:751. https://doi.org/10.1021/cg0706159.
[224] Truong T, Morgan GP, Bansal N, Palmer M, Bhandari B. Food Chem 2015;171:157. https://doi.org/10.1016/j.foodchem.2014.08.113.
[225] Jores K, Mehnert W, Drechsler M, Bunjes H, Johann C, Mäder K. J Control Release 2004;95:217. https://doi.org/10.1016/j.jconrel.2003.11.012.
[226] Gao N, Sebben DA, Gillies G, Krasowska M, Beattie DA. Cryst Growth Des 2019;19:513. https://doi.org/10.1021/avs.cgd.8b01699.
[227] Lesov I, Valkova Zh, Vassileva E, Georgiev GS, Ruseva K, Simeonov M, et al. Macromol. 2018;51:7456. https://doi.org/10.1021/acs.macromol.8b00529.
[228] Guttman S, Kesselman E, Jacob A, Marin O, Danino D, Deutsch M, et al. Nano Lett 2019;19:3161. https://doi.org/10.1021/acs.nanolett.9b00594.
[229] Gehrer S, Schmiele M, Westermann M, Steiniger F, Unruh T. J Phys Chem B 2014;118:11387. https://doi.org/10.1021/jp506787v.
[230] Giso MQ, Zhao H, Spicer PT, Atherton TJ. Langmuir 2020;36:13853. https://doi.org/10.1021/acs.langmuir.0c02249.
[231] Giso MQ, Zhao H, Spicer PT, Atherton TJ. J Colloid Interface Sci 2022;605:138. https://doi.org/10.1016/j.jcis.2021.07.045.
[232] Westesen K, Siekmann B. Int J Pharm 1997;151:35. https://doi.org/10.1016/S0378-5173(97)04890-4.
[233] Illing A, Unruh T, Koch MHJ. Pharm Res 2004;21:592. https://doi.org/10.1023/b:pham.0000022405.49805.a7.
[234] Schmiele M, Schindler T, Westermann M, Steiniger F, Radulescu A, Kriele A, et al. J Phys Chem B 2014;118:8808. https://doi.org/10.1021/jp502580a.
[235] Unruh T. J Appl Crystallography 2007;40:1008. https://doi.org/10.1107/s0021889807044378.
[236] Schmiele M, Knittel C, Unruh T, Busch S, Morhenn H, Boesecke P, et al. Phys Chem Chem Phys 2015;17:17939. https://doi.org/10.1039/c5cp01241d.
[237] Lesov I, Glushkova D, Cholakova D, Georgiev MT, Tcholakova S, Smoukov SK, et al. J. Ind. Eng. Chem. 2022;112:37. https://doi.org/10.1016/j.jiec.2022.03.043.